A Dissertation for the Degree of Doctor Scientiarum

Low-frequency Noise Characterization of Silicon-Germanium Resistors and Devices

Jarle Andre Johansen

June 2004

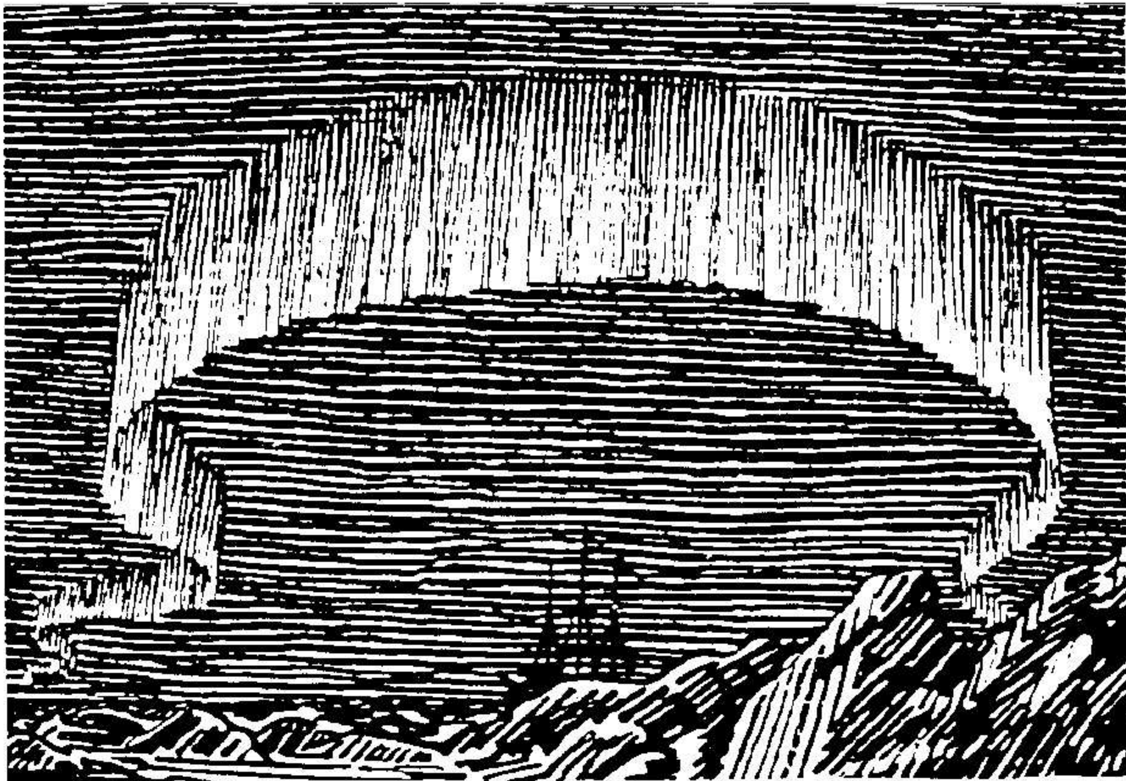

Original by F. Nansen

FACULTY OF SCIENCE

Department of Physics

University of Tromsø, NO-9037 Tromsø, Norway, telephone: +47 77 64 51 50, fax no: +47 77 64 55 80

A Dissertation for the Degree of Doctor Scientiarum

Low-frequency Noise Characterization of Silicon-Germanium Resistors and Devices

Jarle Andre Johansen

June 2004

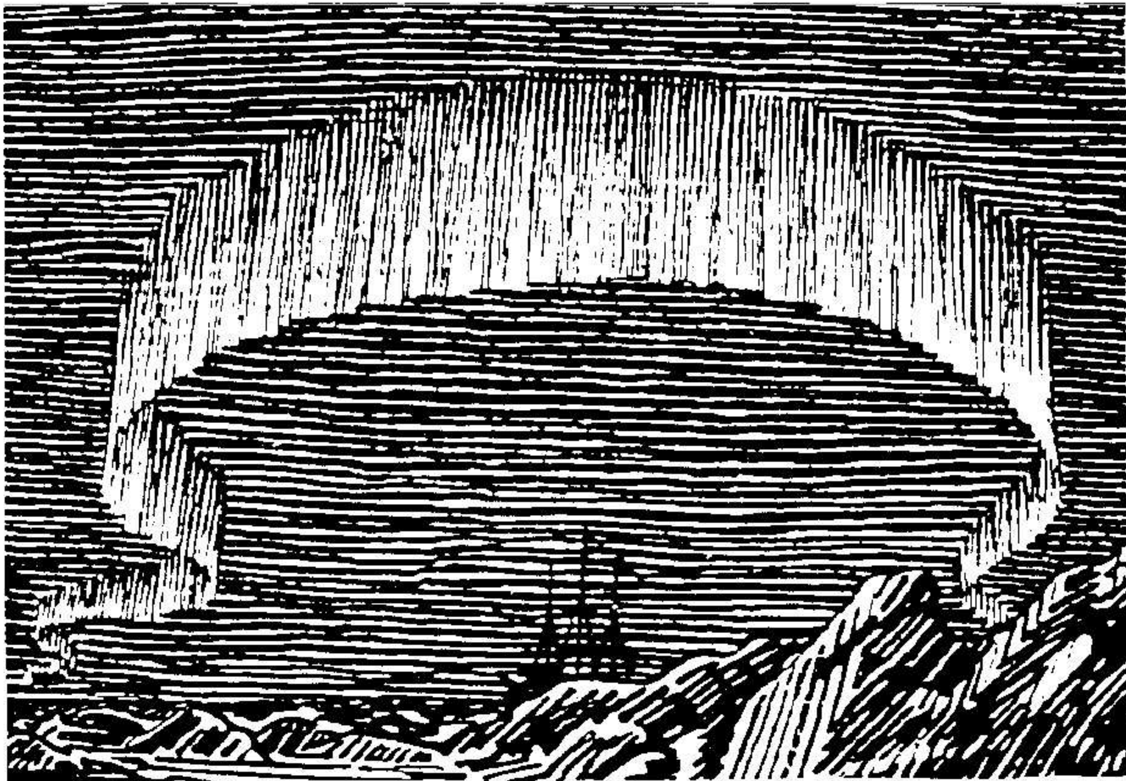

Original by F. Nansen

FACULTY OF SCIENCE

Department of Physics

University of Tromsø, NO-9037 Tromsø, Norway, telephone: +47 77 64 51 50, fax no: +47 77 64 55 80

To Aina Sofie,
Lill Johannne and Isak Andre

Abstract

The main topic of this thesis is experimental low-frequency electrical noise characterization of semiconductor devices. In particular, we concentrate on applications of the silicon-germanium alloy (SiGe).

Low-frequency electrical noise is a sensitive measure of defects and non-idealities in semiconductor devices, which directly or indirectly impact device performance and reliability. Thus, it is of prime importance to be able to characterize the noise in semiconductor devices.

We compare the low-frequency noise from poly-crystalline silicon-germanium thin film resistors with different germanium content, film thickness and doping level. The noise level decreases with increasing doping density. We find that the germanium content and film thickness have little influence on the noise level. The noise was found to stem from mobility fluctuations in the depletion region of the grains.

We compare the low-frequency noise of silicon based field-effect transistors with poly-crystalline gates, made from silicon and silicon-germanium. The output noise level for N-MOSFETs is independent of the gate material, whereas for P-MOSFETs the silicon-germanium gate material results in lower noise. Analysis of fluctuating physical quantities, points towards mobility fluctuations for P-MOS, and number fluctuations for N-MOS.

We present results from measurement of the low-frequency electrical noise in AlGaInP Quantum Well Lasers. Experimental evidence of a connection between the noise and device reliability is found, and hence, low-frequency noise measurements can be used as a non-destructive reliability indicator for laser diodes.

The low-frequency noise in state-of-the-art silicon-germanium Heterojunction Bipolar Transistors (HBTs) is explored. Device geometrical down-scaling induces a device-to-device noise variation, caused by small sets of noise generating traps, that are different from device to device. We use proton irradiation to introduce additional traps, and find that it can reduce the noise variation without increasing the noise level significantly.

Aggressive down-scaling normally results in higher low-frequency noise. However, we find that the latest generation of SiGe HBTs (> 200 GHz) breaks this trend, and only a residual background noise remains, resulting in record values of low-frequency noise level and noise corner frequency.

We present, and apply, recent statistical tools to probe for non-linear coupling between frequency components in a noise signal. These tools are applied to low-frequency noise time series with Random Telegraph Signal (RTS) noise from small geometry SiGe HBTs. The noise in small HBTs is shown to be non-Gaussian and non-linear. The non-linearity is shown to originate from the RTS component of the noise.

Preface

This thesis consists of 7 chapters, and it describes the results from low-frequency noise experiments performed on on-wafer semiconductor devices at room temperature, with emphasis on applications of the silicon-germanium alloy.

The first year of my PhD work was devoted to the installation of a new probe station, developing measurement techniques to obtain reliable on-wafer electronic noise measurements, and to automation of the noise data acquisition.

In this thesis, applications of silicon-germanium is the common lead, with the exception of chapter 4, where we focus on low-frequency noise and reliability of AlGaInP laser diodes. In the following, an outline of the thesis is given in further detail.

Chapter 1: Introduction

The first chapter is a general introduction and a motivation for the investigations documented in the thesis. A brief review of low-frequency noise sources in semiconductors, and a short history of the silicon-germanium alloy have also been included.

Chapter 2: Polycrystalline Si and SiGe Thin-film Resistors

In this chapter we compare the low-frequency noise from poly-crystalline thin film resistors with different germanium content and film thickness. These results were first presented at an international conference in India, and later published in Solid-State Electronics:

- X. Y. Chen, J. A. Johansen, C. Salm and A. D. van Rheenen. *On low-frequency noise of polycrystalline Ge_xSi_{1-x} for sub-micron CMOS technologies*. In *Proceeding of the International Conference on Communications, Computers & Devices (ICCCD)*, edited by S. L. Maskara and T. S. Lamba, volume I, pp. 187–190. Kharagpur, India, December 14-16, 2000b.

- X. Y. Chen, J. A. Johansen, C. Salm and A. D. van Rheenen. *On low-frequency noise of polycrystalline Ge_xSi_{1-x} for sub-micron CMOS technologies*. *Solid-State Electronics*, **45**(11): 1967–1971, 2001b.

Chapter 3: Poly-Si- and Poly-SiGe-gated Field Effect Transistors

In this chapter we compare the low-frequency noise of silicon based field-effect transistors with poly-crystalline gates, made from silicon and silicon-germanium. This chapter is based on results published at the international noise conference in Florida:

- J. A. Johansen, H. Figenschau, X. Y. Chen, A. D. van Rheenen and C. Salm. *Low frequency noise in poly-Si- and poly-SiGe-gated MOSFETs*. In *Proceedings of the International Conference on Noise in Physical Systems and $1/f$ Fluctuations (ICNF)*, edited by G. Bosman, pp. 161–164. Gainesville, FL, USA, October 22-25, 2001.

Chapter 4: Quantum Well Semiconductor Lasers

In this chapter, we discuss results on low-frequency electrical noise in AlGaInP Quantum Well Lasers. We look into the location of low-frequency noise sources, and we discuss how the noise can be used as a non-destructive tool to probe device reliability. This chapter is a reformatted version of a conference paper presented at an international conference in China. My contribution to this work was mainly experimental:

- X. Y. Chen, J. A. Johansen and C. L. Liu. *Temperature dependence of low frequency electrical noise and reliability of semiconductor lasers*. In *Proceedings of SPIE, Semiconductor Optoelectronic Device Manufacturing and Applications*, edited by D. Chen, R. T. Chen, G.-Y. Wang and C.-C. Zhu, volume 4602, pp. 128–133. Nanjing, China, November 7–9, 2001a.

Chapter 5: SiGe Heterojunction Bipolar Transistors

In this chapter, we discuss low-frequency noise in state-of-the-art silicon-germanium Heterojunction Bipolar Transistors. We look into scaling induced noise variation, we use proton irradiation to add noise sources, and we find record-low noise levels that break the scaling trend of noise. This chapter is based on work done at Georgia Tech in close cooperation with Zhenrong Jin, while I was on leave from the University of Tromsø. The chapter consists of a collection of recent conference and journal papers, and thus some overlap in terms of results presented in the sections of this chapter is unavoidable:

- J. A. Johansen, Z. Jin, J. D. Cressler and A. J. Joseph. *Geometry-dependent low-frequency noise variations in 120 GHz f_T SiGe HBTs*. In *Digest of Papers, Topical Meeting on Silicon Monolitic Integrated Circuits in RF Systems (SiRF)*, edited by G. E. Ponchak, pp. 57–59. Grainau, Germany, April 9–11, 2003b.

- Z. Jin, J. A. Johansen, J. D. Cressler, R. A. Reed, P. W. Marshall and A. J. Joseph. *Using proton irradiation to probe the origin of low-frequency noise variations in SiGe HBTs*. In *Annual Nuclear and Space Radiation Effects Conference (NSREC)*. Monterey, CA, USA, July 21–25, 2003b.

- Z. Jin, J. A. Johansen, J. D. Cressler, R. A. Reed, P. W. Marshall and A. J. Joseph. *Using proton irradiation to probe the origin of low-frequency noise variations in SiGe HBTs*. *IEEE Transactions on Nuclear Science*, **50**(6): 1816–1820, 2003c.

- J. A. Johansen, Z. Jin, J. D. Cressler, Y. Cui, G. Niu, Q. Liang, J.-S. Rieh, G. Freeman, D. Ahlgren and A. Joseph. *On the scaling limits of low-frequency noise in SiGe HBTs*. In *International Semiconductor Device Research Symposium Proceedings (ISDRS)*, pp. 12–13. Washington, DC, USA, December 10–12, 2003a.

- J. A. Johansen, Z. Jin, J. D. Cressler, Y. Cui, G. Niu, Q. Liang, J.-S. Rieh, G. Freeman, D. Ahlgren and A. Joseph. *On the scaling limits of low-frequency noise in SiGe HBTs*. *Accepted for publication in Solid-State Electronics*, 2004b.

Chapter 6: Voltage Time Series of Low-frequency Noise

In this chapter, we present recent statistical tools to characterize noise, and to probe for nonlinear coupling between frequency components in a noise signal. These tools have been applied to random telegraph signal (RTS) noise found in small geometry SiGe HBTs. This chapter is based on three recently submitted conference papers. The first two of these papers focus on the statistical tools, and in the third paper these tools are applied to the analysis of low-frequency noise in SiGe HBTs:

- Y. Birkelund, J. A. Johansen, A. Hanssen, J. D. Cressler and A. D. van Rheenen. *Time series analysis of low-frequency noise in SiGe HBTs*. In *Proceedings of the Norwegian Signal Processing Symposium (NORSIG)*. Bergen, Norway, September 6-10, 2003b.

- Y. Birkelund, J. A. Johansen and A. Hanssen. *High-precision surrogate based tests for Gaussianity and linearity*. *Accepted for the European Signal Processing Conference*

(EUSIPCO), Vienna, Austria, September 6-10, 2004.

- J. A. Johansen, Y. Birkelund, Z. Jin and J. D. Cressler. *A statistical tool for probing the coupling between noisy traps in semiconductor devices, with application to* $1/f$ *noise in SiGe HBTs. Accepted for the Topical Meeting on Silicon Monolitic Integrated Circuits in RF Systems (SiRF)*, Atlanta, Georgia, September 8-12, 2004a.

Chapter 7: Summary and Conclusions

In this chapter, we summarize the results of the present thesis. Finally, we suggest relevant investigations for future research.

Acknowledgements

I would like to thank *all* the people that has helped me in accomplishing this thesis.

First I would like to thank Arthur D. van Rheenen, my first supervisor, for initiating the project, and for help in the final stages of preparing this thesis. I am also thankful to my second supervisor Xu-yuan Chen for his guidance and help through the early years, and for teaching me the art of low-frequency noise measurements. Unfortunately, I could only enjoy the full benefits of their guidance in the beginning of the project as they left their positions at the University of Tromsø in 2001 (van Rheenen) and 2002 (Chen).

I had the pleasure of joining Dr. John D. Cressler's research group at Georgia Institute of Technology during the 2002-2003 academic year. It turned out to be a very fruitful experience. I was provided access to state-of-the-art devices, which was very important for the accomplishment of my thesis. I thank John for hosting me. My stay at *Georgia Tech* was supported by grants from the University of Tromsø and the Fulbright Foundation.

I am grateful to my fellow Ph.D Students, in particular Yngve Birkelund, a close friend for more than 20 years, and Zhenrong Jin, whom I met at Georgia Tech, and initiated a close cooperation with during the year in Atlanta. Without their help, the last two chapters would not have been possible.

Of course, I am in debt to my soul mate Aina, and our daughter Lill Johanne and son Isak Andre for their patience and *love*.

Finally, I wish to thank the following: Karl Magnus Fossan for guidance on measurement setup issues, in particular ground-loops, Kjell-Arne Willumstad for welding the shielding box, Hallvar Figenschau for cooperation and help during the first year when he was working on his Master thesis, Cora Salm for providing resistors and MOSFETs, Anders Karlsen for ideas for automatic noise measurements, and Alfred Hanssen for proofreading and for helping me through the last months of writing.

Tromsø, Norway Jarle Andre Johansen
April 2004

Contents

1 Introduction **1**

1.1 The Silicon-Germanium Alloy . . . 2

1.1.1 Band-Gap Engineering . . . 2

1.2 Semiconductor Low-frequency Noise Sources . . . 3

1.2.1 Thermal Noise . . . 3

1.2.2 Shot Noise . . . 4

1.2.3 Generation-Recombination Noise . . . 4

1.2.4 Random Telegraph Signal Noise . . . 5

1.2.5 $1/f$ Noise . . . 6

1.2.6 Mobility Fluctuations $1/f$ Noise . . . 6

1.2.7 Number Fluctuations $1/f$ Noise . . . 7

1.2.8 Semiconductor Device Noise and Scaling . . . 7

2 Polycrystalline Si and SiGe Thin-film Resistors **9**

2.1 On Low-frequency Noise of Polycrystalline SiGe for Sub-Micron CMOS Technologies . . . 10

2.1.1 Introduction . . . 10

2.1.2 Characteristics of The Gate Films . . . 11

2.1.3 Low-frequency Noise Measurement and Results . . . 14

2.1.4 Discussion . . . 16

2.1.5 Conclusions . . . 17

3 Poly-Si- and Poly-SiGe-gated Field Effect Transistors **19**

3.1 Low-frequency Noise in Poly-Si- and Poly-SiGe-gated MOSFETs . . . 20

3.1.1 Introduction . . . 20

3.1.2 Devices . . . 21

3.1.3 Threshold Voltage Extraction and DC Performance . . . 22

3.1.4 Drain Current Noise Level Comparison 25
3.1.5 Analysis of Noise Origin 28
3.1.6 Summary 32

4 Quantum Well Semiconductor Lasers **33**
4.1 Temperature Dependence of Low-frequency Electrical Noise and Reliability of Semiconductor Lasers 34
4.1.1 Introduction 34
4.1.2 Noise Measurement as a Diagnostic Tool for Reliability of Laser Diodes 35
4.1.3 Experiments and Results 37
4.1.4 Discussion 41
4.1.5 Conclusion 42

5 SiGe Heterojunction Bipolar Transistors **43**
5.1 Low-frequency Noise in 120 GHz f_T SiGe HBT's 45
5.1.1 Introduction 45
5.1.2 Experiment 45
5.1.3 Results and Discussion 46
5.1.4 Summary 49
5.2 Proton Response of Low-frequency Noise in 120 GHz f_T SiGe HBT's . . . 51
5.2.1 Introduction 51
5.2.2 Experiment 52
5.2.3 Measurement Results 53
5.2.4 Model and Discussion 56
5.2.5 Summary 60
5.3 Low-frequency Noise Variation in 200 and 350 GHz f_T SiGe HBT's 62
5.3.1 Introduction 62
5.3.2 Experiment and Devices 62
5.3.3 Noise Measurement Results 64
5.3.4 Noise Model and Discussion 65
5.3.5 Noise Simulations 66
5.3.6 Summary 68

6 Voltage Time Series of Low-frequency Noise **71**
6.1 Statistical Tools for Analysis of Noise Time Series 73

6.1.1 Introduction 73
6.1.2 Devices and Measurements 74
6.1.3 Power Spectrum Estimation 77
6.1.4 Gaussianity and Linearity 81
6.1.5 Decomposition of Time Series 84
6.1.6 Conclusion 86

7 Summary and Conclusions **87**

Chapter 1

Introduction

Various definitions of noise can be found in the literature. For example, in Dictionary.com noise is defined as, "*…a disturbance, especially a random and persistent disturbance, that obscures or reduces the clarity of a signal…*" Although not very specific, this definition coincides very well with the common understanding of noise. Another definition can be found in Columbia Encyclopedia, "*…noise is any signal that does not convey useful information…*" Also this definition is generally correct. However, in certain situations the noise signal *does* carry useful information. In this thesis we show that very useful information about the electronic transport properties of semiconductor material and devices can be obtained from making measurements of, exactly, the noise signal.

The interest in low-frequency noise in electronic devices has been motivated by at least two factors. First the theoretical and experimental studies of the noise itself are of major interest. The low-frequency noise has a tremendous impact on devices and circuits. It sets the lower limit of detectable signals, and it converts to phase noise and thereby reduces the achievable spectral purity in communications systems. It is therefore of prime importance to be able to characterize the noise from electronic devices.

Equally important is the information the noise carries about the microscopical physical processes taking place. In electronic devices, noise is caused by the random movement of discrete charge carriers, and their interaction with the environment in which they move. Hence, they carry useful information about that environment, e.g., the interior of a resistor or other semiconductor device.

In the search for even better performing devices, one often looks at alternative materials. Although silicon is the most widely used semiconductor material and is still at the edge of technology, there are some niche applications, such as microwave and optical, where III-IV compounds dominate. Also, to extend the life of silicon process-

ing, germanium is introduced in the form of silicon-germanium alloys. Here we shall mainly consider devices where the silicon-germanium alloy is applied. The successful introduction of germanium into silicon has allowed engineering of material properties, often termed band-gap engineering, in fully silicon compatible processes, with great enhancement of device performance.

Another performance enhancing development, that also has economical benefits, is downscaling of the device geometry. Ultimately, the device or system performance will be determined by the charge transport properties of just a few charge carriers, or even a single electron. This may lead to possible statistical variations from device to device, which cannot be explained by conventional DC-models that rely on the collective behavior of many carriers. This has a profound effect on the noise performance of devices and circuits. Such a behavior has to be described by statistical models for noise.

In the following sections of this introductory chapter we will present the most common sources of noise semiconductor devices, and we will give a brief history of the use of the silicon-germanium alloy in semiconductor industry.

1.1 The Silicon-Germanium Alloy

Although germanium was the semiconductor used for the first transistor [Bardeen and Brattain, 1948; Shockley, 1949], silicon has dominated the semiconductor industry for more than fifty years. This is due to the abundance of silicon, and the fact that the world largest perfect crystals can be made from silicon at a cost much lower than any other semiconductor material. Also it brings along a stable and high quality silicon oxide insulator.

The idea of combining silicon and germanium is an old one [Stöhr and Klemm, 1939; Johnson and Christian, 1954], but the ability to grow stable layers of silicon-germanium was not realized until the early 1980's. From that time on, a rapid development in applications of silicon-germanium has given a new boost to the silicon based RF semiconductor niche, where the magic of band-gap engineering utilized in III-IV compounds for years now could be practiced in silicon.

1.1.1 Band-Gap Engineering

By introducing germanium into silicon we can tune the electrical and physical properties of the material. Silicon-germanium alloys are generally referred to as $\mathrm{Si}_{1-x}\mathrm{Ge}_x$,

where x is the germanium mole fraction.

Ge has a larger lattice constant than Si, resulting in a smaller band gap for Ge of 0.66 eV compared to Si with 1.12 eV, making it a good candidate for band-gap engineering in Si. The electron affinity for Si and Ge is almost the same, and hence does not change much in the SiGe alloy. However, the band gap and therefore the valence band level will be moved towards the mid-gap level of pure Si. In addition, the difference in lattice constant will cause a compressive strain in the SiGe alloy grown on a Si wafer, which in turn improves carrier mobility in the SiGe layer.

Polycrystalline SiGe has been used as an alternative to Si for thin film resistors and as a gate material for MOSFETs. Strained crystalline SiGe layers have been applied as the base of Si based HBTs and in the cannel of MOSFETs to a great extent, and with impressive performance improvements compared to their pure Si counterparts. Noise in SiGe based devices has been reviewed by e.g., Regis et al. [2001], and it is found that the noise properties of SiGe based devices is very attractive compared to the III-IV counterparts.

In this thesis we will characterize low-frequency noise from the first three applications mentioned above, in addition to low-frequency electrical noise in lasers.

1.2 Semiconductor Low-frequency Noise Sources

1.2.1 Thermal Noise

Consider an ohmic device at temperature T. Charge carriers inside collide with phonons causing Browninan random motion with a kinetic energy proportional to T. This yields open circuit voltage fluctuations with zero average value, but a nonzero rms value given by,

$$v_n = \sqrt{\frac{4hfBR}{e^{hf/kT} - 1}} \tag{1.1}$$

where v_n is the rms value in Volts, $h = 6.63 \times 10^{-34}$ Js is Planck's constant, $k = 1.38 \times 10^{-23}$ JK^{-1} is Boltzmann's constant, B is the bandwidth of the system in Hz, f is the center frequency of the band in Hz and R is the resistance in Ohms. For the low frequencies considered here, we use the Rayleigh-Jeans approximation, where we consider only the first two terms of a series expansion of the exponential, $e^{hf/kT} - 1 \approx hf/kT$. Using the approximation and converting to voltage spectral density v_n^2/B, we get,

$$S_V = 4kTR \tag{1.2}$$

Hence, the thermal noise is a white noise, i.e., a noise with a frequency independent spectrum for frequencies up to the validity of the approximation, $f < kT/h \approx 6250$ GHz at 300 K, or $f \approx 1/(2\pi RC)$, or $f \approx 1/\tau_{coll} \approx 10^{12}$ Hz. Here C is the parasitic capacitance parallel to R and τ_{coll} the mean time between collisions of free charge carriers. Thermal noise is also known as Johnson or Nyquist noise.

Thermal noise is normally the white noise floor observed at high frequencies for the resistors and MOSFETs considered in this thesis.

1.2.2 Shot Noise

Shot noise is due to the corpuscular nature of charge transport. In 1918, Walter Schottky discovered shot noise in radio tubes and developed what has been known as Schottkys theorem [Schottky, 1918]. In a tube, under steady-state conditions, the time-averaged current is constant, but arrival times of the electrons are not equally spaced, because the electrons leave the cathode at random times. This leads to fluctuations in the measured current, which can be described by simple Poisson statistics. It is required that there is a DC current present or there is no shot noise, and thermal noise would dominate. Shot noise can be observed in for example Schottky-barriers and in PN-junctions where current results from the random emission of charged particles which are discrete and independent. The short circuit current spectral density is given by,

$$S_I = 2qI \tag{1.3}$$

where I is the DC-current in Ampere, and $q = 1.6 \times 10^{-19}$ C. Shot noise in PN junctions is white up to a frequency given by the reciprocal of the transit time, i.e., as long as the fluctuations are slower than the rate of recombination.

Shot noise is normally the white noise floor observed for the bipolar devices, i.e, the lasers and the HBTs, considered in this thesis.

1.2.3 Generation-Recombination Noise

Generation-Recombination (GR) noise is due to fluctuations in the number of free carriers associated with random transitions of charge carriers between energy states, mostly between an energy band and a discrete energy level (trap) in the bandgap. For a two

terminal sample with resistance R, the spectral densities are,

$$\frac{S_R}{R^2} = \frac{S_V}{V^2} = \frac{S_N}{N^2} = \frac{\langle \Delta N^2 \rangle}{N_0^2} \frac{4\tau_N}{1 + (2\pi f \tau_N)^2} \tag{1.4}$$

where S_R, S_V and S_N are spectral densities of resistance, voltage and number of carriers, respectively, $N_0 = \langle N \rangle$ is the average number of free carriers, and τ_N is the trapping time. The resultant spectrum is of Lorentzian type, which is approximately constant below a frequency given by $f = 1/(2\pi\tau_N)$, and rolls off like $1/f^2$ at higher frequencies.

Lorentzian GR-noise signatures are found in all the device types considered in this thesis, but we could only see it in a few samples, and these were not used since they were not under study. For the bipolar transistors, we observed and explored the GR-noise components further.

1.2.4 Random Telegraph Signal Noise

The notion Random Telegraph Signal (RTS) refers to a random signal that can be in two states, called high and low. It is due to trapping and de-trapping of carriers from two-level fluctuators, for example a single GR-trap [Mitin et al., 2003]. It can influence the current flow in two ways, by the trapping of carriers and thereby removing them from the current flow, and by the fact that the trapping of carriers can locally change the Fermi-level, which in turn will reduce or enhance the flow of carriers in the vicinity of the trap [von Hartmann et al., 2002]. Multilevel RTS signatures can be observed if more than one trap is present. These are characterized by a time signal switching between more than two levels.

An observable RTS signature in the time-domain will always show up as a Lorentzian component in the power spectrum, due to the fact of a larger amplitude for the RTS compared to the amplitude of the remaining noise. The converse is not necessarily true, many independent traps, e.g., spatially distributed, with the same characteristic time constant, will give rise to a single Lorentzian spectral signature, but if the traps operate independently, an RTS signal will not necessarily be observable in the time-domain [Sanden and Deen, 2002].

Controversy exists about the difference and similarity in origin and appearance, for GR noise and RTS noise. This has been reviewed and discussed in depth in many of the papers in the collection by Balandin [2002]. Here we will not consider this controversy.

We have measured RTS noise in SiGe HBTs, that has been analyzed in the last part of this thesis.

1.2.5 $1/f$ Noise

$1/f$, "one-over f" noise, or flicker noise, owes its name to its spectral density that is inversely proportional to frequency over a wide frequency range down to very low frequencies (10^{-6} Hz). This noise is caused by a fluctuation of the conductivity σ,

$$\sigma = q(\mu_n n + \mu_p p) \tag{1.5}$$

where μ_n and n are electron mobility and density, respectively, and μ_p and p are hole mobility and density, respectively. Hence, conductivity fluctuations can be caused by fluctuations in the number of carriers or in their mobility.

For homogenous samples of semiconductors and metals, Hooge [1969] presented an empirical relation for $1/f$ noise,

$$\frac{S_G}{G^2} = \frac{\alpha}{fN} \tag{1.6}$$

where S_G is the spectral density of fluctuations in conductance G, N is the total number of free carriers, and α is a dimensionless parameter.

There is no generally accepted theory for $1/f$ noise but two major schools of thought have been competing. They will be briefly reviewed in the following sections.

1.2.6 Mobility Fluctuations $1/f$ Noise

This model considers carrier scattering by lattice vibrations to be the origin of $1/f$ fluctuations [Hooge et al., 1981],[Hooge and Vandamme, 1978],[Chen, 1997]. The carrier mobility in the bulk of the material is assumed to fluctuate and cause the observed conductivity fluctuations, hence it is a volume effect. At the time when the Hooge relation was proposed, the parameter α was considered a universal constant with a value of 2×10^{-3}. Because of the fact that α varied between 10^{-7} to 10^{-2} [Hooge, 1994], the validity of equation (1.6) was questioned. It turned out that the value of α was very sensitive to material quality and processing techniques, and hence it can be used as a measure of the quality and relative noise level of material and devices.

The Hooge relation (equation (1.6)) has been extensively used and connected to the mobility fluctuations model. Later, Hooge [1994] has stressed that it is an empirical relation and that the only theoretical idea behind it, is that whatever carriers do to produce $1/f$ noise, they do it independently.

1.2.7 Number Fluctuations $1/f$ Noise

A model where one assumes that fluctuations in the number of free carriers is causing $1/f$ noise, is the McWhorter model [McWhorter, 1955b], similar to what was suggested earlier by Bernamont [1937] and Surdin [1939]. Here, a superposition of independent GR-sources with lifetimes distributed on a wide time scale and amplitudes distributed like $\langle \Delta N^2 \rangle \propto 1/\tau$, is shown to yield a $1/f$ spectrum within the frequency range given by the reciprocal of the largest and smallest life times,

$$S_V = \sum_{i=1}^{N_t} \frac{\langle \Delta N^2 \rangle}{N_0^2} \frac{4\tau_i}{1 + (2\pi\tau_i)^2} \propto 1/f \tag{1.7}$$

where N_t is the number of traps.

Objections have been raised about the requirements; the wide distribution of time constants and the specific distribution of amplitude, but the required distributions have been explained in several ways.

Traps in the oxide with a uniform distribution of distance from the oxide-semiconductor surface [McWhorter, 1955b], in for example MOSFETs, yields the necessary distribution. Number fluctuations $1/f$ noise has therefore been called a surface effect, but van der Ziel [1974] pointed out how for example traps in space charge regions surrounding precipitates in the bulk of the sample can provide $1/f$ noise by equation (1.7) as well. D'yakonova et al. [1991] has proposed a model where an exponential tail of defect states near the conduction band causes the $1/\tau$ distribution. Dutta and Horn [1981] explains the $1/\tau$ distribution to be caused by an uniform distribution of activation energies.

Less attention has been paid to the requirement of independent traps, which has been pointed out in recent years [Hooge, 2003], where it is shown that interaction between traps causes the fastest trap to dominate, and the summation ceases to produce a $1/f$ spectrum.

1.2.8 Semiconductor Device Noise and Scaling

The demand for higher speed and lower cost in the semiconductor industry has led to an aggressive geometrical downscaling of devices. Higher density leads to more functionality on a smaller area at a lower cost.

Scaling has a tremendous impact on the low-frequency noise. This can be shown from the $1/N$ factor in the Hooge relation, since smaller geometries means lower number of carriers N. Also, it has been shown that the normalized current noise in MOSFETs

scales with $1/(WL)$, W and L being the width and length of the transistor [Vandamme et al., 1994]. For bipolar transistors, the normalized current noise scales with $1/A_E$, where A_E is the emitter area [Chen et al., 1998; Mounib et al., 1996; Deen et al., 1995; Markus and Kleinpenning, 1995].

Therefore, there might be a physical noise limit to geometrical downscaling of semiconductor devices. We shall see later in this thesis that the examination of very small SiGe HBTs, contradicts this statement.

Chapter 2

Polycrystalline Si and SiGe Thin-film Resistors

Chapter 2: Polycrystalline Si and SiGe Thin-film Resistors

In this chapter we compare the low-frequency noise from poly-crystalline thin film resistors with different germanium content and film thickness. These results were first presented at an international conference in India, and later published in Solid-State Electronics:

- X. Y. Chen, J. A. Johansen, C. Salm and A. D. van Rheenen. *On low-frequency noise of polycrystalline Ge_xSi_{1-x} for sub-micron CMOS technologies*. In *Proceeding of the International Conference on Communications, Computers & Devices (ICCCD)*, edited by S. L. Maskara and T. S. Lamba, volume I, pp. 187–190. Kharagpur, India, December 14-16, 2000b.

- X. Y. Chen, J. A. Johansen, C. Salm and A. D. van Rheenen. *On low-frequency noise of polycrystalline Ge_xSi_{1-x} for sub-micron CMOS technologies*. *Solid-State Electronics*, **45**(11): 1967–1971, 2001b.

2.1 On Low-frequency Noise of Polycrystalline SiGe for Sub-Micron CMOS Technologies

Abstract

Polycrystalline gate films of $Si_{1-x}Ge_x$ were deposited using low pressure chemical vapor deposition. To study the effects of different Ge contents on the noise properties, values of x = 0.0, 0.3, and 0.6 was selected. Samples of 300 nm and 500 nm thickness were prepared for comparing the thickness effects on the quality of the gate films. The gate films were implanted with different concentrations of boron. The morphology and electrical properties have been characterized using Atomic Force Microscopy, Transmission Electron Microscopy, and Hall-effect measurements. Conductance fluctuations were measured at room temperature. Here we present how low-frequency noise depends on the Ge contents, the doping concentration, and on the thickness of the gate film. The $1/f$ noise in polycrystalline $Si_{1-x}Ge_x$ can be analyzed in terms of mobility fluctuations caused by lattice scattering.

2.1.1 Introduction

In the past decade, serious efforts have been made to combine the best of silicon and germanium by using SiGe alloys in devices. This led to a new SiGe technology that is of great interest for microelectronics. The poly-$Si_{1-x}Ge_x$ technology makes it possible, (i) to offer a mid-gap gate material that is compatible with standard Si technology, (ii) to respond to technically emerging challenges as the dimensions of semiconductor devices are continuously scaled down into the deep sub-micron regime. The threshold voltage V_t of Metal Oxide Semiconductor Field Effect Transistors (MOSFETs) is limited by the off-current requirement. Downscaling requires increasing the doping concentration, which reduces the mobility and hence the device speed. This issue can be addressed by bandage engineering. The change of the gate-to-bulk work-function by using SiGe as a gate material can give the same V_t as for poly-Si gate material while keeping the doping level lower, thereby enhancing the channel mobility and saturation current. A mid-gap-work-function gate is also symmetrical for n-type and p-type MOSFETs. By varying the Ge fraction, the workfunction of poly-$Si_{1-x}Ge_x$ can be manipulated by 200-300 mV towards midgap. Technology issues, such as compatibility of gate material with thin gate oxide, with Si processing, and deposition of the poly-$Si_{1-x}Ge_x$ gate film with good electrical properties, have been extensively investigated in the last decade. However,

the noise properties of poly-$Si_{1-x}Ge_x$ were much less studied. The technological importance of polycrystalline $Si_{1-x}Ge_x$ has increased to the point where knowledge of noise properties is of value to the design and process engineer. For example, in microwave (telecom) and mixed mode analog-digital circuits, the low-frequency noise from transistors and resistors in the circuits affect, either directly, e.g. the design of low-noise amplifiers, or indirectly, by determining the phase noise of high-frequency oscillators and mixers. The conduction noise in the gate film of a MOSFET is known to have little effect on the noise in the drain current. However, in integrated circuits in which poly-$Si_{1-x}Ge_x$ gated MOSFETs are used, poly-$Si_{1-x}Ge_x$ resistors will also be included. Noise characterization of these layers may therefore be important. In addition, a noisy poly-$Si_{1-x}Ge_x$ gate film may point to poor material quality. The boron diffusion through the low-quality gate film down to the oxide layer can degrade the quality of the oxide layer. This will result in distributed space charges and defects in the oxide layer, and thus, a high noise level in the drain current. Here, we study low-frequency noise in polycrystalline $Si_{1-x}Ge_x$ film grown by low-pressure chemical vapour deposition (LPCVD). The results will be presented in terms of Ge contents, doping concentration and film thickness. Our results support the notion that mobility fluctuations are the origin of $1/f$ noise in polycrystalline materials.

2.1.2 Characteristics of The Gate Films

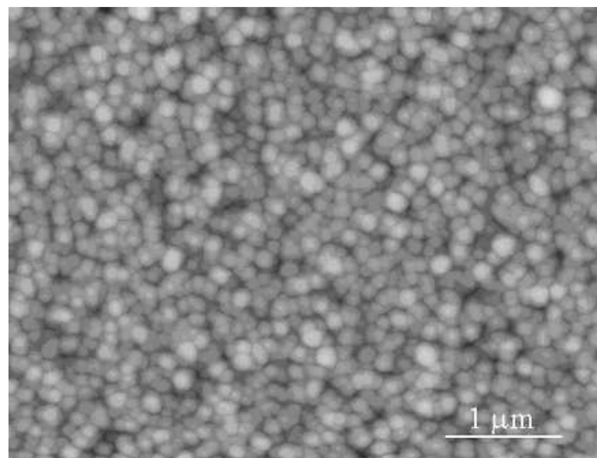

Figure 2.1: Atomic force microscopy picture of the surface

The gate films were deposited by LPCVD on thermal-oxide-covered (25 nm) n-type

Sample code	Ge fraction (%)	N_A (cm^{-3})	Ion beam (keV)	Thickness (nm)
30T500	30	$10^{18} - 10^{20}$	70	500
30T300	30	$10^{18} - 10^{20}$	40	300
60T300	60	$10^{18} - 10^{20}$	40	300
30T500	0	$10^{18} - 10^{20}$	70	500

Table 2.1: Sample specifications

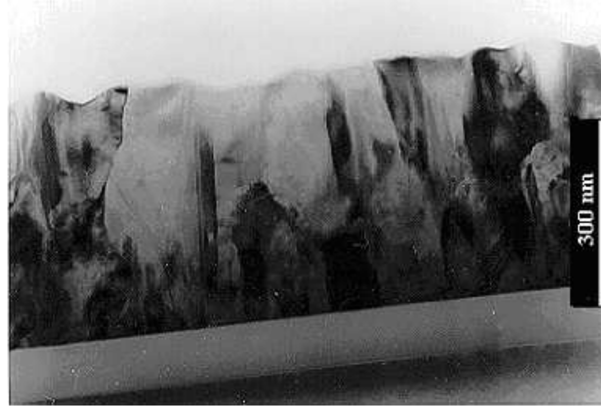

Figure 2.2: Transmission electron microscopy picture of the cross-section

Si wafers. Silane (SiH_4) and germane (GeH_4) were used as source materials in the LPCVD process. This process was optimized with respect to the texture and morphology of the poly-SiGe layer. Detailed information of the growth can be found in [Chen et al., 1999]. To study the effects of material composition different Ge fractions were selected: x = 0.0, 0.3, and 0.6. It is widely believed that the compatibility with Si technology reduces for Ge fractions larger than 0.6. It is typical that the electrical properties of poly-SiGe film are very sensitive to the morphology of the film which varies with film thickness. Therefore, samples of 300 nm and 500 nm thickness were prepared for comparison. The 300-nm-thick samples were implanted with 40 keV BF^{2+} ions, and then annealed in two steps for a total of 30 min at 850°C. First the samples were annealed in an O_2 ambient for 5 min to form a thin oxide layer to prevent out-diffusion of the dopants and then in an N_2 ambient for 25 min. The 500-nm-thick samples were implanted with 70 keV BF^{2+} ions, and annealed at 800°C for 60 min. The annealing ensures a homogeneous doping distribution throughout the film. Figure 2.1 and figure 2.2 shows typical microphotographs of our samples with a homogenous distribution of ver-

Sample	N_A (cm^{-3})	μ_H (cm^2/V s)
Poly-SiGe [Chen et al., 1999]	1×10^{19}	18.1
Mono-SiGe [King et al., 1990]	1×10^{19}	84
Lattice scattering in SiGe [King et al., 1990]		260

Table 2.2: Mobilities in the samples

tical columned structures. Such a structure is the best one for the gate of CMOS devices. The average column diameter, which is weakly dependent on the doping level, is about 170 × 55 nm. Table 2.1 lists the pertinent details of the samples we used. The samples were lithographically defined as two crossing bars (see figure 2.3). Each of the bars has a length of 3.0 mm and a width of 0.5 mm. Measurements of the Hall effect yielded a Hall concentration of 0.7 times the doping concentration and mobility values varying from 11 to 33 cm^2/Vs. In our calculation the Hall scattering factor of mono-Si was used because alloy scattering in $Si_{1-x}Ge_x$ is negligible [Manku et al., 1993]. To analyze the effects of the grain-boundaries on the transport of carriers in the poly-SiGe, we list in table 2.2 the hole mobility in doped mono-crystalline and poly-crystalline SiGe, and the hole mobility limited by lattice scattering only. We see that in mono-crystalline SiGe the mobility is about 80 cm^2/Vs at a doping level of 10^{19} cm^{-3}, while at this doping level the mobility of poly-SiGe is only about 18 cm^2/Vs. Therefore, in our samples the grain boundaries strongly limit the charge transport.

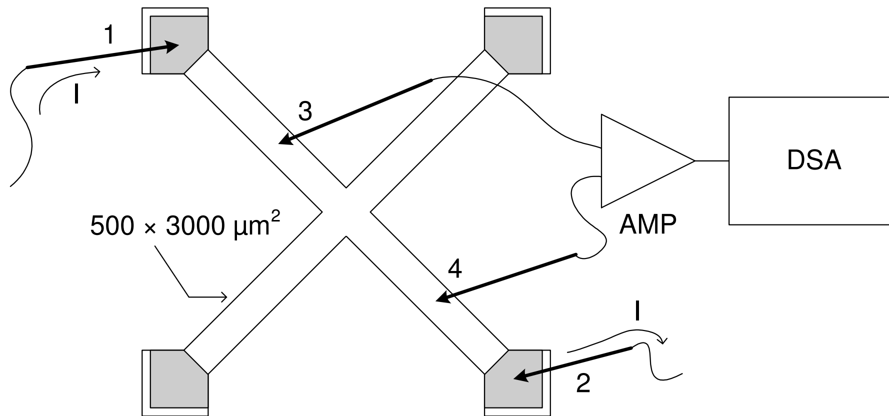

Figure 2.3: Sample structure and probing configuration. 1 and 2 are current contacts, 3 and 4 are noise measurement contacts

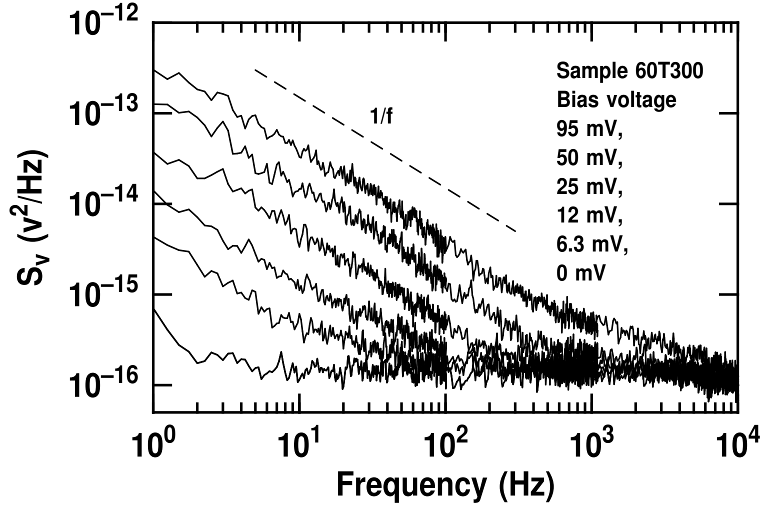

Figure 2.4: Noise power spectral density measured from 60T300 doped at 10^{19} cm^{-3}. From top to bottom, the bias voltage is: 95, 50, 25, 12, 6.3, and 0 mV. The dashed-line is for guiding the eyes.

2.1.3 Low-frequency Noise Measurement and Results

We used a femto-ampere DC level triaxial probe system together with an HP semiconductor parameter analyzer 4155A to make I-V measurements. In addition to probing the contacts of the gate film, we connected a probe to the triaxial chuck surface. Measurements of current through this probe revealed a significant leakage from the gate film to the substrate in some of samples. Therefore, as a first step samples without this type of gate leakage were selected from the wafers for noise measurements. Those selected samples have a linear I-V characteristic over the voltage region from -7 V to $+7$ V. We measured voltage fluctuations using the four-point method as shown in figure 2.3. The current passed through one pair of contacts while the noise voltage is measured with another pair of contacts. Most noise measurements revealed pure $1/f$ spectra. Only sample 30T300 doped at 10^{19} cm^{-3} exhibited components associated with generation-recombination (GR) noise in addition to $1/f$ noise. Typical noise power spectra are presented in figure 2.4. Even though some minor GR contributions may be present (most pronounced at 50 mV) good estimates for the upper limit of the $1/f$-noise magnitude can be extracted. The noise power spectral density scales with the voltage squared for all samples. The largest operating voltage, 95 mV, corresponds to a current density of 8.5 A/cm^2. To compare the noise level in different samples, we express the $1/f$ noise by

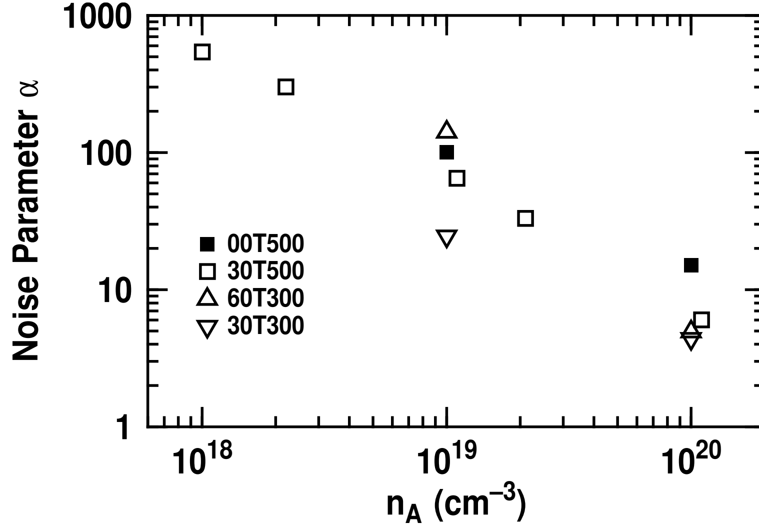

Figure 2.5: Noise parameter α vs. doping concentration. (■) 00T500, (□) 30T500, (△) 60T300, (▽) 30T300

the empirical Hooge relation, [Hooge et al., 1981],

$$\frac{S_V}{V^2} = \frac{S_R}{R^2} = \frac{S_G}{G^2} = \frac{\alpha}{f N_H} \tag{2.1}$$

where V is the voltage, R the resistance and G the conductance, S_X is the noise power density of the quantity X, α is the noise parameter, f is the frequency, and N_H is the total number of carriers in the volume involved in the noise generation. This relation was proposed to quantify the $1/f$ noise in homogeneous samples. In the situation where the noise generators are not homogeneously distributed, N_H is an effective number of carriers. Neglecting the complications of inhomogeneity associated with the granular morphology, we calculate α using as-measured Hall concentrations. We have to stress that this α does not have the meaning originally proposed by Hooge et al. [1981]. The analysis of the origin of the noise in any polycrystalline material cannot be carried out using the value of this α only. Nevertheless, such an α is a good measure of the relative magnitude of the noise in different gate films. The dependence of the noise on Ge content and boron doping concentration has been obtained. The noise parameter α of the gate films is depicted in figure 2.5. We found that decreasing boundary scattering at higher doping concentration results in increased mobility, and decreased $1/f$ noise parameter α. It is clear that the noise properties of poly-SiGe are comparable with that of poly-Si. At a very high doping level (10^{20} cm^{-3}), the poly-SiGe gate film with 60% of

Ge does not appear to be very noisy when compared with the 30% Ge film. However, at a doping level of 10^{19} cm^{-3} the poly-SiGe film with 60% of Ge is quite noisy. The noise levels of thicker gate films doped with higher energy ion beam are slightly higher than the noise levels in thinner gate films doped with lower energy ion beam. This may be related to better homogeneity of the thinner gate films. In addition, the thinner films are implanted at lower energies, reducing the amount of incurred lattice damage.

2.1.4 Discussion

The gate leakage results from the processing related damage/degradation of the 25-nm oxide layer under the gate films. The noise measured from those samples would not give any information on the noise in poly-$Si_{1-x}Ge_x$ gate films. First, trapping-detrapping of holes in the gate film via defects in the damaged/degraded oxide layer results in GR noise components or/and $1/f$-shaped contributions that add to the $1/f$ spectrum of the gate films, masking the fundamental $1/f$ noise. Second, the leakage path can form a parallel conducting channel in the substrate. From the noise measurements it is not possible to differentiate between contributions from the gate film and those from the parallel substrate channel. We observed that the noise in "leaky" devices is at least one order of magnitude higher than that in "good" devices. One cannot extract the $1/f$ noise of the gate films in these cases. In sample 30T300 the observation of high GR bumps is evidence of the imperfection of the oxide layer. Regarding the origin of the $1/f$ noise in polycrystalline materials, there are two competing models, similar to crystalline materials, namely the number fluctuations and the mobility fluctuations. Few investigations of noise in polysilicon can be found in the literature. de Graaff and Huybers [1982], Jang [1990], and Luo and Bosman [1990] reported on the $1/f$ noise of polysilicon. All three papers stated that the measured noise is caused by mobility fluctuations, although there were some disagreements. Luo and Bosman made corrections to the older model and proposed a more mature model. Madenach and Werner [1988] and Dimitriadis et al. [1998] presented an analysis in support of a typical number-fluctuation model. Especially Dimitriadis et al. [1998] claimed that the origin of the noise in intrinsic polysilicon is related to fluctuations in the free carrier density due to trapping-detrapping via gap states. They assumed two types of trapping states: mid-gap states with a uniform energy distribution and gap states in the exponential band tails. Such a distribution of trap states has never been experimentally verified. The model also cannot explain the doping dependence of the noise that we observed in figure 2.5. Of course their model was applied to intrinsic samples, whereas ours are

(heavily) doped.

More recently we presented a detailed analysis of the $1/f$ noise in poly-SiGe gate films to distinguish between the $1/f$ noise from grain-boundaries, depletion region, and neutral region of the grains [Chen et al., 1999]. It was concluded that the $1/f$ noise is generated in the depletion region of the grains. Inside the grains we can apply the lattice scattering model [Hooge et al., 1981] for the $1/f$ noise because the grains themselves are crystalline. As a result, we have,

$$\alpha_g = \left(\frac{\mu_g}{\mu_{Latt}} \right)^2 \alpha_{Latt} \tag{2.2}$$

where α_g is the Hooge parameter for the crystal grains in the poly-SiGe film, and μ_g is the mobility in the crystal grain, α_{Latt} is a material constant characterizing the $1/f$ noise due only to the lattice scattering. Thus, α_{Latt} has the same value in the depletion region (at the grain boundary) and neutral region of the crystal grain. Based on equation (2.2), we derived the following relation between the measured α and the doping concentration n_A (for detail, see the derivation of equation 22 in [Chen et al., 1999],

$$\alpha \propto n_A^{\lambda} \tag{2.3}$$

where λ varies from 0.7 to 0.8. Our experimental results in figure 2.5 show that λ is in this predicted range and independent of the Ge content. Therefore, the noise measurements on samples with different Ge contents, different doping concentrations, and different thicknesses support the mobility fluctuation model.

2.1.5 Conclusions

The noise properties of poly-$Si_{1-x}Ge_x$ are comparable with that of poly-Si. The noise in the poly-$Si_{1-x}Ge_x$ gate films is independent of the Ge mole fraction for $0 \leq x \leq 0.6$. The thickness of the gate film has only a minor effect on the noise magnitude: the thinner samples are slightly more quiet. We found that decreasing boundary scattering at higher doping concentration results in increased mobility, and decreased $1/f$ noise parameter α. The origin of the noise is the mobility fluctuations.

Chapter 3

Poly-Si- and Poly-SiGe-gated Field Effect Transistors

In this chapter we compare the low-frequency noise of silicon based field-effect transistors with poly-crystalline gates, made from silicon and silicon-germanium. This chapter is based on results published at the international noise conference in Florida:

- J. A. Johansen, H. Figenschau, X. Y. Chen, A. D. van Rheenen and C. Salm. *Low frequency noise in poly-Si- and poly-SiGe-gated MOSFETs*. In *Proceedings of the International Conference on Noise in Physical Systems and* $1/f$ *Fluctuations (ICNF)*, edited by G. Bosman, pp. 161–164. Gainesville, FL, USA, October 22-25, 2001.

Few investigations focus on the effect of alternative gate materials on the noise performance of MOSFETs. A recent comprehensive review article [Simoen and Claeys, 2002] on low-frequency noise in MOSFETs refers to our work as one of two studies dealing with the influence the gate material has on noise, ours being the only using silicon-germanium gates.

3.1 Low-frequency Noise in Poly-Si- and Poly-SiGe-gated MOSFETs

Abstract

We compare the low-frequency noise performance of poly-Si and poly-SiGe gated silicon MOSFETs. Both P-MOS- and N-MOS-transistors are studied. For P-MOS devices, the $1/f$ noise level versus drain current is about 2 orders lower than for N-MOS of equal size and operating at similar drain currents in saturation mode. The noise level of the P-MOS devices with a poly-SiGe gate is found to be lower than that of devices with a poly-Si gate, whereas for N-MOSFETs the noise level is found to be comparable for both gate materials. Our analysis suggests that the measured noise in the N-MOSFETs is caused by number fluctuations, whereas the noise in P-MOSFETs is caused by mobility fluctuations.

3.1.1 Introduction

Among the approaches for improving silicon-based MOSFETs is that of changing the material used as the gate electrode. Metal was replaced by silicon because it is more compatible with semiconductor processing because it has a much higher heat tolerance, for example. The semiconductor gate is degenerately doped, to increase conductivity and to reduce gate depletion effects. Since poly-crystalline material is can be doped at higher levels than crystalline material, poly-crystalline material has been the preferred choice.

Scaling of MOSFETs generally requires an increase in well doping density, to avoid short-channel effects, and reducing the lateral extension of the drain depletion region. Downscaling results in increasing $1/f$ noise and also a lower channel mobility caused by enhanced Coulomb scattering and transverse electrical fields. There is a trade-off between threshold voltage and achievable drive current [Simoen and Claeys, 2002].

In recent years, the silicon-germanium alloy has provided a way of doing band-gap engineering in silicon [Levitas, 1955]. This allows changing the work function of the gate [Hellberg et al., 1997], which directly affects the threshold voltage and provides an extra degree of freedom in designing MOSFETs, since changing the gate work-function allows on to achieve the same threshold voltage at a lower channel doping level [Ponomarev et al., 2000]. The lower channel doping level gives higher mobility and better current drive capability [Lee et al., 1999]. Since the band-gap change affects the valence

band edge energy level much more than the conduction band edge, only degenerately doped p-type material will give a significant change in work function as one increases the germanium content in the silicon-germanium alloy. Therefore, the devices used here are from a so called single gate technology where both P-MOS and N-MOS uses boron doped (p-type) poly-crystalline gates. It has been shown that for boron doping, the dopant activation is better for poly-SiGe than for poly-Si. A complete compatibility to standard CMOS is achieved without adverse effects on gate currents and oxide reliability [Salm et al., 1998].

Most designs utilizing the silicon-germanium gate take advantage of the tunable gate work function, and change the channel doping profile accordingly. Unfortunately, this makes it more difficult to compare the noise performance because more than just one device parameter changes. Here we compare devices with the same physical design, except for the gate material.

3.1.2 Devices

The devices used here are from a single-gate standard CMOS process where the gate material is changed from silicon to silicon-germanium, everything else left unchanged. This provides a way to gain insight into what influence the gate-material change itself has on device performance.

Si wafers are processed with a standard CMOS process. In the gate deposition step, the poly-Si or poly-SiGe gate material is grown by low-pressure chemical vapor deposition (LPCVD) on 25-nm-thick silicon dioxide. Then the gate electrode is doped by boron implantation (4.0×10^{15} BF_2^+ cm^{-2} at 40 keV). This gives us two identical wafers except for the gate electrode materials. Both Atomic Force Microscopy (AFM) of the surface, and Transmission Electron Microscopy (TEM) of the poly-SiGe film cross section (see chapter 2), show that the polycrystalline grains are well organized vertical columns that reach through the gate film from the oxide and up to the surface. To ensure dopant activation and a homogenous doping profile, the gate film is annealed after boron implantation. Further details of the devices can be found in [Salm, 1997]. The impurities diffuse more easily along the grain boundaries than through the crystalline grains. This will cause the impurity atoms to reach down to the oxide along the grain-boundaries before the doping profile inside the grains is as homogenous as wanted [Lee et al., 1999]. Continued annealing until a homogenous doping profile is obtained can cause local boron penetration into the oxide layer at grain boundaries. Such oxide impurities will affect the threshold voltage. The columnar structure of the poly crystalline gate film

gives rise to a distribution of these oxide charges that will modulate the threshold voltage along the channel. This in turn modulates the thickness of the conducting channel, which may increase the noise in the current passing through the channel. This effect could depend on the properties of the gate material.

The device geometry chosen for the experiment has channel width $W = 20\ \mu$m, and channel length $L = 5.2\ \mu$m, and the oxide thickness is 25 nm. These are fairly large devices selected to avoid possible scaling-induced issues, such as short channel effects and statistical noise variation, that are not the focus of this experiment.

3.1.3 Threshold Voltage Extraction and DC Performance

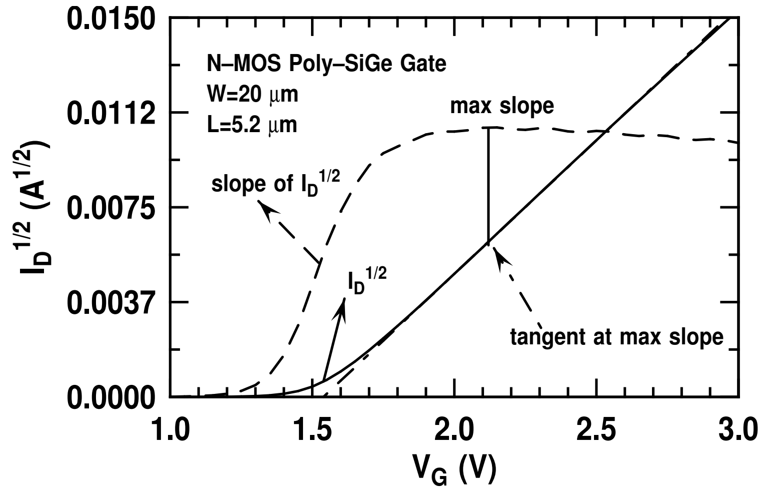

Figure 3.1: Determining the threshold voltage by the saturation current method.

In order to obtain comparable drain current at the same gate voltage overdrive, $|V_G - V_t|$, the threshold voltage V_t, has to be determined. This is done here by the saturation current technique [Schroder, 1998; Lee et al., 1982], which is an ASTM Standard F1096 [1996] technique based on the basic expression for saturation drain current [Sze, 1981],

$$I_{D,Sat} = \frac{mW}{L}\mu_{eff}C_{ox}(V_G - V_t)^2 \tag{3.1}$$

where m is a function of channel doping concentration, W is the channel width, L is the channel length, μ_{eff} is the effective channel mobility, C_{ox} is the gate capasitance, V_G is the gate voltage, and V_t is the threshold voltage to be determined. Plotting the square root of I_D versus gate voltage, and extrapolating at the maximum slope as shown in

figure 3.1, gives the threshold voltage at the point where the tangent intersects with the V_G-axis. The method assumes negligible series resistance and mobility degradation [Schroder, 1998]. Extraction of series resistance using the channel resistance method, gave values on the order of tens of Ohms. These series resistance values do not affect the extracted threshold voltage, and neither do they affect the measured noise.

After determining the threshold voltage for our set of 4 types of devices; N-MOS and P-MOS, with silicon and silicon-germanium as the gate material, we compare the sub-threshold current behavior as a measure to compare the extracted threshold voltages. Figure 3.2 shows the current versus gate voltage overdrive for all four types of devices. The sub-threshold current behavior shows that the extracted threshold voltage is consistent for all four device types, and hence is suitable for comparing relative differences in threshold voltage. Since we only want to compare the relative differences when changing the work-function of the gate material, the choice of method for extracting the threshold voltage is of little importance. The sub-threshold swing is the gate voltage necessary to change the current by one decade, and is given by [Sze, 1981],

$$S \approx \frac{kT}{q} \ln 10 \cdot \left(1 + \frac{C_D + C_{it}}{C_{ox}}\right) \tag{3.2}$$

where C_D is the depletion layer capacitance, C_{ox} is the oxide capacitance, C_{it} is the capacitance associated with interface traps. The sub-threshold voltage swing is around 90 mV/decade for these devices. From figure 3.2, we see that it does not depend on gate material. The device channel properties is not changed with gate material in these devices. The unchanged sub-threshold swing, indicates that the interface trap density controlling C_{it} in equation (3.2), does not change much when using SiGe instead of Si as the gate material.

From the current-voltage relationship in figure 3.3 we see that the current at the same gate voltage overdrive is larger for silicon-germanium gated devices. For P-MOS the change is about 20% and for N-MOS we find a change less than 10%, in saturation, at room temperature, with 1.5 V gate voltage overdrive.

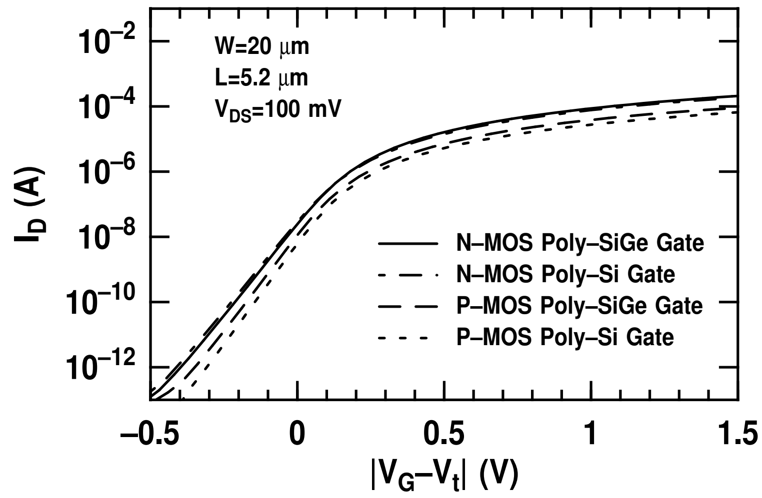

Figure 3.2: Sub-threshold current versus gate voltage overdrive

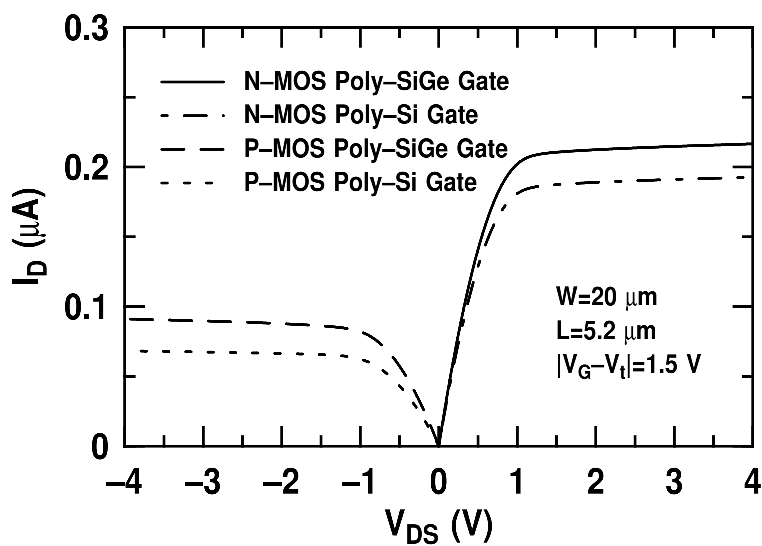

Figure 3.3: Current-Voltage relationship for MOSFETs

3.1.4 Drain Current Noise Level Comparison

Typical drain current noise spectra for the silicon-germanium N-MOS devices are shown in figure 3.4(a). Here we show the noise measured at V_G=3 V, for V_{DS}=0.1, 0.2, 0.4, 0.8, and 2.0 V. All devices exhibit $1/f$ noise spectra. In addition, at the lowest drain current, we can see that the $1/f$ noise reaches a thermal noise floor. At low frequency the noise at the three lowest drain currents, has a slope slightly larger than 1. For the highest drain current, a Lorentzian GR bump can be identified at around 10 kHz. The extracted $1/f$ noise level at 1 Hz at the different bias points is shown in figure 3.4(b). The noise is extracted by fitting a $1/f$ line to the spectra after removal of any identified GR-bumps and thermal noise floor.

The current noise S_I, in the linear regime can be expressed as follows [Vandamme et al., 1994],

$$S_I = \frac{\alpha q \mu^2 C_{ox} |V_G - V_t| V_{DS}^2 W}{f L^3} \propto |V_G - V_t| V_{DS}^2 \tag{3.3}$$

where α is the noise constant, μ is the channel mobility, C_{ox} is gate capacitance, $|V_G - V_t|$ is the gate voltage overdrive, V_D is the drain to source voltage, W is the channel width, and L is the channel length. Note that the use of α does not imply mobility fluctuations, but it is rather used as a relative measure of noise level in devices, regardless of the origin of the noise.

The proportionality of the noise in equation (3.3) with V_D^2 in the linear region of operation, can clearly be seen from figure 3.4(b), where the noise from the silicon gated N-MOS transistor is shown as an example. In the saturation region the current noise is expressed by [Vandamme et al., 1994],

$$S_{I,Sat} \cong \frac{\alpha q \mu^2 C_{ox} |V_G - V_t|^3 W}{2 f L^3} \propto |V_G - V_t|^3 \tag{3.4}$$

The saturation current noise is independent of the drain voltage. This can clearly be seen from figure 3.4(b) where the noise level becomes constant, and does not change when increasing V_{DS}, after reaching saturation.

Comparing the drain current noise level versus drain current for N-MOS transistors shows little change between devices with silicon gates and those with silicon-germanium gates. This is shown in figure 3.5. For P-MOS transistors, a difference in noise level can be seen (figure 3.6), with the silicon-germanium gated device being less noisy.

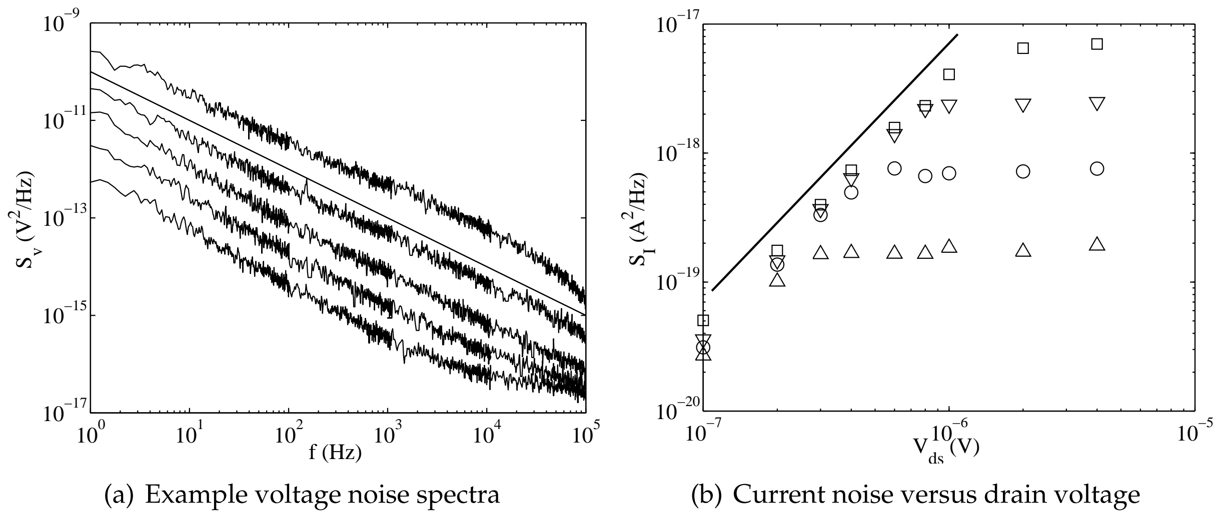

(a) Example voltage noise spectra

(b) Current noise versus drain voltage

Figure 3.4: Silicon gated N-MOS. (a) Example voltage noise spectra measured at $V_G = 3$ V. V_{DS} is from bottom to top, 0.1, 0.2, 0.4, 0.8, and 2.0 V. Line is proportional to $1/f$. (b) Current noise density versus drain voltage at 1 Hz at different gate voltages: ($\triangle$) $V_G = 1.8$ V, ($\bigcirc$) $V_G = 2$ V, (∇) $V_G = 2.4$ V, ($\square$) $V_G = 3$ V. The solid line has slope 2.

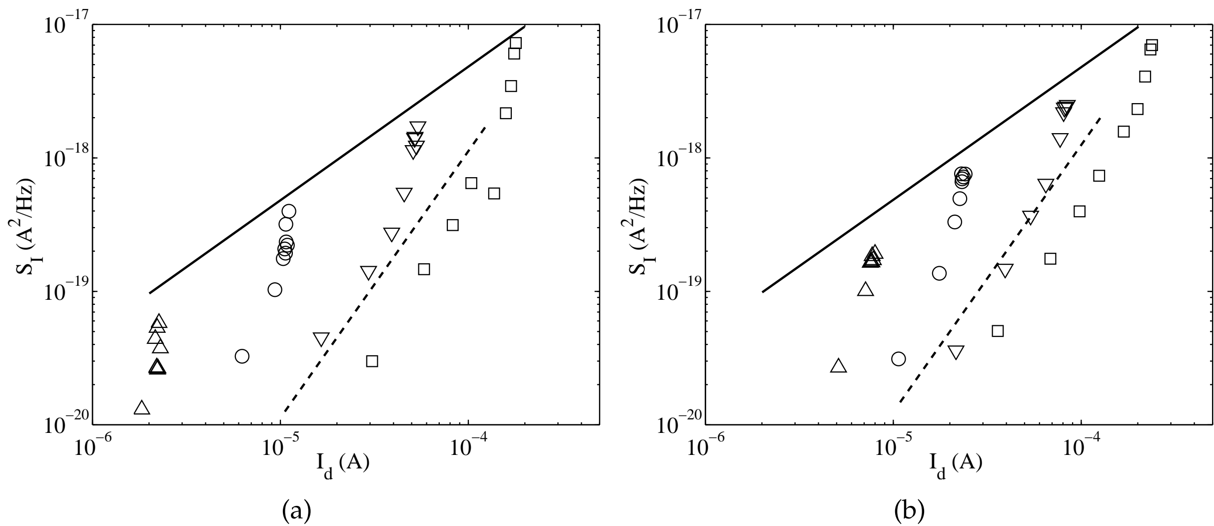

(a)

(b)

Figure 3.5: The N-MOS current noise density at 1 Hz at different gate voltages: ($\triangle$) $V_G = 1.8$ V, ($\bigcirc$) $V_G = 2$ V, (∇) $V_G = 2.4$ V, ($\square$) $V_G = 3$ V. (a) Silicon gated. (b) SiGe gated. The solid line has slope 1 and the dashed line has slope 2.

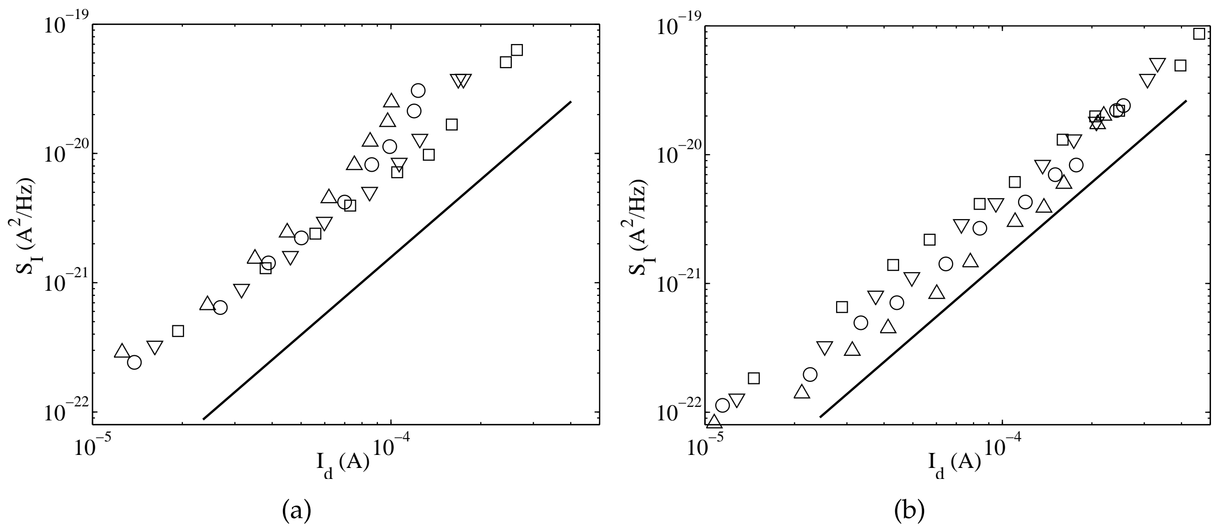

Figure 3.6: The P-MOS current noise density at 1 Hz at different gate voltages: (△) $V_G = 1.8$ V, (◯) $V_G = 2$ V, (∇) $V_G = 2.4$ V, (□) $V_G = 3$ V. (a) Silicon gated. (b) SiGe gated. The solid line has slope 2.

3.1.5 Analysis of Noise Origin

In this section we will attempt to find what fluctuating physical quantity causes the measured noise. We shall consider only the pure simplified number fluctuations and mobility fluctuations models. We will not consider the more refined models, such as the correlated-mobility-number-fluctuations model that was independently developed by Hung et al. [1990] and Ghibaudo et al. [1991], even though this correlated model is now widely implemented in simulator models. Note however, that there still exists some controversy about the validity of those models for some applications [Vandamme and Vandamme, 2000]. The analysis is based on noise in the saturation region, using the expected proportionalities of drain current noise and equivalent gate input referred noise on gate voltage overdrive.

Saturation Drain Current Method

Starting with the saturation drain current noise in equation (3.4) we find that the noise is proportional to the squared gate voltage overdrive $|V_G - V_t|^2$. To discriminate between mobility fluctuations and number fluctuations, we have to consider that in the number fluctuations model for MOS transistors, the noise parameter α can be shown to depend on the gate voltage overdrive [Vandamme and Penning de Vries, 1985] as follows,

$$\alpha \propto \frac{1}{|V_G - V_t|} \tag{3.5}$$

In the number fluctuations model, the noise is due to trapping and detrapping of carriers from slow surface states [Chang et al., 1994]. For the pure mobility fluctuations model, which is based on empirical observations of noise in homogenous samples [Hooge, 1976], α is regarded as a constant and does not depend on gate voltage overdrive. Inserting this into equation (3.4) yields a way to discriminate between number fluctuations and mobility fluctuations. For the number fluctuations model, we would then by combining equation (3.4) and equation (3.5) expect that,

$$S_{I,Sat} \propto |V_G - V_t|^2 \tag{3.6}$$

and for the mobility fluctuations model we still have,

$$S_{I,Sat} \propto |V_G - V_t|^3 \tag{3.7}$$

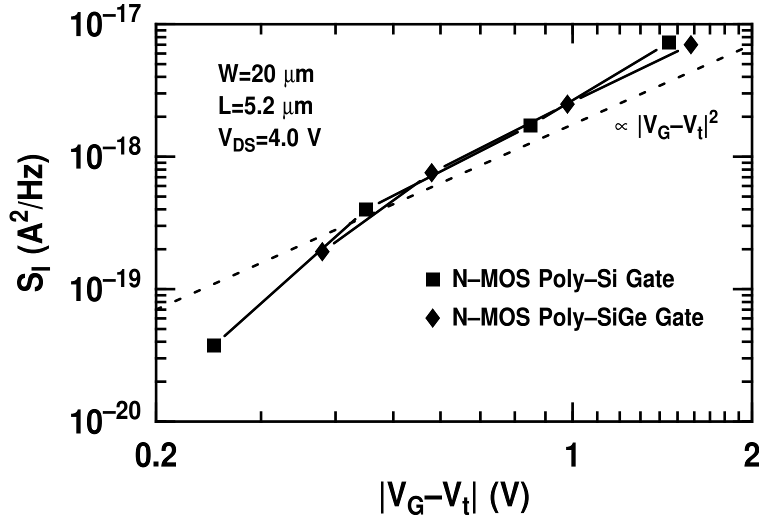

Figure 3.7: Channel current noise versus gate voltage overdrive on log-log scales for N-MOSFTEs with poly-Si- and poly-SiGe-gate. The dashed line has slope 2.

Figure 3.7 and figure 3.8 shows the channel current noise as a function of gate voltage overdrive on log-log scales. For N-MOS in figure 3.7, we can see that the noise scales with the square of gate voltage overdrive. Based on the above analysis, this points towards a number fluctuations origin of the noise, where trapping and detrapping of carriers close in the channel-gate oxide interface is responsible for the measured noise. In figure 3.8 we can see that the noise for P-MOS has a stronger dependence on gate voltage overdrive, and this points towards a mobility fluctuations origin of noise.

Gate Voltage Noise Method

Also the input referred gate voltage noise S_{V_G}, has been calculated and used as a measure for noise in MOS transistors, because the input referred noise is more suitable to compare the noise from devices in terms of circuit performance [Jacobson, 1997]. S_{V_G} is calculated from the channel current noise by the simple transconductance relationship [Vandamme et al., 1994],

$$S_{V_G} = \frac{S_I}{g_m^2} \tag{3.8}$$

where g_m is the transconductance given by [Sze, 1981],

$$g_m = \frac{\partial I_s}{\partial V_G} = \frac{2mW}{L} \mu_{eff} C_{ox} |V_G - V_t| \tag{3.9}$$

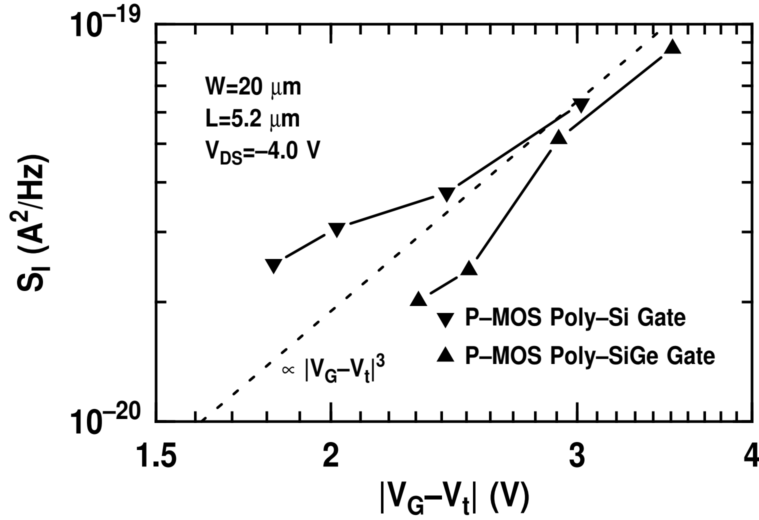

Figure 3.8: Channel current noise versus gate voltage overdrive on log-log scales for P-MOSFTEs with poly-Si- and poly-SiGe-gate. The dashed line has slope 3.

Then for the input referred gate voltage noise we may use the following indicators to distinguish between the models. For the number fluctuations model we find that by combining equations 3.6, 3.8, and 3.9,

$$S_{V_G} \propto |V_G - V_t|^0, \; i.e., constant \tag{3.10}$$

for the number fluctuations model, and by combining equations 3.7, 3.8, and 3.9,

$$S_{V_G} \propto |V_G - V_t| \tag{3.11}$$

for the mobility fluctuations model. Hence, if we observe that the input referred voltage noise is independent of gate voltage overdrive, the noise must originate from number fluctuations. On the other hand, if the input referred voltage noise depends on gate voltage overdrive, mobility fluctuations must cause the noise. These conclusions has been drawn by several independent studies, e.g. by, [Vandamme et al., 1994; Brini, 1998; Chang et al., 1994].

The input referred gate voltage noise is shown in figure 3.9 for N-MOS, and we see that it is independent of gate voltage overdrive. Hence, we conclude that number fluctuations cause the measured noise in N-MOSFETs. For P-MOS, however, we find that the input-referred noise depends on gate voltage overdrive, which is indicative of mobility fluctuations.

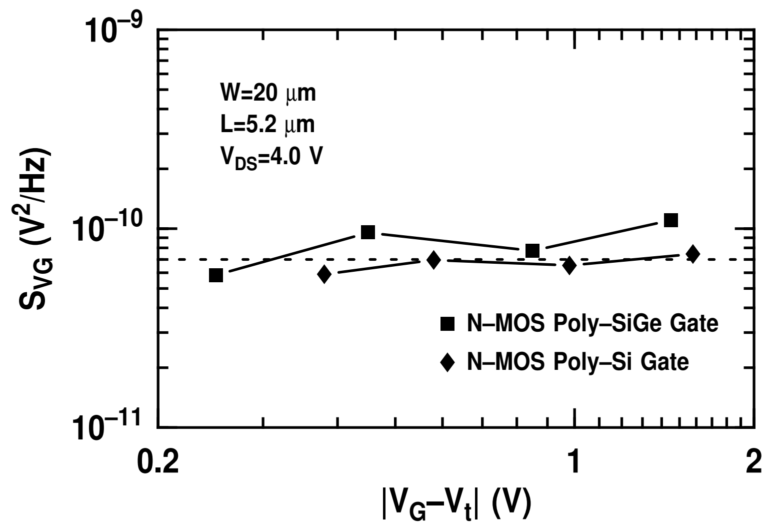

Figure 3.9: Input referred gate voltage noise versus gate voltage overdrive on log-log scales for N-MOSFTEs with poly-Si- and poly-SiGe-gate. The dashed line is constant, i.e, independent of gate voltage overdrive.

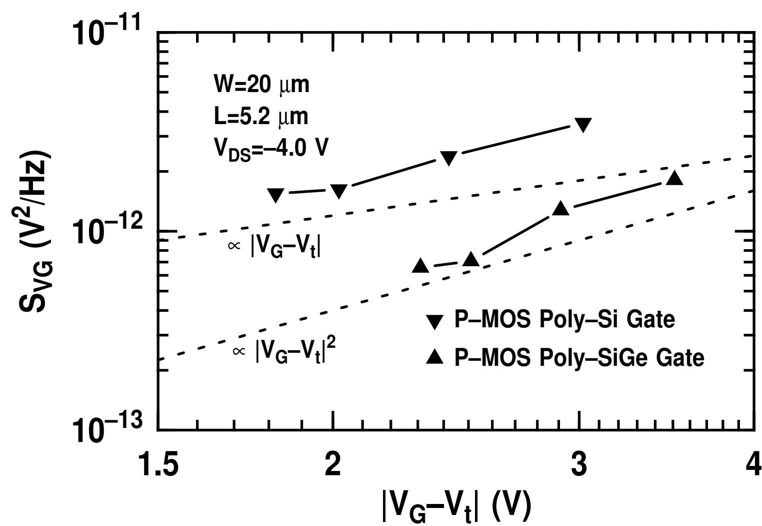

Figure 3.10: Input referred gate voltage noise versus gate voltage overdrive on log-log scales for P-MOSFTEs with poly-Si- and poly-SiGe-gate. The dashed lines has slopes 1 and 2.

3.1.6 Summary

We have compared the noise performance of N-MOS and P-MOS transistors with poly-Si and poly-SiGe as gate material. Output noise performance of N-MOS is independent of gate material, but for P-MOS we find slightly lower noise with a poly-SiGe gate as compared to the noise of a poly-Si gated device. Analysis of fluctuating physical quantities, based on the pure number fluctuations model and the pure mobility fluctuations model points towards mobility fluctuations for P-MOS, and number fluctuations for N-MOS.

Chapter 4

Quantum Well Semiconductor Lasers

In this chapter, we discuss results on low-frequency electrical noise in AlGaInP Quantum Well Lasers. We look into low-frequency noise source locations, and we discuss how the noise can be used as a non-destructive tool to probe device reliability. This chapter is a reformatted version of a conference paper presented at an international conference in China. My contribution to this work was mainly experimental:

- X. Y. Chen, J. A. Johansen and C. L. Liu. *Temperature dependence of low frequency electrical noise and reliability of semiconductor lasers*. In *Proceedings of SPIE, Semiconductor Optoelectronic Device Manufacturing and Applications*, edited by D. Chen, R. T. Chen, G.-Y. Wang and C.-C. Zhu, volume 4602, pp. 128–133. Nanjing, China, November 7–9, 2001a.

4.1 Temperature Dependence of Low-frequency Electrical Noise and Reliability of Semiconductor Lasers

Abstract

Measurements of low-frequency electrical noise (LFN) in quantum-well (QW) semiconductor lasers have been conducted using index guided AlGaInP lasers. To investigate the location and origin of the LFN in QW lasers, temperature dependence of the LFN is investigated over a wide range of injected current from 10^{-7} to 6×10^{-2} A, at temperatures between 0°C and 65°C. The effects of a short duration of burn-in process on the LFN have been investigated by measuring the LFN in the virginal device and the device after 20 hours stress (current I = 45 mA, temperature T = 40°C). We find, i) there are different noise mechanisms associated to the observed terminal current noise when laser diodes operate above and below threshold current; ii) it is much more clear to see the effects of the stress on the LFN versus injected current ($S_I - I_D$) than in current versus voltage ($I_D - V$) and optical-power versus injected current ($P_O - I_D$); iii) over a wide range of injected current, we did not observe a temperature dependence of the $1/f$, though different GR components appear in the spectra of the LFN measured at different temperatures. We have qualitatively analyzed the noise mechanisms and their location. We will also demonstrate that the noise measurement can be used as a diagnostic tool for the reliability of QW laser diodes.

4.1.1 Introduction

Semiconductor lasers are used extensively in telecommunications, optical storage, laser spectroscopy and optical sensing systems. In recent years, telecommunications and optical storage industries have experienced a fantastic development. The semiconductor laser market has been growing at ~20% per year in recent years, and even more is expected for the years to come. Reliability studies of semiconductor lasers becomes an important aspect from the following points of view: understanding failure mechanisms, improving the lifetime of semiconductor lasers, and developing a fast and non-destructive method to assess the reliability. The last point is extremely important to semiconductor laser industries to reduce the cost and time consumption spent in simplifying the expensive processes for reliable semiconductor lasers and in developing semiconductor lasers of high performance. The current method for predicting the lifetime of laser diodes is accelerated lifetime or burn-in testing, a statistical method that is

destructive, time consuming, and expensive. Adding to the above, systems that serve in harsh environments, such as in seabed and space, require 100% reliability assurance. In building such systems we cannot apply the traditional reliability concept that some lasers could offer extremely long lifetimes. We must select individual devices that have to meet specific system lifetime requirements. This is, in other words, asking for laser testing techniques to select the reliable units from a given batch of devices with confidence. First of all, it is a general fact that laser diodes cleaved from even adjacent areas of the same wafer may exhibit variation in degradation rate or lifetime by many orders of magnitude. Second, there are always several different failure modes [Chik and Devenyi, 1988] during laser degradation so that the burn-in testing certainly risks not screening out some individual devices with potential premature failure modes. Therefore, it may be worthwhile to study other methods that can detect all failure modes alone without any aging process or together with the burn-in testing in earlier aging phase. For example, we can investigate methods that use noise as a device-quality indicator. It is nondestructive, i.e., it does not consume the usable lifetime of the device [Vandamme et al., 1983]. With regard to semiconductor laser fundamentals such as transport mechanism, linewidth broadening and optical noise, the low-frequency electrical noise is of a great interest because of, for example, its strong correlation to optical noise [Fukuda et al., 1994; Ohtsu and Kotajima, 1984; Andrekson et al., 1986]. It is considered that an increase in $1/f$ noise in lasers causes an increase in its residual linewidth. The study of the electrical noise often leads to a better understanding of the transport mechanism of the free charge carriers, and hence to more insights in the physics of the systems [Weissman, 1996].

In this paper we use commercially available index guided AlGaInP lasers diodes emitting at 635 nm wavelength to investigate the LFN in QW lasers. The LFN has been measured over a wide range of injected current from 10^{-7} to 6×10^{-2} A, at temperatures between 0°C and 65°C. The effects of a short duration of burn-in process on the LFN have been investigated.

4.1.2 Noise Measurement as a Diagnostic Tool for Reliability of Laser Diodes

There are four important kinds of noise that are usually considered in semiconductor materials and devices, thermal noise, shot noise, generation-recombination noise (GR), and $1/f$ noise. Different noise spectra result from different physical processes. For example, locally crowding of current leads high thermal noise ($4kTR$). Carrier random

emission through barriers causes shot noise ($2qI$). Carrier interaction with phonons and interface states, scattered by defects gives rise to mobility $1/f$ noise [Chen, 1997; Hooge, 1994]. Carrier trapping and detrapping by mid-gap levels results in GR noise and number fluctuation $1/f$ noise. Most of these processes are believed to be the potential facts that can cause or accelerate failure of devices. Therefore, the noise strongly correlates with devices reliability. For semiconductor lasers, the $1/f$ noise and GR noise are the most important quality indicators.

Hooge's empirical relation provides a way to characterize the $1/f$ noise in homogeneous materials [Hooge, 1994],

$$\frac{S_G}{G^2} = \frac{S_R}{R^2} = \frac{S_V}{V^2} = \frac{S_I}{I^2} = \frac{\alpha}{fN} \tag{4.1}$$

where G is the conductance, R is the resistance, V is the voltage, I is the current, N is the total number of current carriers in the volume involved in the generation of the $1/f$ noise, f is the frequency, and α is the Hooge parameter. Without giving the physical origin of $1/f$ noise, this empirical relation does imply that the electrons contribute to the $1/f$ noise independently. The number of free charge carriers in the noise generation area is a determinant fact to the magnitude of the $1/f$ noise. It is a common experience that $1/f$ noise is material quality sensitive. Irradiation damage to, and annealing restoration of the material can vary the noise level by several orders of magnitude [Chen and deFolter, 1997]. For long diodes, S_I is proportional to I_D^2 , with the carrier lifetime so that $1/f$ noise increases with increasing number of traps in the devices.

Traps and recombination centers are particular to semiconductors and semiconductor devices. The random trapping and detrapping of the charge carriers result in fluctuation in the number of free charge carriers N. Hence, the conductance fluctuates, e.g., GR noise. The power spectral density of GR noise is given by,

$$S_N = \langle \Delta N^2 \rangle \frac{4\tau}{1 + (2\pi\tau)^2} \tag{4.2}$$

where τ is the relaxation time of the generation-recombination process, $\langle \Delta N^2 \rangle$ the variance of the fluctuations ΔN in the number of free charge carriers N, and f the frequency. The characteristic time constant τ is determined by the energy difference between conduction/valance band and the trap level at a constant temperature. The trap density N_t and the energy difference between the trap level and quasi-Fermi level determine the magnitude of the GR noise. Therefore, trap characteristics will be visible to the LFN

measurement.

Failure root-causes in semiconductor lasers are mainly mirror damage, dark line defects (DLDs), and dark point defects (DPDs). The mirror damage, if it does not extend to laser active range, is an optical failure that cannot be detected by any electrical characterization. The DLDs and DPDs are related to transport mechanism of free charge carriers in the devices. However, the current versus voltage characteristic is not sensitive to either of the microscopic processes. Measurements of the LFN on the other hand, are very sensitive to these processes. LFN spectroscopy can thus be an indicator of failure mechanisms even before aging starts. The noise spectra could reveal in situ potentially bad devices, devices whose lifetime is expected to be short.

4.1.3 Experiments and Results

Devices used in this work are commercial index guided AlGaInP lasers emitting at 635 nm (Sanyo SDL3038-33). Under CW operation, the laser diodes have typical light output P_O = 5 mW, threshold current I_{th} = 30 mA at 5 mW, and operating current I_{OP} = 40 mA at 5 mW. We used a temperature-controlled laser mount together with an HP semiconductor parameter analyzer 4155A to make $I_D - V$ measurements at 25°C on 40 index-guided lasers. The $I - V$ dependence of the lasers is showed in figure 4.1(a). SDL3308-33 lasers have the same $I_D - V$ dependence only when $V > 1.5$ V and $I_D > 10^{-5}$ A. Below 10^{-5} A, the $I_D - V$ dependence spans a wide range. 25 of the 40 lasers are good, and have very similar $I - V$ dependence as noted by No.1 in figure 4.1(a). Since the dependence spans in a wide range (see figure 4.1(a)), we chose two lasers, the best lasers No.1 and the ”worst” lasers No.2 to measure optical power versus driving current at 25°C and 40°C. In contrast to the $I - V$ characteristic, optical power versus injected current was not significantly different for sample No.1 and No.2, see figure 4.1(b).

To see how the LFN differs for the best and the worst laser diodes, we measured the LFN over a wide range of injected current from 10^{-7} to 6×10^{-2} A at 25°C. The current noise of the semiconductor lasers was obtained by measuring the voltage noise across a bias-resistor that was connected in series with the laser diode. The value of the bias-resistor R varied with driving current to make an appropriate noise measurement. The details of the LFN measurement can be found in [Chen et al., 2000a]. In all laser diodes, measured noise spectra exhibited a $1/f^{\gamma}$ component with $1 < \gamma < 1.15$ at low frequencies and a white component at high frequencies. Sometimes, GR noise components appear. The typical current noise spectra measured at 25°C is shown in figure 4.2(a). We can see that the shape of the spectra varies with the injected current.

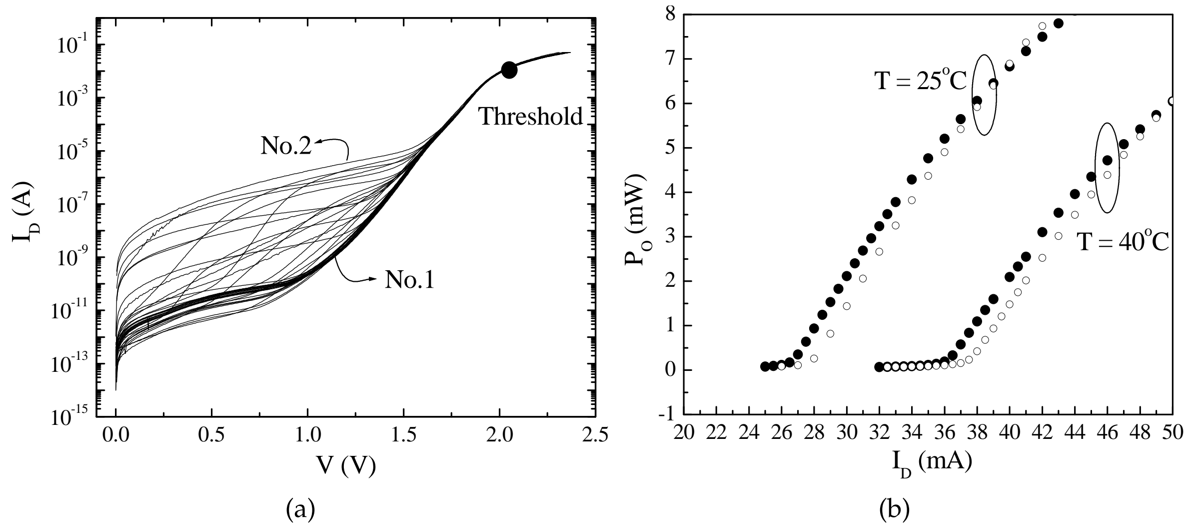

Figure 4.1: (a) $I_D - V$ dependence for 40 lasers. (b) Optical power versus I_D $\bullet$: No.1, $\circ$: No.2

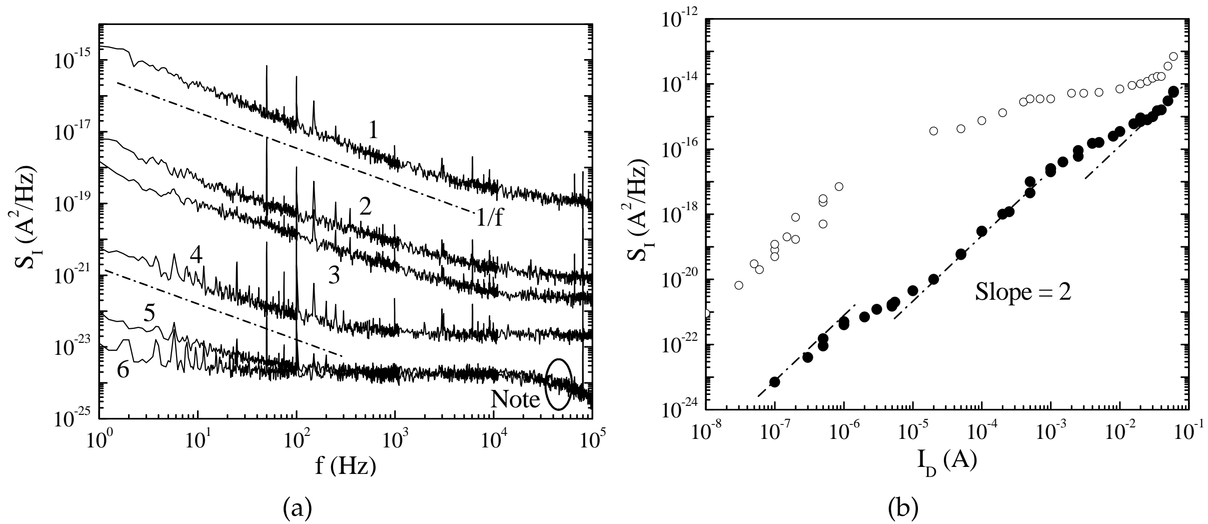

Figure 4.2: (a) Typical noise spectra of sample No.1 before the stress. The solid lines were measured with I_D = voltage/bias-resistor 1: 1V/20Ω , 2: 0.2V/1000Ω , 3: 0.5V/1000Ω , 4: 0.01V/1000Ω , 5: 0.0045V/9000Ω ,and 6: 0.0009V/9000Ω. Note: this is caused by cut-off frequency of preamplifier. The dash-dot lines are for guiding the eyes. (b) S_I versus I_D. $\bullet$: sample No.1, $\circ$: sample No.2. The dash-dot lines are for guiding the eyes.

The magnitude of $1/f^\gamma$, simply $1/f$ noise hereafter, is determined by subtracting the GR components and the white noise from the measured spectrum. Figure 4.2(b) shows the magnitude of current $1/f$ noise versus the injected current at 25°C for virginal laser diodes. It is clear that the noise behavior of the two devices is very different though the devices show only a small variation in optical power versus injected current.

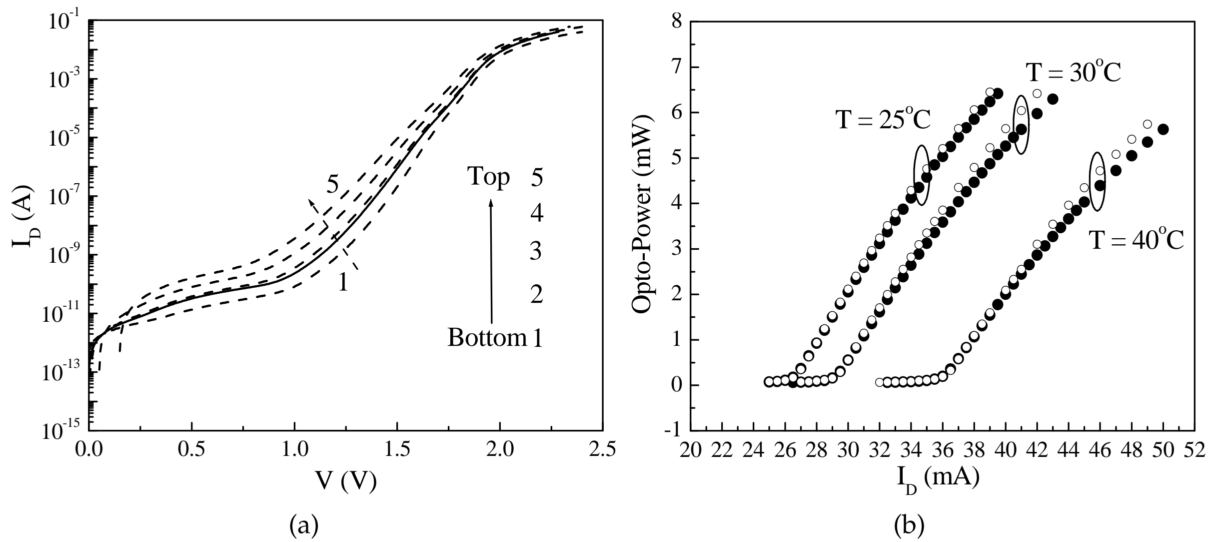

Figure 4.3: (a) $I_D - V$ dependence of sample No.1. The dashed lines were measured after the stress, the measurement temperature is 1: 0°C, 3: 25°C, 4: 45°C, and 5: 65°C. The solid line was measured before the stress, 2: 25°C (b) P_O versus I_D measured at different temperatures. • : before the stress, and ∘ : after the stress.

In order to study the effects of burn-in on laser properties, laser No. 1 is subjected to a short stress with a burn-in matrix (I_D = 40 mA, T = 40°C, t = 20 hours). The $I_D - V$ and $P_O - I_D$ of the laser diode before and after the stress are depicted in figure 4.3. Figure 4.4 shows the typical noise spectra after the stress and $S_I - I_D$ before and after the stress. It is clear that the stress affects S_I versus I_D a lot. However, the effects of the stress on $I_D - V$ and $P_O - I_D$ are negligible.

For better understanding the transport mechanism and origin of the LFN in laser diodes, we measured the LFN of No. 1 device after the stress at different temperatures, 0°C, 25°C, 45°C, and 65°C. Figure 4.4 shows some typical spectra measured at 25°C and $1/f$ noise level measured at different temperatures. The level of the $1/f$ does not change with temperature, though we see the difference in the shape of the spectrum measured at different temperatures.

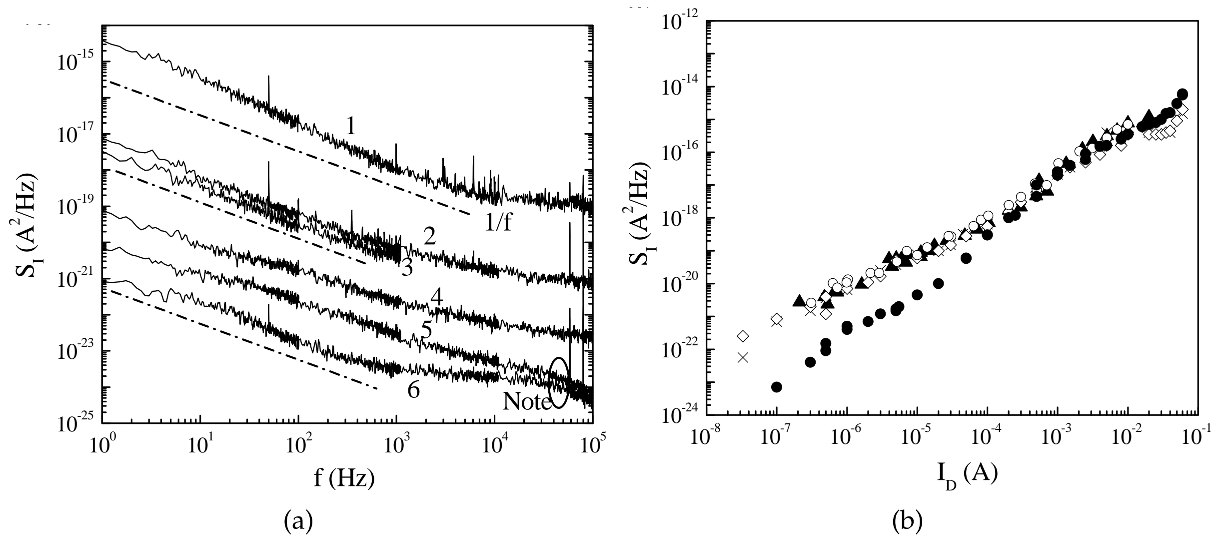

Figure 4.4: (a) Typical noise spectra of sample No.1 after the stress. The solid lines were measured with I_D = voltage/bias-resistor, 1: 1V/20Ω , 2: 0.3V/1000Ω , 3: 0.5V/1000Ω , 4: 0.01V/1000Ω , 5: 0.009V/9000Ω , and 6: 0.0009V/9000Ω . Note: this is caused by cut-off frequency of preamplifier. The dash-dot lines are for guiding the eyes. (b) S_I versus I_D of sample No.1 measured at different temperatures. Before the stress • : at 25°C. After the stress ▲ : at 25°C, ○: at 0°C, ◊ : at 45°C, × : at 65°C.

4.1.4 Discussion

The white noise here is contributed by the shot noise of the laser diode, plus the thermal noise from the circuit bias-resistors. The GR noise bumps above the $1/f$ noise spectra are from trap centers such as dislocations and point defects. The origin of $1/f$ noise can be the fluctuations of the mobility of charge carriers or/and the number of charge carriers. It is a general difficulty to determine which of the two noises is dominating. This would not be any issue for using noise as a quality indicator.

Comparing to the best lasers No.1, in lasers No. 2 we observed more GR noise components whose level and corner frequency depend on the magnitude of injected current. With regard to $1/f$ noise, laser No.2 has much higher level than laser No.1, and very different current dependence ($S_I - I_D$) from laser No.1. As shown in figure 4.1 and 4.2, at currents above 10^{-4} A, the $I_D - V$ curves of all lasers well overlap with each other. However, above this current level we observed clear differences in the LFN spectra and the magnitude of the $1/f$ noise between laser No.1 and No.2. More GR bumps and the high level of the $1/f$ noise indicate the poor quality of laser No.2.

The current dependence of the $1/f$ noise is different in different ranges of the driving current. Therefore, the LFN stems from different mechanisms when the lasers operate in different ranges of driving current. Roughly, free carriers in a QW laser diode transport following the sequence, injected from high doped contact part to the cladding layer, diffusing (probably together with drifting) through the cladding layer toward the confinement layer, diffusing and drifting in the confinement layer towards the QWs, caught and confined in the QWs, thermal emitting and quantum tunneling within the QWs, recombining in and escaping from the QWs. Because each part within the laser structure has very distinct characteristics, it makes different contributions to the terminal current noise. At low injection level, the contact part, or so-called series resistor will not be the noise source because of the high concentration of free charge carriers, see equation (4.1). The active region, e.g., the confinement and the QWs layer are probably candidates for the noise generators. With increasing injected current, a steady accumulation of free charge carriers in the QWs region decreases the $1/f$ noise until the $1/f$ noise generated from the cladding layer becomes significant. At medium injection level, noise from the cladding layer dominates. Noise from the series resistor will dominate at high injection levels above laser threshold current. Such a three-stage behavior is well demonstrated in figure 4.2(b).

After the short period burn-in process, we see the effects of the stress on the LFN. On the contrary, there is almost no change in $I_D - V$ and $P_O - I_D$ dependencies. From fig-

ure 4.2(a) and 4.4(a) we observed more GR components at low currents after the stress. The $1/f$ noise level increases at low and medium injection current only. Evidently, the burn-in process created damage to the device. Since the voltage mainly drops across the active region, the damage most likely locates in this part of the device. Therefore, as shown in figure 4.4(b) the noise will increase only at low and medium injection current. This is in agreement with the analysis in the above paragraph.

Measurements of temperature dependence of $P_O - I_D$, $I_D - V$ and LFN-I_D are shown in figure 4.3(a), 4.3(b) and 4.4(b). The thermal escape of carriers from QWs leads to an exponential temperature dependence of threshold current. This process does not generate any $1/f$ noise. Therefore, we did not see the temperature dependence of the $1/f$ noise.

4.1.5 Conclusion

Experimental evidence of the association between LFN and device reliability was presented. LFN in QW lasers is dominated by the $1/f^{\gamma}$ noise. Different noise mechanisms were observed when the laser diodes operate at different ranges of injected current. On the base of analyzing current transport mechanism in QW lasers, we find that above the laser threshold current, the $1/f$ noise, scaling with the square of driving currents, stems from the series resistance out of the active region. Below the laser threshold current, the $1/f$ noise arises from the laser active region. LFN measurement, but not $I_D - V$ and $P_O - I_D$ dependencies, can reveal the damage created by even a short burn-in process. The $1/f$ noise measurement can be used as a diagnostic tool for assessing the reliability of laser diodes. Measurement at low bias-currents can diagnose the degradation of the active region of the laser diodes, while measurement of the LFN at high injection currents can predict the quality of the cladding layers of the laser diodes.

Chapter 5

SiGe Heterojunction Bipolar Transistors

In this chapter, we discuss low-frequency noise in state-of-the-art silicon-germanium Heterojunction Bipolar Transistors [Cressler and Niu, 2003]. We look into scaling-induced noise variation, we use proton irradiation to add noise sources, and we find record-low noise levels that break the scaling trend of noise. This chapter is based on work done at Georgia Tech in close cooperation with Zhenrong Jin while I was on leave from the University of Tromsø. The chapter consists of a collection of recent conference and journal papers, and therefore some overlap in terms of results presented in the sections of this chapter is unavoidable:

- J. A. Johansen, Z. Jin, J. D. Cressler and A. J. Joseph. *Geometry-dependent low-frequency noise variations in 120 GHz f_T SiGe HBTs*. In *Digest of Papers, Topical Meeting on Silicon Monolitic Integrated Circuits in RF Systems (SiRF)*, edited by G. E. Ponchak, pp. 57–59. Grainau, Germany, April 9–11, 2003b.

- Z. Jin, J. A. Johansen, J. D. Cressler, R. A. Reed, P. W. Marshall and A. J. Joseph. *Using proton irradiation to probe the origin of low-frequency noise variations in SiGe HBTs*. In *Annual Nuclear and Space Radiation Effects Conference (NSREC)*. Monterey, CA, USA, July 21–25, 2003b.

- Z. Jin, J. A. Johansen, J. D. Cressler, R. A. Reed, P. W. Marshall and A. J. Joseph. *Using proton irradiation to probe the origin of low-frequency noise variations in SiGe HBTs*. *IEEE Transactions on Nuclear Science*, **50**(6): 1816–1820, 2003c.

- J. A. Johansen, Z. Jin, J. D. Cressler, Y. Cui, G. Niu, Q. Liang, J.-S. Rieh, G. Freeman, D. Ahlgren and A. Joseph. *On the scaling limits of low-frequency noise in SiGe HBTs*.

In *International Semiconductor Device Research Symposium Proceedings (ISDRS)*, pp. 12–13. Washington, DC, USA, December 10–12, 2003a.

- J. A. Johansen, Z. Jin, J. D. Cressler, Y. Cui, G. Niu, Q. Liang, J.-S. Rieh, G. Freeman, D. Ahlgren and A. Joseph. *On the scaling limits of low-frequency noise in SiGe HBTs. Accepted for publication in Solid-State Electronics*, 2004b.

5.1 Low-frequency Noise in 120 GHz f_T SiGe HBT's

Abstract

The influence of aggressive geometrical scaling on the variation of low-frequency noise in 120 GHz UHV/CVD SiGe HBTs, is presented for the first time. The noise variation shows a strong dependence on transistor geometry and little dependence on bias conditions. Our previous noise theory is used to understand this behavior, and a comparison is made between these new results and our prior results on 90 GHz peak f_T generation SiGe technology.

5.1.1 Introduction

Maintaining high f_T at low bias current levels mandates aggressive geometrical scaling of SiGe HBTs as the vertical profile evolves. It has recently been reported that scaled SiGe HBTs exhibit a large low-frequency noise (LFN) variation at small emitter geometry [Jin et al., 2002]. This small-size effect on LFN in SiGe HBTs is of potential concern in device modeling and circuit design. In our previous work, we presented preliminary results of this LFN size effect at a single fixed bias current on pre-production 90 GHz SiGe HBTs, an early precursor to a commercial 0.20μm 120 GHz peak f_T SiGe technology [Freeman et al., 1999; Joseph et al., 2001]. In the present work, we investigate the bias and device size dependence of this scaling-induced LFN variation in a fully-integrated 120 GHz SiGe technology, and compare the results with those on the earlier 90 GHz SiGe HBTs.

5.1.2 Experiment

The noise measurement setup is discussed by Jin et al. [2001]. Transistors with electrical emitter areas of $A_E = 0.82 \times 3.22\ \mu\text{m}^2$, $0.30 \times 1.86\ \mu\text{m}^2$ and $0.22 \times 0.66\ \mu\text{m}^2$ were measured, and are hereafter referred to as large, medium, and small devices. The transistor Gummel characteristics were ideal down to 10 pA for all of the transistors measured. The devices were biased at three base current densities, and for meaningful statistical comparisons, 7-8 transistors of each transistor size were characterized on separate die from the same wafer.

5.1.3 Results and Discussion

In figure 5.1, we compare the measured noise spectra from several samples of the small and the large geometry SiGe HBTs. The devices were biased at the same base current density to obtain a similar forward voltage bias on the base-emitter junction. The dotted lines in the figure represent the noise spectra from the individual devices, while the solid lines are the averaged spectra across all of the devices. We observe a large statistical variation of the LFN spectra between different samples of the small transistors, whereas the large devices show very similar LFN signature among different samples, consistent with our earlier results. The large transistors individually exhibit a $1/f$ dependence from 10-1000 Hz, and hence the average over all devices show the same frequency dependence. More interestingly, however, the small devices which individually show a strongly variable frequency dependence, also average to a straight-line $1/f$ LFN spectrum across this frequency range.

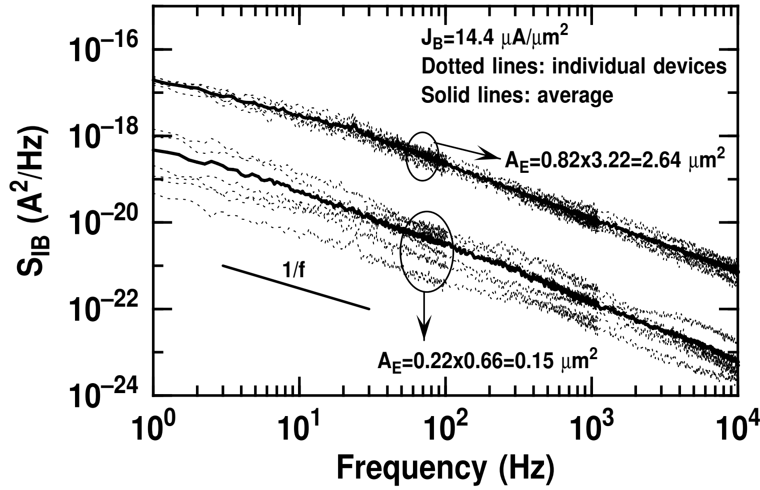

Figure 5.1: Statistical noise variation in the 120 GHz SiGe HBT technology at a fixed base current density. The upper solid lines is the average for large devices, and the lower solid line is the average for small devices. Dotted lines are the individual noise spectra

The variation in noise between the samples of the same geometry was quantified using the empirical relative standard deviation formula [Jin et al., 2002; Deen et al., 2002],

$$\delta = \frac{1}{S_{I_{B,avg}}} \sqrt{\frac{1}{N-1} \sum_{i=1}^{N} \left(S_{I_{B,i}} - S_{I_{B,avg}}\right)^2}$$

$$S_{I_{B,avg}} = \frac{1}{N}\sum_{i=1}^{N} S_{I_{B,i}}$$

where i indicates the $i'th$ sample, and N is the total number of samples. The noise variation dependence on base current density is shown in figure 5.2. The observed noise variation is not strongly dependent on base current density, and we can see only a slight increase in noise variation for the lowest current density for the smallest devices. This is consistent with our observation of the measured noise spectra, which only increase in magnitude, and not in shape with increasing bias current.

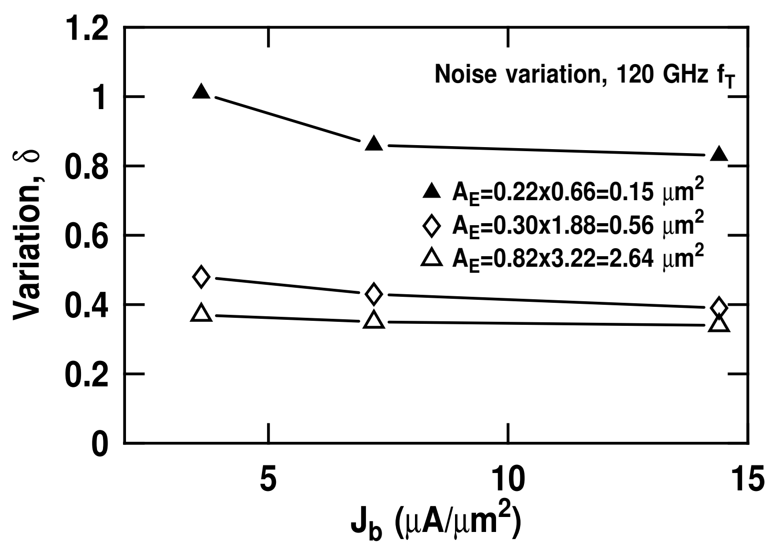

Figure 5.2: Noise variation as a function of bias current for 120 GHz HBTs, from top to bottom, for small, medium and large devices.

In figure 5.3 the noise variation dependence on emitter area is compared for both the 120 GHz and the 90 GHz SiGe HBTs. We can see that the noise variation increases as device size decreases, both within each SiGe technology generation, as well as between the two technology generations.

The noise was measured with the base current held constant from sample-to-sample. Due to small variations in the DC parameters, we observed slight variations in the base-emitter voltage needed to obtain the desired base current, and also a variation in the resulting collector current due to variations in the current gain across the wafer. The observed variation in current gain and V_{BE} was also calculated using the standard deviation formula. The DC parameters variation results are compared to the noise variation results in figure 5.3. The variations in the DC parameters are negligible compared to the

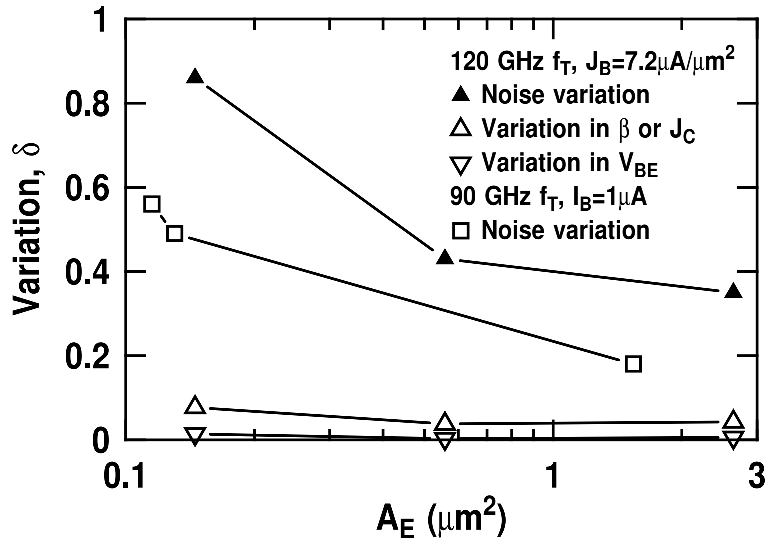

Figure 5.3: Noise variations versus emitter area for 120 GHz and 90 GHz SiGe HBTs, compared to DC parameter variation for 120 GHz HBTs.

large variation in the noise, and hence the observed geometry-induced noise variation is clearly not caused by variations in the transistor DC parameters alone.

Given the above indications, we believe that the observed small-geometry-induced noise variation in these 120 GHz SiGe HBTs is the result of a trap quantization effect, as detailed by Jin et al. [2002]. In this model, the noise mechanism is assumed to be due to the presence of GR trap centers, with differing characteristic time constants, each yielding a Lorentzian ($1/f^2$) noise spectrum. For a particular distribution of trap time constants, combining a large ensemble of independent traps results in a $1/f$ noise spectrum. Thus, for large devices with a sufficient number of traps, the resulting measured noise spectrum will be $1/f$ [McWhorter, 1955b]. For very small devices, however, the number of traps is not sufficient to produce a clean $1/f$ spectrum, and as one moves from one device to the next, a different noise spectrum results, producing a device-to-device variation. If, however, one averages the noise spectra over several small devices, the total number of traps will then be high enough to produce an average spectrum which is again close to $1/f$ (figure 5.1).

Figure 5.4 shows the normalized noise magnitude at $I_B = 1\mu$A for three SiGe HBT technologies with differing transistor-level performance (key properties of three generation SiGe HBTs is compared in table 5.1, including first generation with peak f_T of 50 GHz [Ahlgren et al., 1996]). In this case, the geometries of the transistors were chosen to be large enough to avoid any size-dependent effects, and hence facilitates a comparison

of the inherent noise differences between the various technologies. The data suggest that the device-level LFN capability degrades slightly when moving to higher performance levels, most likely due to the lower overall thermal cycles associated with the requisite vertical profile scaling, and hence the residual trap levels in the device. In all cases, however, the overall noise performance is far superior to both III-V and CMOS at comparable transistor performance [Escotte et al., 1998].

Table 5.1: Technology Comparison

Parameter	50 GHz	90 GHz	120 GHz
Lithography (μm)	0.50	0.20	0.20
Peak β	130	600	450
f_T (GHz)	50	90	120
f_{max} (GHz)	70	90	100
BV_{CEO} (V)	3.3	2.7	1.8
BV_{CBO} (V)	10.5	6.5	6.4
R_{Bi} (kΩ/sqr)	10	9.0	2.8

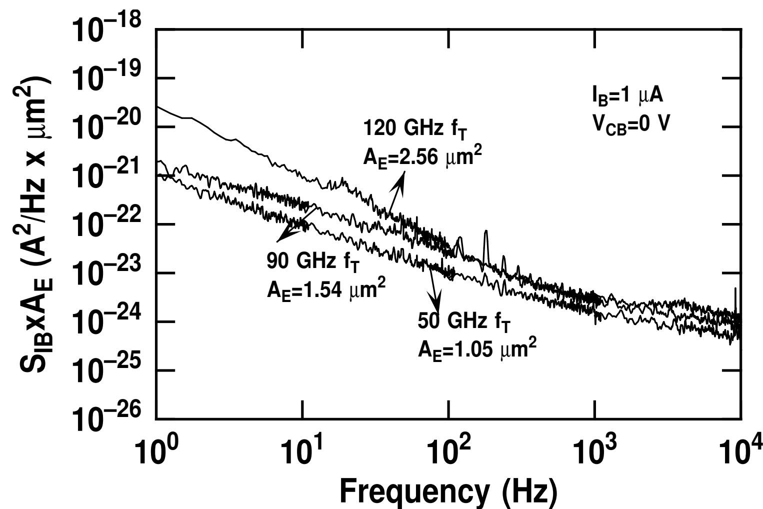

Figure 5.4: Noise spectra comparing different SiGe HBT technologies.

5.1.4 Summary

We have presented the low-frequency noise variation dependence on geometry and bias for 120 GHz SiGe HBTs. The noise variation shows a strong dependence on geometry,

but little dependence on bias. Both the noise magnitude and variation increase as the device and technology down-scales in size for higher performance. The resulting noise performance, however, remains superior to both III-IV and CMOS technologies at similar level of transistor performance.

Acknowledgment

This work was supported by a Fulbright Fellowship (J. Johansen), On Semiconductor, the SRC under Task 1022, Yamacraw at Georgia Tech, and an IBM University Partner Award. The wafers were fabricated at IBM Microelectronics, Essex Junction, VT. The authors would like to thank D. Harame, D. Ahlgren, G. Freeman, B. Meyerson, D. Herman, and the IBM SiGe team for their contributions to this work.

5.2 Proton Response of Low-frequency Noise in 120 GHz f_T SiGe HBT's

Abstract

We use proton irradiation to probe the origins of the geometry-dependent variation of low-frequency noise in 120 GHz silicon-germanium (SiGe) Heterojunction Bipolar Transistors (HBTs). Before irradiation, small-sized transistors show a strong variation in noise magnitude across many samples, whereas the noise in larger devices is more statistically reproducible. Although the noise magnitude shows little degradation after 2×10^{13} p/cm^2 irradiation, the observed noise variation decreases. Its dependence on both geometry and bias is quantified. This fundamental geometrical scaling effect is investigated using theoretical calculations based on the superposition of generation-recombination (GR) noise sources.

5.2.1 Introduction

SiGe HBT bipolar complementary metaloxide-semiconductor (BiCMOS) technology offers high-level integration, low cost, and high-speed, and is being increasingly used for mixed-signal circuit applications. Low-frequency noise (LFN) in transistors usually has a $1/f$-like spectrum, and sets the lower limit on the detectable signal level, not only in the low frequency range, but also at high frequencies via the up-conversion to the carrier frequency through the nonlinearities of the device (phase noise). Understanding LFN is thus a crucial design issue in direct-conversion receivers, oscillators, synthesizers, amplifiers, and mixers for digital, analog and optoelectronics applications.

Transistors are aggressively scaled (down-sized) in order to improve performance and integration level. One design issue associated with geometrical scaling is that the LFN often shows a different frequency dependence for each individual device [Sanden et al., 2002; Jin et al., 2002], and this can directly affect both circuit performance and accurate compact modeling. This LFN variation has been observed in BJTs and SiGe HBTs in very small-sized devices, and the fundamental mechanism is regarded to be the superposition of individual trapping/detrapping processes due to the presence of GR centers in the device [Sanden et al., 2002; Jin et al., 2002]. Each GR center contributes a Lorentzian-type ($1/f^2$) noise signature. Given a sufficient number of traps and a particular distribution of characteristic time constants associated with the GR centers, these Lorentzian processes combine to produce the observed noise behavior [McWhorter,

1955a]. At sufficiently small size, however, the total number of traps is small enough that non-$1/f$ behavior, and large statistical variations, can be observed. These trapping/detrapping processes modulate the number of carriers and, thus, are best described by number fluctuation theory [Sanden et al., 2002; Jin et al., 2002; McWhorter, 1955a; Uren et al., 1985; Kandiah, 1994; Vempati et al., 1996; Llinares et al., 1997; Lau et al., 1992; Deen et al., 1998; Chen et al., 1998; Plana et al., 1995; Markus and Kleinpenning, 1995; Mounib et al., 1995] instead of mobility fluctuation theory [Hooge, 1994; Kilmer et al., 1983; Vandamme et al., 1994; Kleinpenning, 1980; Vandamme et al., 1997].

In this work, we intentionally introduce additional traps into the transistor via proton irradiation in order to probe the physical origins of the observed LFN variations in 120 GHz SiGe HBTs. In addition, this work provides valuable information on whether such LFN variations are potentially important in space-borne communications applications.

5.2.2 Experiment

The transistors are from a fully integrated, commercially available 0.20 μm 120 GHz peak f_T SiGe technology from IBM [Joseph et al., 2001]. Since the dominant noise source in the common-emitter configuration is associated with the base current, the base current noise spectrum was investigated [Sanden et al., 2002; Jin et al., 2002; Vempati et al., 1996; Llinares et al., 1997]. The transistor was biased in a common-emitter configuration with V_{CB} = 0 V. The details of the noise measurement system can be found in [Jin et al., 2001]. Transistors with emitter areas (A_E) of 0.82 $\times$ 3.22 μm^2, 0.30$\times$1.86 μm^2 and 0.22 $\times$ 0.66 μm^2 were measured, and are hereafter referred to as large, medium, and small devices. For meaningful statistical comparisons, six transistors of each transistor size were characterized on separate die from the same wafer.

The samples were diced and attached to a ceramic holder and directly exposed with terminals floating to 62.5 MeV protons at the Crocker Nuclear Laboratory cyclotron located at the University of California at Davis. A total accumulated fluence of 2×10^{13} protons/cm^2 was used. Dosimetry measurements used a 5-foil secondary emission monitor calibrated against a Faraday cup. Ta scattering foils located several meters upstream of the target establish a beam spatial uniformity of 15% over a 2 cm radius circular area. Beam currents from about 5 pA to 50 nA allow testing with proton fluxes from 10^6 to 10^{11} protons/cm^2/s. The dosimetry system has been previously described in [Murray et al., 1991; Marshall et al., 1994], and is accurate to about 10%.

5.2.3 Measurement Results

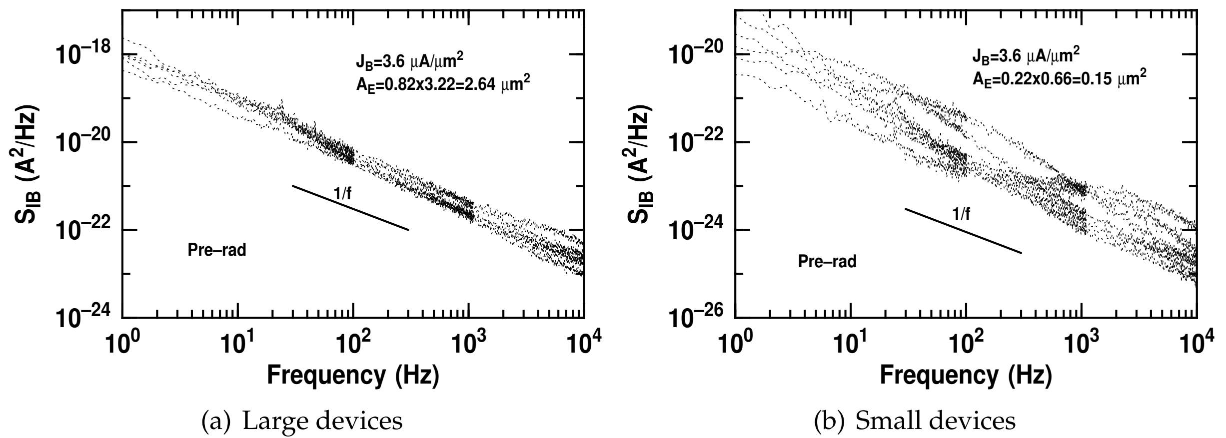

(a) Large devices (b) Small devices

Figure 5.5: Pre-irradiation noise from six large and six small transistors spectra at base current density J_B=3.6 μA/μm^2.

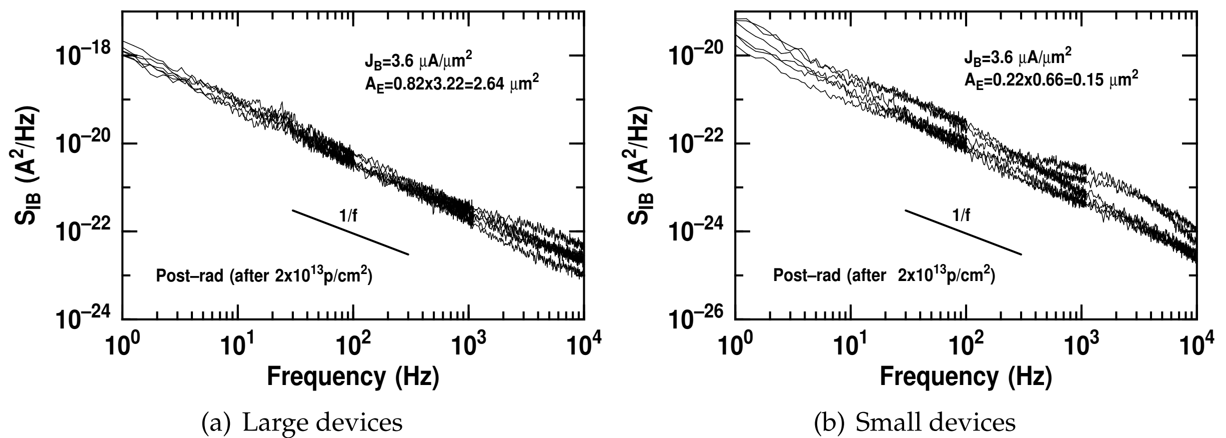

(a) Large devices (b) Small devices

Figure 5.6: Noise spectra from six large and six small transistors at base current density J_B=3.6 μA/μm^2, after 2$\times$10^{13} protons/cm^2.

In figure 5.5, we compare the measured noise spectra from six samples of small and large SiGe HBTs. The devices were biased at the same base current density (J_B) to obtain a similar forward voltage bias on the base-emitter junction. Observe that the noise spectra, shown in figure 5.5, exhibit $1/f^\alpha$ frequency dependencies with α close to but slightly larger than unity. This deviation from $1/f$ frequency dependence could be a result of thermally activated processes, as suggested by DuttaHorn model [Dutta and

Horn, 1981]. Interestingly, we observe a large statistical variation of the LFN spectra between different samples of the small transistors, whereas the large devices show a very similar LFN signature among different samples, consistent with our earlier results on a 90 GHz SiGe technology [Jin et al., 2002]. Post-radiation noise spectra of small and large SiGe HBTs are compared in figure 5.6. It is clearly seen that noise variation decreases for small devices, but remains nearly the same for large devices. The variation in noise at a spot frequency (a measured single frequency) between the samples of the same geometry was quantified using a variation coefficient (δ), given by the standard deviation formula [Sanden et al., 2002; Jin et al., 2002],

$$\delta = \frac{1}{S_{I_{B,avg}}} \sqrt{\frac{1}{N-1} \sum_{i=1}^{N} (S_{I_{B,i}} - S_{I_{B,avg}})^2} \tag{5.1}$$

$$S_{I_{B,avg}} = \frac{1}{N} \sum_{i=1}^{N} S_{I_{B,i}}$$

where i indicates the i'th sample, and N is the total number of samples (δ is then averaged over the measurement frequencies).

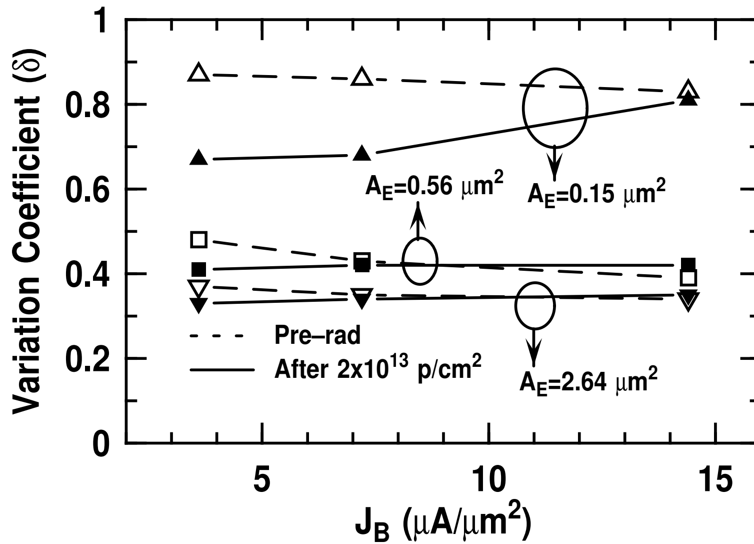

Figure 5.7: Noise variation for measured noise spectra versus J_B before and after irradiation. δ is an average value over the measurement frequencies.

The observed noise variation before proton irradiation is not strongly dependent on base current density, as can be seen in figure 5.7. This is consistent with our observation

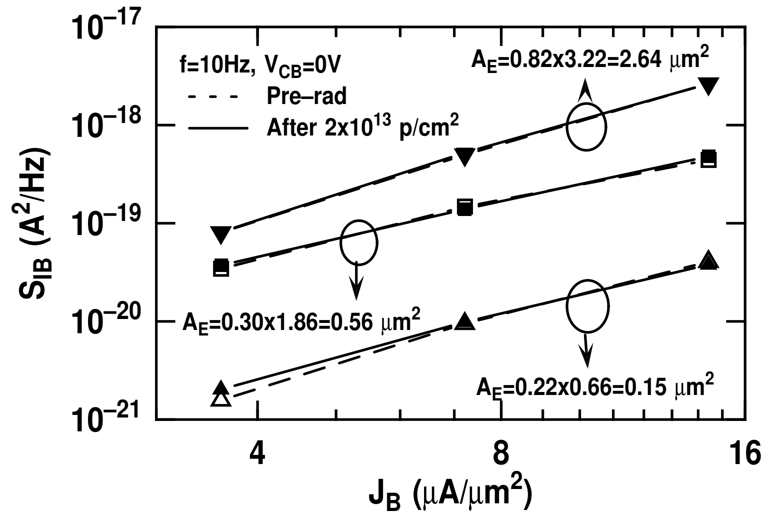

Figure 5.8: Noise magnitude versus J_B before and after irradiation.

of the measured noise spectra, which only increase in magnitude, and do not change in shape, with increasing bias current. After proton irradiation, however, the noise variation shows a significant decrease for the small devices, especially at low J_B, but shows a smaller decrease for the medium and large devices, as shown in figure 5.7. The noise variation thus now depends both on geometry and bias. It is clear that radiation exposure changes the noise variation in these SiGe HBTs. Interestingly, after irradiation, the average noise magnitude shows little degradation at the three bias current densities for the three geometries, as shown in figure 5.8. Furthermore, if we track the noise spectra of the pre- versus post-irradiated individual devices for the small transistors at low bias current, two of them show an observable noise magnitude change, while the others only show changes in noise spectral shape. This suggests that the changes in the pre- and post-radiation noise spectra is a random process, and should be captured by a statistical model.

The noise was measured with the base current held constant from sample-to-sample. Due to small variations in the DC parameters, we observed slight variations in the base-emitter voltage needed to obtain the desired base current, and also a variation in the resulting collector current due to variations in the current gain at a fixed base current from sample to sample across the wafer. The observed variation in current gain and was also calculated using the standard deviation formula. The results are shown in figure 5.9. The variation in the parameters is negligible compared to the large variation in the noise, and hence the observed noise variation is clearly not caused by variations

in the transistor DC parameters alone.

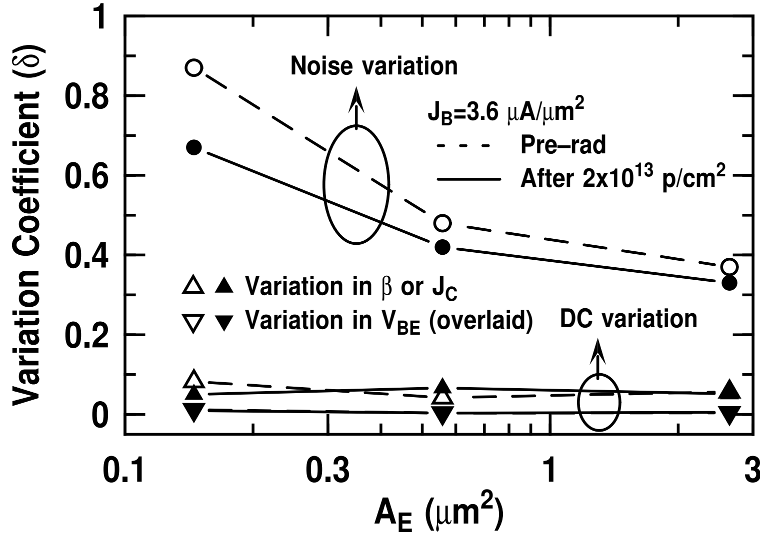

Figure 5.9: Noise and DC parameter variations from measured data versus A_E before and after irradiation

5.2.4 Model and Discussion

Pre-Radiation

An intuitive explanation for the physical basis of carrier number fluctuations in bipolar junction transistors (BJTs) depends on the trapping/detrapping of carriers by traps at the interfaces or oxide layers in the device [Deen et al., 1998]. The noise of each individual trapping/detrapping process theoretically exhibits a Lorentzian spectrum ($1/f^2$), which can be expressed as,

$$S_{I_B} = \alpha \frac{\tau}{1 + (1\pi f \tau)^2} \tag{5.2}$$

where α is the amplitude (with units of A^2) and τ is the characteristic time constant. The noise spectrum is flat at low frequencies and decreases as $1/f^2$ at high frequenies. The superposition of a large number of Lorentzian spectra with a $1/\tau$ distribution results in the usually observed spectrum [McWhorter, 1955a], as illustrated in figure 5.10. In [Jin et al., 2002], the $1/f$ noise in SiGe HBTs was expressed as the superposition of such Lorentzian noise sources. The pre-rad S_{I_B} depends on bias and geometry, as seen in figure 5.8. The best fit to the data shows a $A_E^{0.2} J_B^{2.4}$ dependence. Following the same

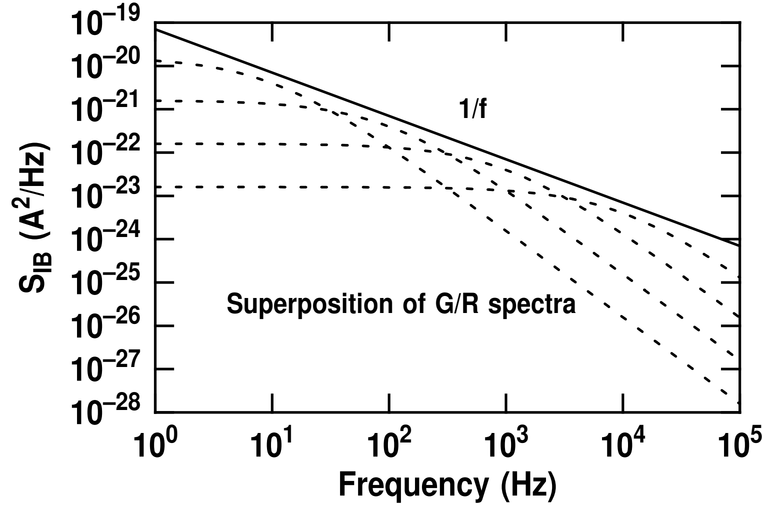

Figure 5.10: Superposition of Lorentzian (GR) spectra yields a $1/f$ spectrum if the number of GR traps in the summation is sufficiently large.

procedure outlined in [Jin et al., 2002], to obtain a best fit to the pre-radiation measurement data, an empirical expression of the low-frequency noise spectrum can be written as [Sanden et al., 2002; Jin et al., 2002],

$$S_{I_B} = \sum_{i=1}^{N} A \frac{A_E^{0.2} J_B^{2.4} \tau_i}{1 + (2\pi f \tau_i)^2} \tag{5.3}$$

where A is a constant, τ_i is the characteristic time constant of the i'th independent traps and has to be distributed as $1/\tau$ to produce a $1/f$ spectrum, and N_T is the total number of characteristic time constants associated with traps in the device and proportional to A_E. When N_T is large enough, which is the case in the large device, equation (5.3) yields a $1/f$ spectrum [McWhorter, 1955b]. When N_T is sufficiently small, corresponding to the small device case, the spectrum modeled by this equation will show a deviation from $1/f$ behavior. Five hundred different characteristic time constants were generated over the range $1/(2\pi \times 10^7)$ to $1/(2\pi \times 10^{-3})$ with a $1/\tau$ distribution. This number is by far large enough to ensure that the superposition of all, like in equation (1.7), gives a $1/f$ spectrum. To best fit the noise variation found by equation (5.1) from the experiments, three characteristic time constants were inferred for the small-sized device, 12 were inferred for the medium-sized device, and 50 were inferred for the large-sized device. In the calculation, characteristic time constants were randomly drawn from the previously generated 500 cases, which have a $1/\tau$ distribution, for every calculation of the small,

medium, and large devices $A = 1.1 \times 10^{-23}$.

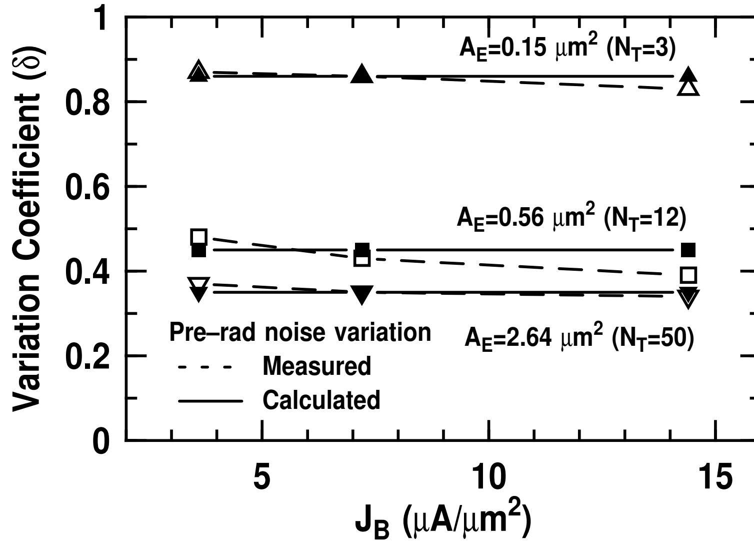

Figure 5.11: Noise variation from measured and calculated noise spectra versus J_B before irradiation. The number of traps N_T, used in the calculation, was inferred to match the experimental noise variation. N_T is indicated for each size.

Six individual calculations (to mimic the six independent measurements) were performed for each size device, and the resultant noise variation coefficient of the six calculated spectra is shown in figure 5.11, which is consistent with the measured data. The calculated noise variation is bias independent as expected from equation (5.1) and equation (5.3). These calculations indicate that a small number of traps indeed leads to the observed large noise variation in the small devices.

Post-Radiation

Proton irradiation generates traps at the $SiSiO_2$ interface [Rashkeev et al., 2001] at the E-B spacer around device emitter perimeter [Jin et al., 2001]. These traps create a non-ideal base current component due to increased space-charge region (SCR) GR center recombination current near the surface, as confirmed in figure 5.12. The DC degradation of SiGe HBTs after proton irradiation has been extensively investigated in [Cressler et al., 2002].

Assuming that the observed radiation-induced noise increase is mainly due to these peripheral traps, the radiation-induced LFN increase $S_{I_{B,SCR}}$ can be expressed as [Jin

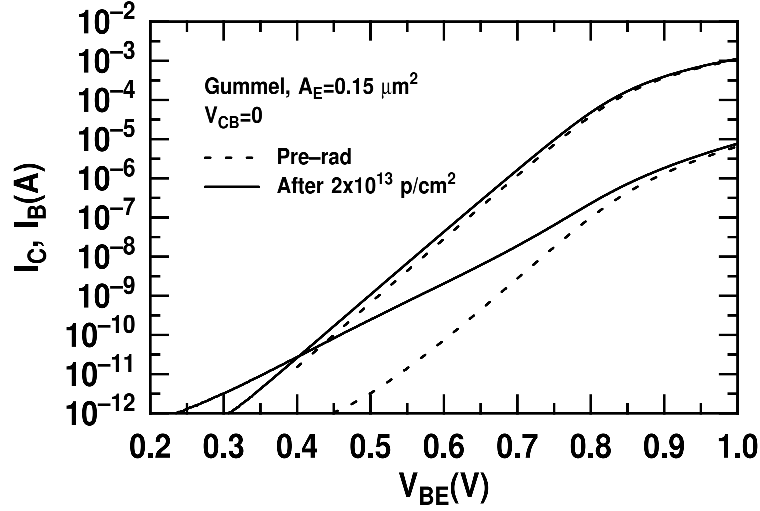

Figure 5.12: I_C and I_B versus V_{BE} for a small transistor before and after irradiation.

et al., 2001],

$$S_{I_{B,SCR}} = CJ_B n_{T,R} P_E \frac{\alpha_H}{f} \tag{5.4}$$

where C is a constant that is independent of bias and geometry, $n_{T,R}$ is the peripheral trap density induced by radiation, P_E is the emitter perimeter, α_H and is the Hooge constant. Thus, radiation-induced $S_{I_{B,SCR}}$ shows a J_B and P_E dependence. By analogy to the pre-radiation behavior, assuming each radiation-induced trap has a Lorentzian spectrum, the radiation-induced noise power spectral density $S_{I_{B,SCR}}$ can also be expressed as a superposition of Lorentzian spectra provided that the superposition shows a J_B and P_E dependence when the number of traps is large enough, as expected from equation (5.4). Hence, an empirical expression for $S_{I_{B,SCR}}$ can be obtained as,

$$S_{I_{B,SCR}} = \sum_{j=1}^{N_{T,R}} B \frac{J_B \tau_j}{1 + (2\pi f \tau_j)^2} \tag{5.5}$$

where τ_j is the j'th characteristic time constant associated with the j'th radiation-induced traps, B is a constant, $N_{T,R}$ and is the number of characteristic time constants associated with traps induced by radiation, which is assumed to be proportional to the emitter perimeter. The post-radiation spectrum can be obtained by adding equation (5.3) and

equation (5.5),

$$\begin{aligned} S_{I_{B,post}} &= S_{I_B} + S_{I_{B,SCR}} \\ &= \sum_{i=1}^{N} A \frac{A_E^{0.2} J_B^{2.4} \tau_i}{1 + (2\pi f \tau_i)^2} + \sum_{j=1}^{N_{T,R}} B \frac{J_B \tau_j}{1 + (2\pi f \tau_j)^2} \end{aligned} \tag{5.6}$$

Since S_{I_B} increases much faster than $S_{I_{B,SCR}}$ when J_B increases, S_{I_B} can be the dominant term at high bias in equation (5.6). It is thus possible to see that the noise variation shows a decrease at low J_B, rather than at high J_B for the same size devices, as shown in figure 5.7. For small devices with a small number of pre-radiation traps and a large noise variation, a few more radiation- induced traps can effectively decrease the noise variation at certain J_B. It is thus possible to see a relatively large decrease of noise variation for small devices compared to the medium and large devices.

To best fit the data, one characteristic time constant associated with radiation-induced traps was added to the small-sized device after irradiation, two were added to the medium-sized one, and five were added to the large-sized one ($B = 5.2 \times 10^{-18}$), consistent with a uniform trap generation rate at the device perimeter. The post-radiation calculation results are shown in figure 5.13, and are in agreement with the measured data. The calculated results of average post-radiation noise magnitude are also close to the data, but for brevity are not shown.

5.2.5 Summary

We have investigated for the first time the effects of proton irradiation on the low-frequency noise variation in aggressively scaled SiGe HBTs. The pre-radiation LFN variation is geometry dependent and largest for the smallest devices, but shows little dependence on bias. After irradiation, however, the overall noise magnitude shows little degradation, but the noise variation decreases significantly for the small devices, and shows both geometry and bias dependence.

The pre-radiation noise can be expressed as a superposition of individual GR traps, and the number of characteristic time constants associated with GR trap centers is proportional to the area of the transistors. The calculation shows a small number of pre radiation traps leads to a large noise variation. The radiation-induced noise is written as another set of superposed GR traps and added to the pre-radiation expression, and the number of characteristic time constants associated with radiation-induced GR traps is proportional to the emitter perimeter. Calculations show that such radiation-induced

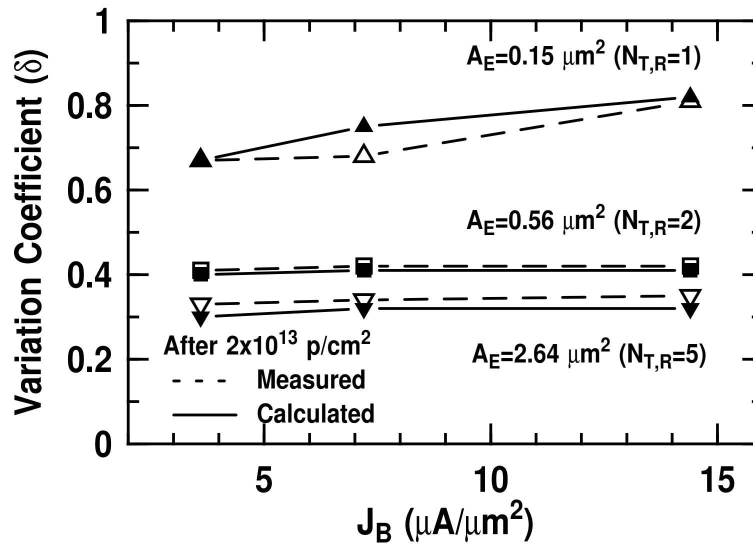

Figure 5.13: Noise variation from measured and calculated noise spectra versus J_B after irradiation. The number of additional radiation-induced traps $N_{T,R}$, was inferred to match the post-irradiation noise variation. $N_{T,R}$ used in calculations is indicated for each size.

traps can decrease the noise variation, consistent with the data.

Advanced device technologies with aggressively-scaled emitter geometries have a size-dependent low-frequency noise variation, and this variation is sensitive to proton irradiation. Proton irradiation can decrease the noise variation without any significant degradation in noise magnitude, and thus favors the application of scaled SiGe HBT technology in the radiation environment. This size variation is believed to be fundamental to scaled bipolar technologies and, thus, is of potential concern for noise-sensitive circuits operating in the radiation environment.

Acknowledgement

The authors would like to thank IBM Microelectronics, Essex Junction, VT, where the wafers were fabricated. The authors would also like to thank G. Niu, Y. Li, X. Liu, L. Cohn, B. Kauffman, D. Harame, D. Ahlgren, G. Freeman, B. Meyerson, D. Herman, and the IBM SiGe team for their contributions to this work.

5.3 Low-frequency Noise Variation in 200 and 350 GHz f_T SiGe HBT's

Abstract

The low-frequency noise in high-speed transistors generally increases (degrades) as device technologies down-scale for higher performance. Interestingly, the latest generation of deep-submicron SiGe HBTs breaks this trend, and we find record-low noise corner frequencies of 220 Hz in SiGe HBTs with a peak f_T of 210 GHz. An explanation for this behavior based on a reduction of the number of dominant noisy traps is offered, and microscopic 2-D simulations of noise are used to support this claim and explore the origins and scaling limits of low-frequency noise in advanced SiGe HBTs.

5.3.1 Introduction

Low-frequency noise (LFN) is up-converted to phase noise through the nonlinearities of transistors, placing a fundamental limit on the achievable spectral purity of communications systems. One unique merit of SiGe HBTs is that they can simultaneously provide very low broadband noise and $1/f$ noise, giving them a decided advantage over scaled CMOS and III-V devices for high-frequency wireless building blocks limited by phase noise (e.g., oscillators and mixers). A statistical (device-to-device) variation in the LFN spectra of small geometry SiGe HBTs was recently reported [Jin et al., 2003a]. The variation was found to be independent of bias current [Johansen et al., 2003b], and a qualitative explanation was offered which assumes a reduction in the number of noise-generating traps as the device emitter area decreases [Jin et al., 2003a; Sanden et al., 2002]. Here we present LFN results on SiGe HBTs with f_T's of 210 GHz and 350 GHz, compare scaling-induced small-size effects in LFN with previous SiGe HBT technology generations, and use 2-D simulations of $1/f$ noise to better understand the scaling limitations of noise in SiGe HBTs.

5.3.2 Experiment and Devices

The noise measurement setup has been previously described [Jin et al., 2003a]. Typically, 8-10 transistors were measured at each geometry to ensure statistical validity of the results. Deep- and shallow-trench isolated, UHV/CVD, graded-base SiGe HBTs with 210 GHz peak f_T [Freeman et al., 2003; Greenberg et al., 2002], and 350 GHz peak f_T

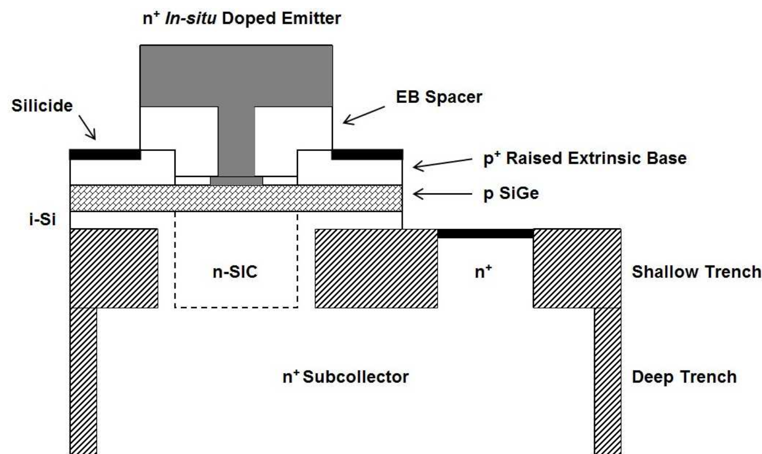

Figure 5.14: Schematic device cross-section showing the raised extrinsic base structure of the 210/350 GHz SiGe HBTs.

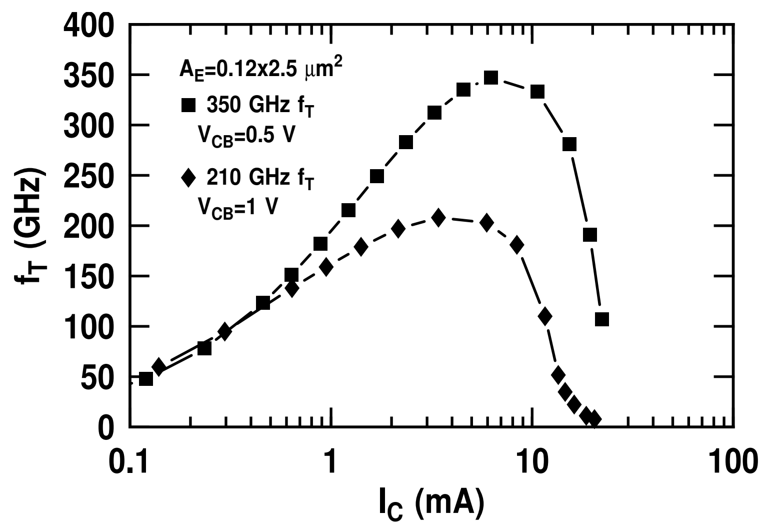

Figure 5.15: Unity gain cutoff frequency f_T, versus collector current for the 210 GHz and 350 GHz SiGe HBTs.

[Rieh et al., 2002] were investigated. Both technologies were fabricated in a novel, low-thermal-budget, raised extrinsic base structure using the same transistor layout. Careful vertical scaling of the collector and base profiles improved the performance from 210 GHz to 350 GHz. A schematic device cross-section and the frequency response for both devices are shown in figure 5.14 and figure 5.15.

5.3.3 Noise Measurement Results

In figure 5.16 we compare best-case noise spectra for several SiGe HBT generations. Clearly, SiGe HBTs are capable of extremely low levels of LFN. A record-low $1/f$ noise corner frequency of 220 Hz (I_B = 1 μA) in a 0.12×0.50 μm² SiGe HBT with a peak f_T of 210 GHz and NF_{min} of less than 0.5 dB at 10 GHz is achieved. Figure 5.17 shows

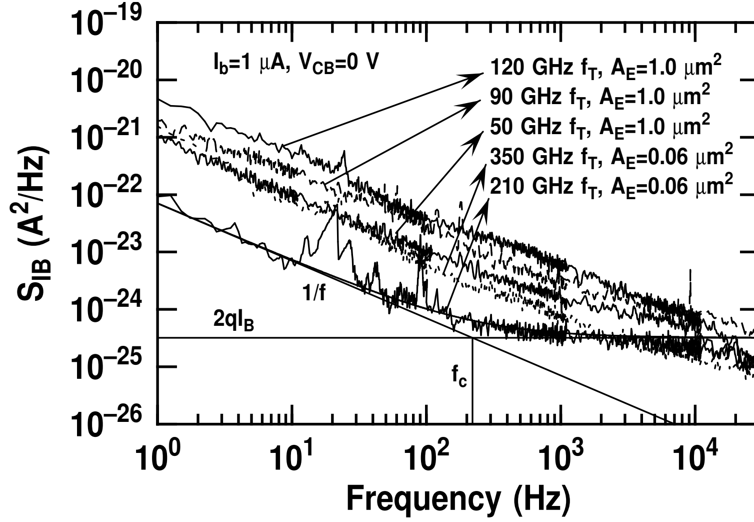

Figure 5.16: Best case noise spectra for several generations of SiGe HBTs.

the cross-generational noise magnitude as a function of bias current (at 10 Hz) for the devices exhibiting $1/f$ behavior, and a classical I_B^2 dependence is observed, which indicates that the noise mechanism is consistent with number fluctuation theory [Chen et al., 1998]. It has been recently reported that LFN in small-sized SiGe HBTs shows large device-to-device variations as the technology scales [Jin et al., 2003a], an issue of potential concern for both compact modeling and for certain circuit applications. The statistical noise variation between samples of the same geometry was quantified using a variation coefficient (δ), as defined by the standard deviation formula [Jin et al., 2003a; Sanden et al., 2002],

$$\delta = \frac{1}{S_{I_{B,avg}}} \sqrt{\frac{1}{N-1} \sum_{i=1}^{N} \left(S_{I_{B,i}} - S_{I_{B,avg}}\right)^2} \tag{5.7}$$

where $S_{I_{B,avg}} = N^{-1} \sum_{i=1}^{N} S_{I_{B,i}}$ is the average noise spectrum, i indicates the $i'th$ sample, and N is the total number of samples. Noise variation data is shown in figure 5.18

(the variation is negligible in the 50 GHz, first-generation devices), and explicit device-to-device statistical scatter for eight 0.12×0.5 μm^2 350 GHz and 210 GHz SiGe HBTs is shown in Figure 5.19. Interestingly, observe that the noise variation in the 210 GHz technology generation shows anomalous scaling behavior below about 0.2-0.3 μm^2 emitter geometry, below which the noise variation rapidly decreases.

5.3.4 Noise Model and Discussion

A physical model for $1/f$ noise in BJTs is based trapping/detrapping of carriers by noisy traps [Deen et al., 1998]. The resulting fluctuations in the number of carriers is thus the fundamental origin of $1/f$ noise. Each trap yields a Lorentzian spectrum, and the resulting noise spectrum is a superposition of Lorentzian spectra from individual traps,

$$S_{I_B}^{noisy} = \sum_{j}^{N_T} A \frac{J_B^2 \tau_j}{1 + (2\pi f \tau_j)^2} \tag{5.8}$$

where A is a constant, τ_j is the characteristic time constant of the jth independent trap and has to be distributed as $1/\tau$ to produce a $1/f$ spectrum [McWhorter, 1955b], and N_T is the total number of noisy traps in the device and proportional to A_E. When N_T is large, which is true for large devices, eq. (5.8) yields a $1/f$ spectrum. When N_T is small enough, corresponding to the small device case, the spectrum modeled by this equation

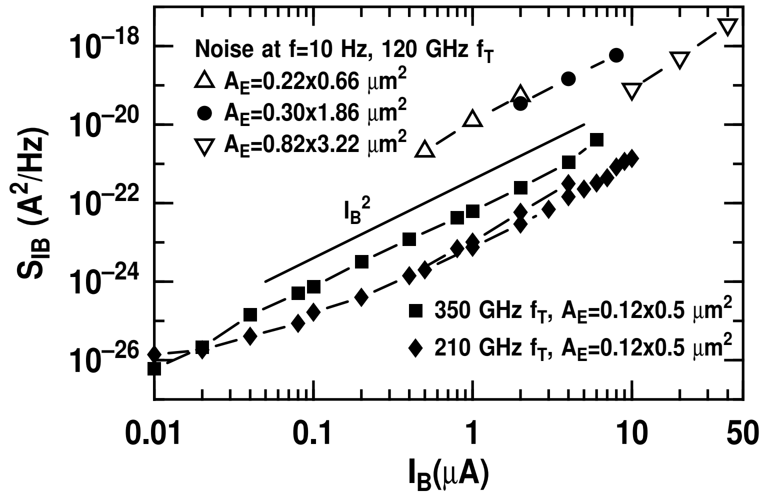

Figure 5.17: Noise power spectral density versus base current at 10 Hz for three generations of SiGe HBTs.

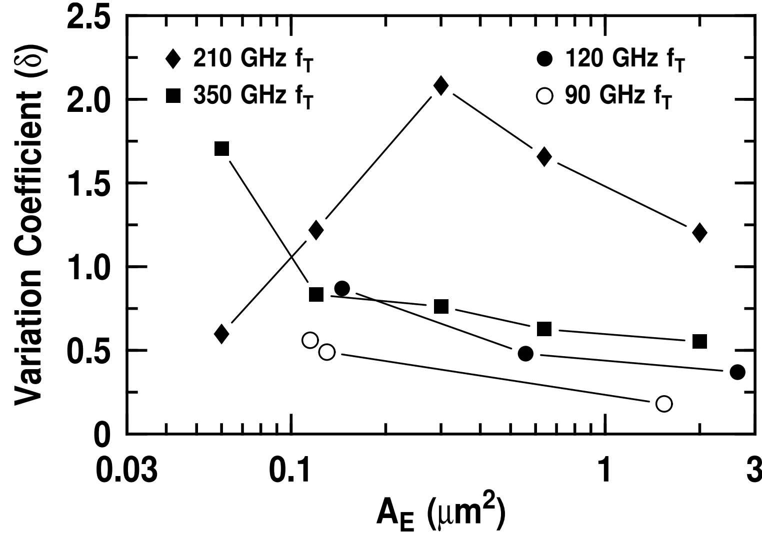

Figure 5.18: Noise variation versus emitter area for several generations of SiGe HBTs.

will show a deviation from $1/f$ behavior, and give device-to-device noise variations.

For the smallest devices, the number of noisy traps may be equal to zero, and eq. (5.8) then suggest zero resultant noise, which is clearly not physical. Adding a residual $1/f$ noise to the model gives,

$$S_{I_B} = S_{I_B}^{noisy} + S_{I_B}^{res} \tag{5.9}$$

where $S_{I_B}^{res}$ is the residual low-amplitude background $1/f$ noise that can be inferred from the smallest 210 GHz devices (Figure 5.16). The residual noise may be either of the mobility fluctuation type [Hooge and Vandamme, 1978], or of a number fluctuation type like $S_{I_B}^{noisy}$. If the latter is true, we can model $S_{I_B}^{res}$ by eq. (5.8), and the constant A has to be smaller for $S_{I_B}^{res}$ than for $S_{I_B}^{noisy}$, and the number of residual traps, N_T for $S_{I_B}^{res}$, has to be large enough to yield a $1/f$ background noise, as observed in figure 5.16. Measurements of the background noise for the smallest 210 GHz devices versus current (Figure 5.17), show a I_B^2 dependence. This suggests that the residual background $1/f$ noise is also of number fluctuation type [Chen et al., 1998].

5.3.5 Noise Simulations

Robust simulation of LFN has proven challenging to implement in commercial 2-D device simulators. Here, we present LFN simulations of SiGe HBTs using DESSIS [ISE, 2003], which we use to better understand the measured results. A Green's function ap-

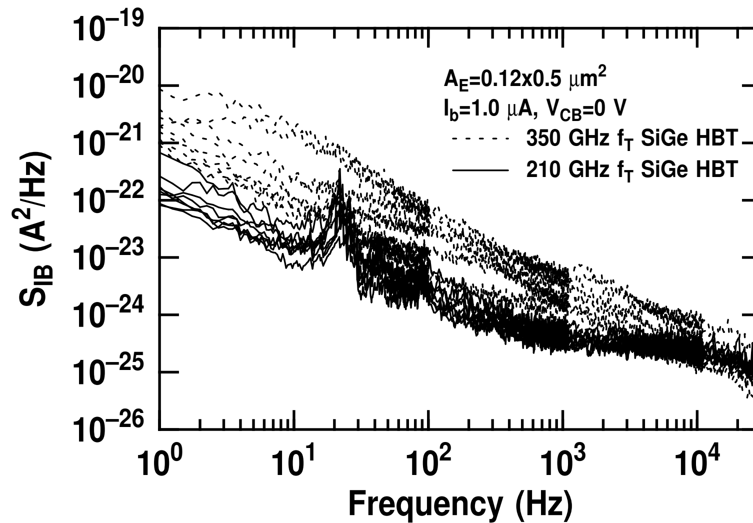

Figure 5.19: Base current noise showing the statistical variation sample-to-sample in 210/350 GHz devices.

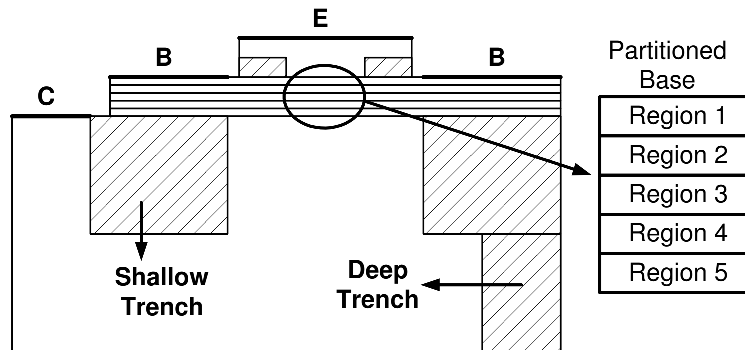

Figure 5.20: Device structure used in DESSIS simulations, showing the partitioning of the base that allows controlled location of different trap characteristics.

proach to the Langevin equation using Shockley's impedance field method is the basis for the noise implementation in DESSIS [Bonani et al., 1998]. In contrast to phenomenological simulations and other calculations of noise, the simulator in our case allows microscopic physical theory to be implemented in the device simulation, facilitating more physical insight. With careful mesh partitioning, different time constants having a $1/\tau$ distribution can be assigned to the traps responsible for noise generation in these SiGe HBTs, and used to shed light on the physical mechanism of the observed noise variations with scaling.

Figure 5.20 shows the simplified structure used in these DESSIS simulations. The

transistor base is partitioned into 5 regions, and different trap characteristics (time constant and trap density) are assigned to each region. Figure 5.21 demonstrates that the simulated base terminal current noise clearly qualitatively captures the measured statistical device-to-device noise variation we observe experimentally (figure 5.19). Furthermore, we can show with simulations that for devices so small that there are statistically no noisy traps remaining, the low-amplitude background $1/f$ noise is recovered (figure 5.21), consistent with the data shown in figure 5.16, and supporting the observation of the decreasing noise variation in the 210 GHz devices with decreasing emitter geometry. Using a slightly higher density of noisy traps in simulations and calculations explains why we cannot see the same trend for the 350 GHz devices in the selected range of emitter areas.

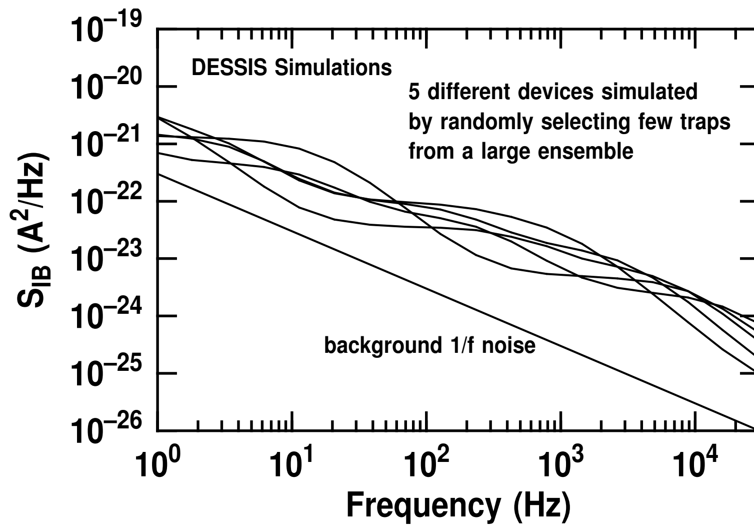

Figure 5.21: Base terminal current noise spectra extracted from DESSIS simulations showing small-size variations.

5.3.6 Summary

Aggressive down-scaling of transistor dimensions and profile optimization can result in impressive performance, but often at the cost of higher and variable LFN. In this work we find that the latest generation of SiGe HBTs (> 200 GHz) breaks this increasing LFN trend, and only a residual background noise remains, resulting in record values of noise corner frequency. Microscopic 2-D simulations of noise can reproduce the measured results and are used to explore the origin and scaling limits of low-frequency noise in

SiGe HBTs.

Acknowledgement

This work was supported by a Fulbright Fellowship (J. Johansen), the Semiconductor Research Corporation, IBM, and the Georgia Electronic Design Center at Georgia Tech. The wafers were fabricated at IBM Microelectronics, Essex Junction, VT.

Chapter 6

Voltage Time Series of Low-frequency Noise

In this chapter, we present recent statistical tools to characterize noise, and to probe for nonlinear coupling between frequency components in a noise signal. These tools have been applied to random telegraph signal (RTS) noise found in small geometry silicon-germanium (SiGe) Heterojunction Bipolar Transistors (HBTs). This chapter is based on three recently submitted conference papers. The first two of these papers focus on the statistical tools, and in the third paper these tools are applied to the analysis of low-frequency noise in SiGe HBTs.

- Y. Birkelund, J. A. Johansen, A. Hanssen, J. D. Cressler and A. D. van Rheenen. *Time series analysis of low-frequency noise in SiGe HBTs.* In *Proceedings of the Norwegian Signal Processing Symposium (NORSIG)*. Bergen, Norway, September 6-10, 2003b.
- Y. Birkelund, J. A. Johansen and A. Hanssen. *High-precision surrogate based tests for Gaussianity and linearity. Accepted for the European Signal Processing Conference (EUSIPCO)*, Vienna, Austria, September 6-10, 2004.
- J. A. Johansen, Y. Birkelund, Z. Jin and J. D. Cressler. *A statistical tool for probing the coupling between noisy traps in semiconductor devices, with application to* $1/f$ *noise in SiGe HBTs. Accepted for the Topical Meeting on Silicon Monolitic Integrated Circuits in RF Systems (SiRF)*, Atlanta, Georgia, September 8-12, 2004a.

The idea to use higher order statistics for analyzing possible coupling between frequency components in the low-frequency noise from electronic devices was brought up

during loose discussions with Yngve Birkelund. The idea materialized in late December 2003 in a Georgia Tech lab, and we decided to try and analyze voltage time series of noise from SiGe HBTs by higher order statistical methods. It would provide interesting real data for applications of this class of analysis methods, and it would give us new way to analyze low-frequency noise.

6.1 Statistical Tools for Analysis of Noise Time Series

Abstract

We have analyzed random telegraph signal noise in the base current of commercial SiGe HBTs. In a traditional noise analysis one often assumes that the noise processes are Gaussian, stationary, and/or linear. Using classical time series analysis, we show that the measured noise in these HBTs are non-Gaussian and non-linear. Exploratory time series analysis is applied to explore the origin of the low-frequency noise. We have decomposed the time series into a multilevel random telegraph signal (RTS) and remaining noise. The random telegraph signal is found to contribute with Lorentzian $1/f^2$-shaped spectra. Finally we show that the non-linearity found is directly connected to the random telegraph signal, which indicated that the GR-traps may be statistically dependent.

6.1.1 Introduction

To enhance device performance, geometrical downscaling is a key angle of attack. The resulting devices, however, can show variations in the low-frequency noise (LFN). Deviations from the classical $1/f$ shaped spectrum is found, as have been shown in the previous chapter of this thesis. Often such variations are due to generation-recombination (GR) traps with different characteristics in different devices. This can show up as RTS noise signatures in the time series of the noise, depending on the number of traps involved [Sanden and Deen, 2002]. In this chapter we analyze RTS noise time series from high performance commercial SiGe HBTs using various recent statistical tools.

Traditionally, the noise analysis is done by means of a spectrum analyzer. This approach quickly produces good spectral estimates, but restricts the possibility of applying more advanced signal analysis techniques. Time series of the noise record, on the other hand, provide unprocessed data that can be analyzed conventionally, but also facilitate more exploratory examination of the data. In the case of noise with RTS components, underlying trap characteristics have been extracted from the power spectrum [van Rheenen et al., 1985] [Vempati et al., 1996], or directly from the RTS time series [Kirton and Uren, 1989]. von Hartmann et al. [2002] have analyzed RTS noise from time series in SiGe HBTs as a function of bias and temperature and suggested two RTS noise sources. One in the base-emitter space charge region, and another in the silicon-silicon-dioxide (Si-SiO_2) interface at the emitter periphery. Here we shall not consider such

an analysis but explore the possibility to utilize advanced signal processing to analyze noise.

We have performed three different signal processing tasks: (i) Estimation of power spectrum by various methods, (ii) classification as Gaussian and/or linear (iii) analysis of non-linear coupling between frequencies. In the first task we have compared different power spectrum estimates using advanced approaches as the adaptive multitaper approach [Thomson, 1982; Birkelund et al., 2003a] and wavelet based methods [Daubechies, 1982; Gurley and Kareem, 1999]. This task also includes a comparison with the traditional analysis method using a HP3561A Dynamic Signal Analyzer. Application of time-frequency methods as wavelets, or dual-frequency methods as in [Hanssen and Scharf, 2003], also allows for investigation and quantification of non-stationary properties in time series.

The second task includes both conventional histogram analysis of the noise signal, and higher order spectra based Gaussian and linear classification methods [Rao and Gabr, 1980; Hinich, 1982]. With the recently proposed improvement to these classical method by means of surrogate data [Birkelund, 2003], the Gaussian and linear properties of the observed noise signals are analyzed and discussed.

In the last task we have decomposed the time series into a multilevel RTS and remaining noise. Then we use advanced statistical methods to probe for non-linear coupling between frequency components in the original noise signal, in the extracted RTS, and in the remaining noise. This allows us to check which component of the noise signal that contains a possible non-linear coupling between frequencies.

6.1.2 Devices and Measurements

A 0.18 μm SiGe HBT BiCMOS technology featuring 120-GHz f_T, 100-GHz f_{max} self-aligned SiGe HBT's was used in this investigation. Details of this technology can be found in [Joseph et al., 2001]. We have measured HBTs with three emitter areas: 0.256 μm^2 (small), 0.512 μm^2 (medium) and 1.28 μm^2 (large). Since the dominant noise source is associated with the base current, the base current noise was investigated. The HBT was biased in the common-emitter configuration as illustrated in figure 6.1 with $V_{CB} = 0$ V, and the external base resistance, R_B, was kept much higher than the input resistance of the HBT. Time series of the output voltage fluctuations on the collector terminal was measured using a low-noise voltage amplifier and a NI-6035E data acquisition card with 16 bit analog inputs, at sampling rate of 200 kHz. The input-referred base current noise was then obtained from the measured collector voltage fluctuations. A typical input

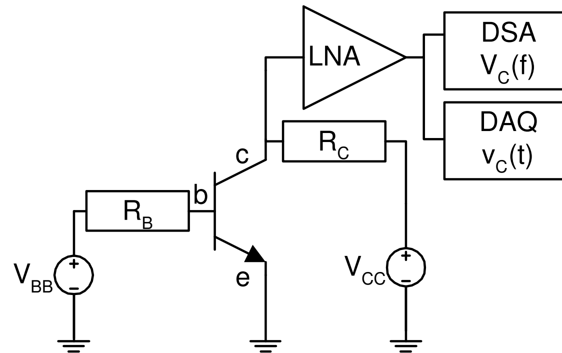

Figure 6.1: Schematic measurement setup for low-frequency noise with the HBT biased in the common emitter configuration. LNA is a low noise amplifier, DSA is a dynamic signal analyzer, DAQ is a data acquisition (sampling) device, b, c and e are the base, emitter and collector terminals of the HBT. V_{CC} and V_{BB} are adjustable battery power supplies.

referred current noise time series for the smallest HBT is shown in figure 6.2. From the full 30 second time series to the left it is difficult to identify the RTS noise. However, on the expanded timescale to the right, one can easily identify the RTS noise.

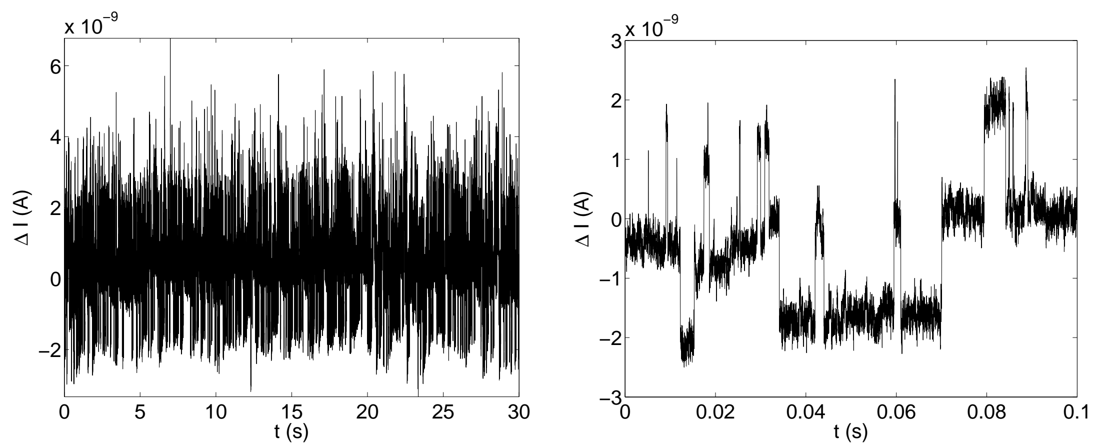

Figure 6.2: *Left*: Full length of the input referred base current noise time series from the smallest HBT (30 seconds sampled at 200 kHz). *Right*: The first 0.1 second of the time series clearly shows the RTS noise.

We have shown power spectrum estimates from HP 3561A in the left column of figure 6.3. These power spectra are similar to the ones obtained by Johansen et al. [2003b],

where the generation of $1/f$ noise is argued to be a superposition of Lorentzian spectra. In the middle and right column of figure 6.3, we have shown the first $T = 0.1$ seconds

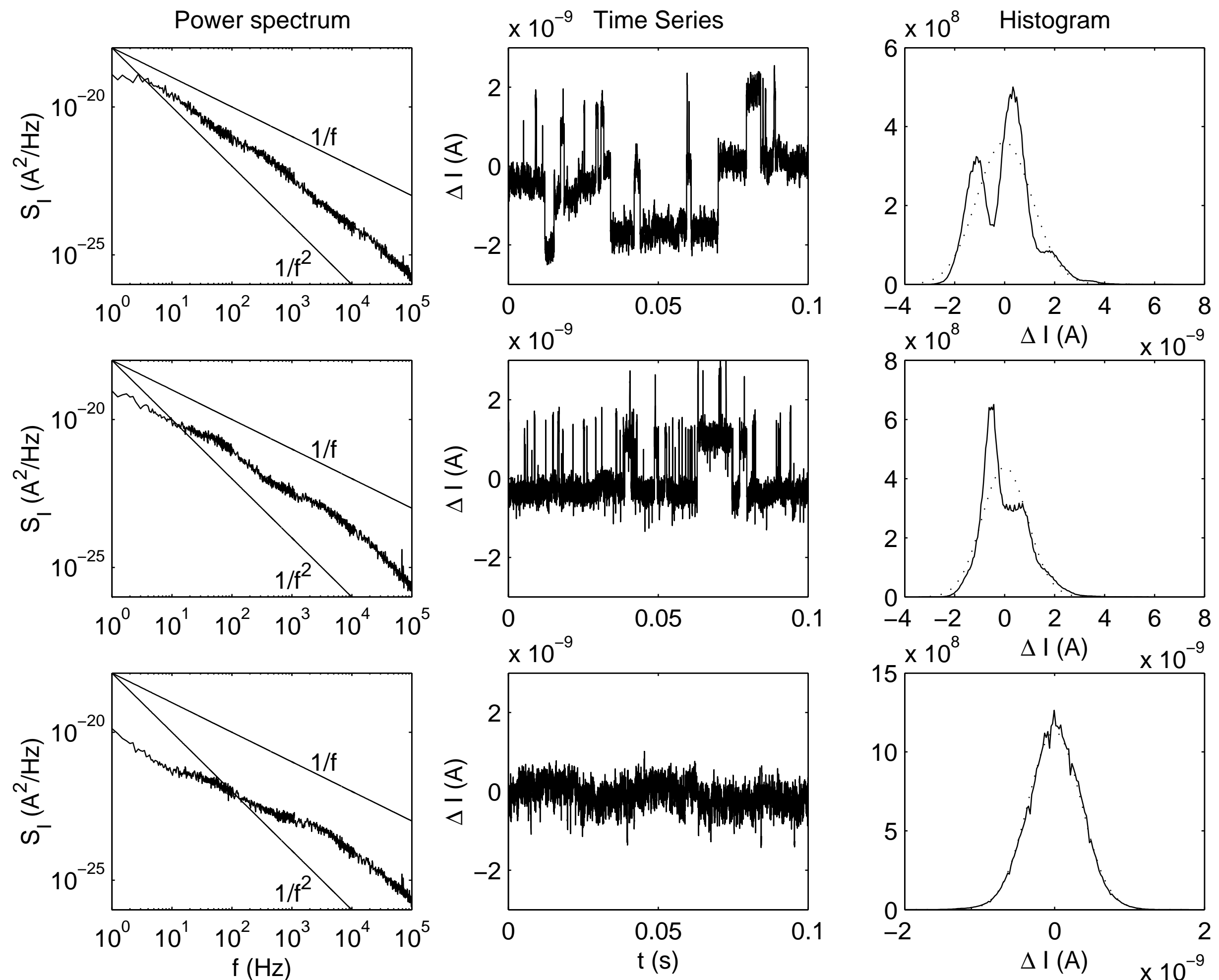

Figure 6.3: *Left column*: Power spectrum estimate from HP3561A Dynamic Signal Analyzer. The straight lines corresponds to theoretical $1/f$ and $1/f^2$ spectra. *Middle column*: First 0.1 second of the sampled time series. *Right column*: Estimated amplitude distribution (histogram) of the full sampled time series. The dotted line is the best Gaussian fit fo the data. Results from small, medium and large HBTs are shown in upper, middle and lower rows, respectively. Base current is 1 μA and $V_{CB} = 0$ V.

of the measured time series, and the corresponding amplitude distributions of the three different HBTs, respectively. The background noise seems to have comparable power in all devices, while the RTS amplitudes in the small and medium HBT are significantly larger than the background noise level. Hence, Lorentzian components dominate the

noise spectra. In the large device, the RTS is dominated by the background noise level in the time signal, but Lorentzian bumps can be seen in the power spectrum.

Since the smallest HBT exhibits the largest RTS amplitude, we shall in the following mainly focus on the smallest device.

6.1.3 Power Spectrum Estimation

A dynamic signal analyzer is normally used to obtain a power spectrum estimate over the frequency range from f=1 Hz to 100 kHz. In order to get the desired frequency resolution, we have to split the range into several smaller ranges, usually decades. For each frequency range the spectrum is obtained by averaging several spectral estimates from a number of time series captures [HP, 1985]. The full range spectrum is then obtained by combining the averaged estimate from each decade. In an experimental setting, overlap between the estimates from different ranges, is used as a quality measure for the obtained spectrum. A disadvantage of this approach is that different time series are used to obtain different parts of the spectrum. Hence, any coupling between higher and lower frequencies in the noise is not accessible. Therefore, we analyze single continuous measured time series by various methods. We will here compare the power spectrum estimate from the HP3561A Dynamic Signal Analyzer with power spectrum estimates using three different methods: The conventional periodogram using fast Fourier transform, the adaptive multitaper method, and a discrete wavelet spectrum. The variance of the estimates is used to compare their performance. In general, the variance is inversely proportional to the available degrees of freedom [Percival and Walden, 2000].

Conventional Periodogram Estimation

The averaged periodogram method, basically splits the time series into S segments of M data samples, where $N = SM$, and estimates the periodogram for each segment. This gives us power spectrum estimates at $M/2+1$ equidistant samples in $f \in [0, f_S/2]$. To improve the frequency resolution of the averaged periodogram for low frequencies, we can resample the time series with lower sampling frequency, and apply the same power spectrum method on this decimated time series. With a down sampling factor of R, the power spectrum is now estimated at $M/2+1$ linearly equally spaced samples in $f \in [0,\ f_S/2R]$, where f_S is the sampling frequency. We have presented the periodogram estimate of the smallest HBT in the upper right plot of figure 6.4. The results are obtained with $N = 6 \cdot 10^6$, $M = 128$ and $f_S = 200$ kHz, with decimation factors of

$R = 1, 10, 100, 1000$ and 10000, in which overlapping frequency samples are discarded. Compared to the HP3561A result, we find that the variance in the periodogram estimate is significantly lower in the higher frequency region. The decreasing variance as f increases in the averaged periodogram method is due to the increased number of segments available for small R, corresponding to a higher degree of freedom in the chi-square distribution of the power spectrum estimate [Percival and Walden, 1993]. For $R = 10000$, the total length of the decimated time series is $N = 600$, which only provides 4 segments to be averaged. The results from the HP3561A are obtained using a very similar procedure, but here the averaging always includes 25 segments in each frequency range (each R factor). Thus, the results from the HP3561A have lower variance than the periodogram based method at $R = 10000$. To match this variance, we would have to measure the time series for $T = 25MR/f_S = 160$ seconds. This is comparable to the time used by the HP3561A at the lowest frequency range.

The Adaptive Multitaper Method

The variance of the periodogram based method can be further reduced by frequency smoothing. One advanced frequency smoothing technique is to apply the adaptive multitaper method [Thomson, 1982; Birkelund et al., 2003a]. The user defined time-frequency half-bandwidth Mf_B basically controls the number of frequency samples to smooth over, so that the power spectrum estimate variance is reduced by a factor $2Mf_B$ compared to the periodogram method. In addition to this reduced variance, the adaptive multitaper method minimizes the possibility of spectral leakage.

With $Mf_B = 2$, and the same M and R settings as for the periodogram, we have shown the power spectrum estimate using the adaptive multitaper method in the lower left plot of figure 6.4. For the lowest frequencies, the multitaper method provides estimates with similar or much better variance properties than the HP3561A method in all frequency ranges. The multitaper result is almost identical to the periodogram based result for $f > 10$ Hz, which indicates that spectral leakage does not influence the periodogram based method for these particular time series.

Discrete Wavelet Basis

The most common way to display low-frequency power spectra, is to use logarithmic scaling on both the power- and frequency axis. Wavelets provide a decomposition of the time series in time and scale, instead of time and frequency as in the Fourier based

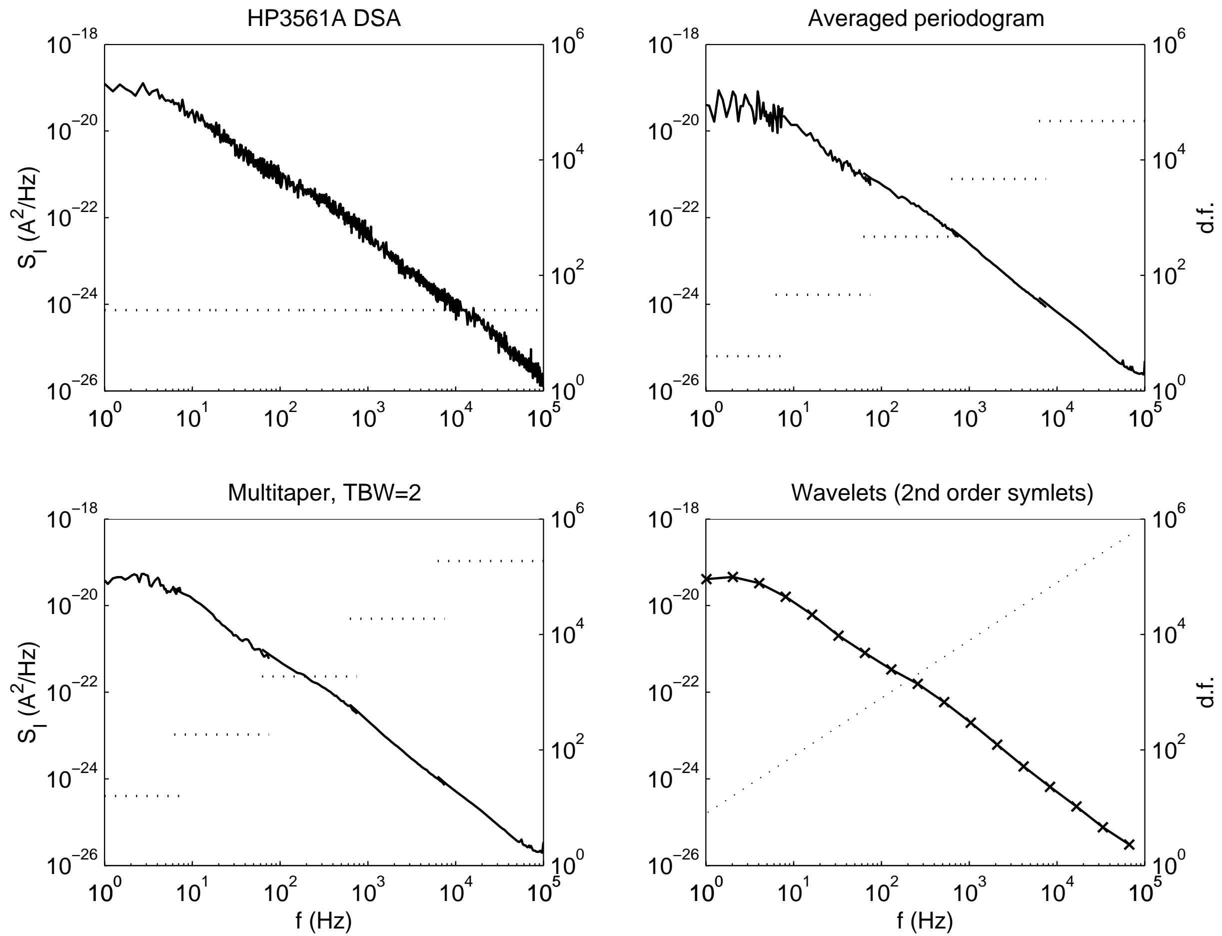

Figure 6.4: Power spectrum estimates from the small HBT biased at $I_B = 1$ μA and $V_{CB} = 0$ V. Power spectral density is shown as solid lines on left y-axis, and corresponding degrees of freedom is shown as dotted lines on right y-axis of each plot. *Upper left*: HP 3561A estimate. *Upper right*: Averaged periodogram. *Lower left*: Multitaper. *Lower right*: Wavelets (2nd order symlet).

method [Daubechies, 1982; Gurley and Kareem, 1999; Percival and Walden, 2000]. Discrete wavelets generally work on scales of length $s = 2^p$, where $p = 1, 2, 3, \ldots, P$ and $s^P < N$. The scale parameter is connected to the traditional frequency approach through a pseudo-frequency $f' \propto 1/s$, which leads to P logarithmically spaced frequency samples for $f' \in [f_{min}, f_{max}]$. The exact boundary frequencies, f_{min} and f_{max} depends on the chosen wavelet function.

Using the first $T = 0.1$ second of the time series of the small HBT, we have shown its wavelet decomposition using the discrete symlet wavelet of second order [Daubechies,

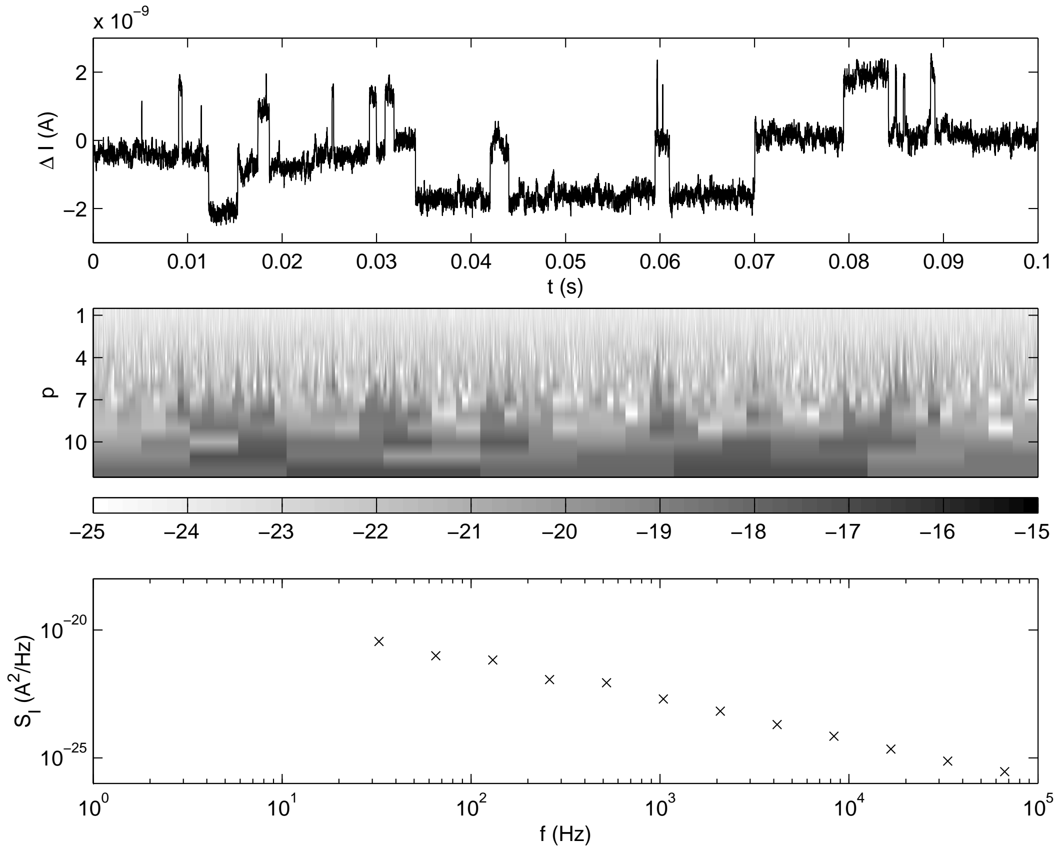

Figure 6.5: Results from the small device biased at $I_B = 1$ μA and $V_{CB} = 0$ V. *Upper plot*: Time series of input referred base current noise. *Middle plot*: Wavelet scalogram (logarithmic amplitude as shades of gray), with scale on the y-axis, and time along the x-axis. *Lower plot*: Wavelet power spectrum estimate.

1982], in the upper and middle plot of figure 6.5, respectively. The combination of time and scale information can easily be identified by the peaks located at $t \simeq 0.06$ s in the time series. The wavelet coefficients, or the scalogram,contain information of both the length of these peaks (from the scale s^p) and the exact time of the different peaks. This time-scale information can be used to analyze non-stationary time series. We have averaged the scaleogram along the time axis to create a power spectrum estimate at the logarithmically spaced frequencies [Gurley and Kareem, 1999; Percival and Walden, 2000], as shown in the lower plot of figure 6.5.

We have compared the wavelet based power spectrum estimate with the other estimates in the lower right plot of figure 6.4. The magnitude of the power spectrum is virtually identical to the other methods, but the rigid logarithmic frequency resolution

provides an objective grid to analyze the shape for all frequency regions. As for the Fourier based methods, the wavelet based method clearly provides lower variance for increasing frequencies.

The effective bandwidth in the wavelet method increases from one frequency sample to the next. Thus, the wavelet power spectrum can be described as a logarithmic frequency smoother, with a variable bandwidth for each scale or frequency. The wavelet power spectrum provide the lowest variance among the methods in figure 6.4. The variance is decreasing for each point towards higher frequencies in the spectrum, as opposed to the stepwise variance for the other methods. However, a more rigorous statistical analysis is needed to fully describe all the statistical properties of the methods applied in this thesis.

6.1.4 Gaussianity and Linearity

Non-Gaussianity and non-linearity in time series represent significant challenges in time series analysis [Theiler et al., 1992]. Theoretically, the Gaussian distribution is generally much easier to handle than most non-Gaussian distributions. Oftenm the Gaussian assumption leads to closed form mean squared optimal solution. For non-Gaussian time series, the solution of the same problem may lead to sub-optimal or unstable solutions. In particular, applications based on a Gaussian assumption may lead to erroneous results if the time series in study deviate significantly from a Gaussian or linear process.

Histogram Analysis

The right hand column of figure 6.3 shows a normalized histogram estimate of the probability density function for the small, medium and large HBTs as solid lines in the upper, middle and lower row, respectively. The dotted line represents a Gaussian distribution with a mean and variance identical to the HBT time series. We find that the two smallest HBTs shows significant deviation from the theoretical Gaussian distribution. These results indicate that these time series are non-Gaussian. The peaks in the normalized histograms correspond to the different charge levels seen in the time series in figure 6.3. From the time series in figure 6.3, we can also conclude that the estimated density function does not come from a sum of Gaussian distribution with different means. More likely, the time series consists of a sum of one Gaussian process and a RTS with several different discrete levels. For the largest HBT, however, the estimated and theoretical

Gaussian distribution are in good agreement.

Higher Order Spectrum Based Test

The power spectral density, or the power spectrum, is an indispensable quantity when describing the second-order statistics of stationary stochastic processes. If the process considered has a Gaussian amplitude distribution, it is well known that the mean value and the power spectrum characterize the process completely. If the process under study is non-Gaussian, or if it is the result of nonlinear dynamics, knowledge of the mean value and the power spectrum is not sufficient to fully characterize the process. Under such circumstances, one may have to consider higher order spectra (HOS). HOS based tests for Gaussianity and linearity of stationary processes are most often based on the complex valued skewness function [Brillinger, 1965],

$$b(f_1, f_2) = \frac{B(f_1, f_2)}{\sqrt{S(f_1)S(f_2)S(f_1 + f_2)}}, \tag{6.1}$$

where $S(f)$ and $B(f_1, f_2)$ are the power- and bispectrum of the time series, respectively. Note that $b(f_1, f_2)$ has been referred to as *bicoherence* or *normalized bispectrum* in the literature, although $b(f_1, f_2)$ is not limited to values below unity [Birkelund, 2003].

Theoretically, a Gaussian process has a zero valued skewness function, a linear non-Gaussian time series has a non-zero constant magnitude skewness function, and a nonlinear time series has a frequency dependent skewness function [Brillinger, 1965]. Rao and Gabr [1980] proposed hypothesis tests for both Gaussianity and linearity, and Hinich [1982] constructed asymptotic tests that are well established in time series analysis of economic data [Barnett et al., 1997]. In [Birkelund, 2003], an improved version of these tests are based on the use of surrogate time series [Theiler et al., 1992]. These surrogates time series are generated to fulfill the two different null hypothesis of the tests, a linear Gaussian and non-Gaussian time series, respectively, while the dynamical properties are identical to the original time series. That is, the power spectrum of the original and surrogate time series are almost identical, as is their mean, variance and skewness. In the Gaussianity test we simply test if the magnitude of the skewness function estimate of the original time series is significantly larger than for its Gaussian distributed surrogates (RPH) [Theiler et al., 1992]. Similarly, the linearity test checks if the bifrequency variation of $|b(f1, f2)|$ for LFNG surrogates are smaller than the original time series [Birkelund et al., 2004]. Using a significance level of $1 - \alpha = 0.99$, we have performed the Gaussian and linear classification method on the $R = 100$ decimated time series of

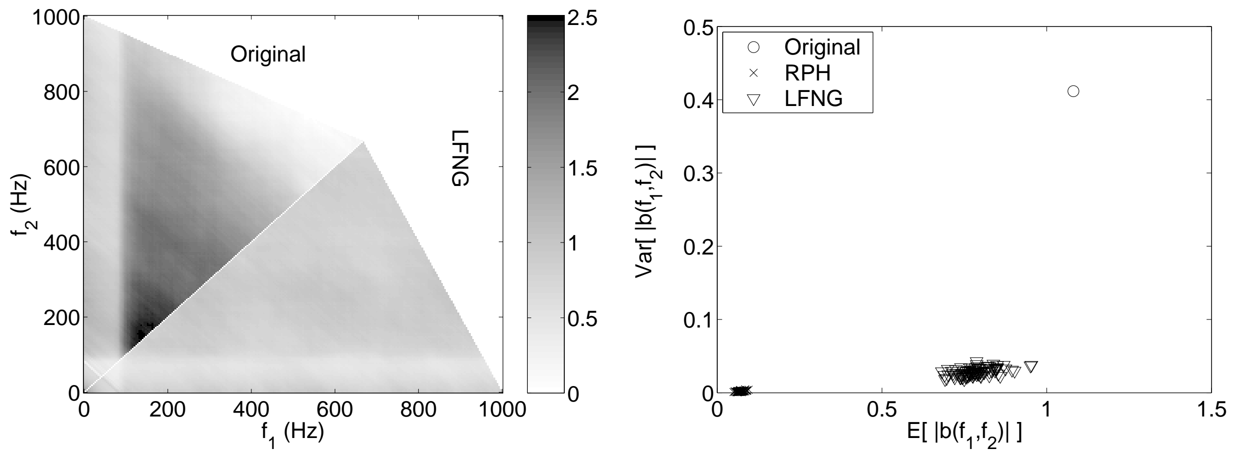

Figure 6.6: *Left*: Skewness function estimates for the original signal in the left triangular, and for LFNG surrogate data in the lower triangular. *Right*: Classification statistics, i.e, mean and variance of the estimated skewness function, for the original signal and RPH, and LFNG surrogate data. $\circ$ is the original signal, $\times$ is the RPH surrogate data, and $\triangledown$ is the LFNG surrogate data.

the small HBT. With $\alpha = 0.01$, the number of RPH and LFNG surrogates for each test is $1/\alpha - 1 = 99$. If the Gaussian and linear discrimination statistic are larger than all the RPH and LFNG statistics, respectively, the time series are classified as Gaussian and linear with α significance level.

This skewness function estimate is found using frequency smoothed HOS estimates, as explained by Birkelund et al. [2004]. The left part of figure 6.6 shows the skewness function estimate of original noise data, and LFNG surrogate data. We focus on frequencies below 1 kHz because the two main *bumps* in the spectrum are contained in this frequency range. The surrogate data skewness function has a nearly constant amplitude, while the real data skewness function is non-constant and has a peak below 200 Hz. This is indicative of non-linear coupling between pairs of frequencies in the noise signal. Hence, this suggests that the traps causing the RTS noise are statistically dependent rather than independent.

The right plot of figure 6.6 shows the Gaussian and linear detection statistics of the original, RPH, and LFNG surrogate data. The strong separation between the original and RPH insample mean on the x-axis, indicates that the signal under study is non-Gaussian. Similarly, the separation between the original signal and the LFNG insample variance along the y-axis, strongly indicates that the signal is non-linear.

6.1.5 Decomposition of Time Series

In this section we shall decompose the time series into a multilevel RTS and remaining noise. This is based on the assumption that the mechanisms generating the RTS and the remaining $1/f$ noise are independent [Vempati et al., 1996; Wu et al., 1989].

A decomposition of the time series into a multilevel RTS and residual noise is now performed using these steps: (1) Detect all possible RTS steps. This is done by calculating the local mean over L samples, and comparing this to the original signal. If the difference is greater than a significance level ΔL, we detect this a possible change of mean value. (2) Calculate the mean value between each instance of the change. If the magnitude of the difference in mean is greater than a significance level ΔD, we use this difference as the jump height in the RTS component. (3) Since we expect that an increase in the mean is followed by the same decrease at a later moment, we also keep track of the Q previous mean values. If the distance between previous mean values and the new is less than ΔQ, the closest pervious mean value is used at the level of the RTS signal. In practice, L restricts the length of possible rectangular pulses to be detected, ΔL is used to tune the filtering to not detect regular noise as jumps (which would significantly increase the calculation time in this iterative filtering), while ΔD restricts the possible height of each change. The ΔQ parameters adjust the number of possible levels locally in time, while Q allows the levels to change over time to keep track of low frequency variations.

Naturally, this filtering technique works well when the different levels in the RTS are significantly higher than the residual noise, but the parameters have to be carefully tuned to the time series in study. Thus, we have only performed the decomposition on the smallest HBT where the levels seems to have the highest separations. The time series of the small HBT, and its decomposition into RTS and remaining noise, are shown to the left in the upper, middle and lower rows of figure 6.7, respectively.

In the middle column of figure 6.7, we have shown the wavelet based power spectrum estimate of the original time series and its decomposition. From these plots, we find that the RTS signal contributes with two frequency separated Lorentzian $1/f^2$ shaped spectra, one at very low frequency and the other near $f = 200$ Hz. From figure 6.3 and figure 6.7, we understand that the small HBT time series can be decomposed into non-Gaussian RTS components with two separated $1/f^2$ shaped features in the power spectrum, and a component closer to $1/f$-shaped noise with Gaussian distribution.

To further examine the origin of the non-linear properties in the HBT time series, we

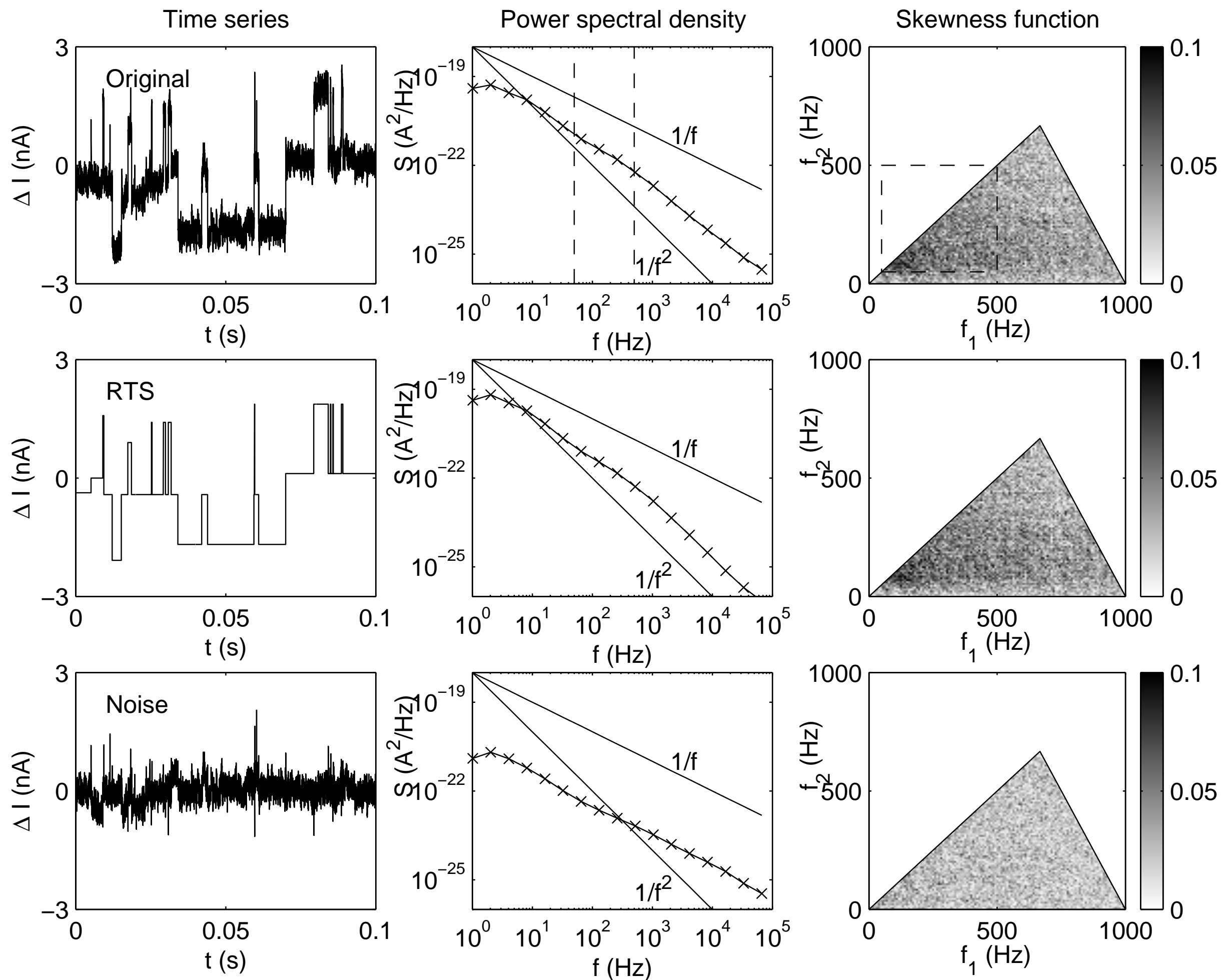

Figure 6.7: Decomposition results of the small HBT biased at $I_B = 1$ μA and $V_{CB} = 0$ V. *Left*: Time series. Middle: Wavelet power spectrum estimates. *Right*: Skewness/bichoerence estimate. Original time series, RTS component and remaining noise is shown in upper, middle and lower rows, respectively.

have shown the magnitude of the estimated skewness functions to the right in figure 6.7. The upper right plot shows the results for the original time series, the middle right show the results for the extracted RTS, and the lower right shows the results of the residual noise. Since the frequency dependent skewness magnitude of the original time series is almost identical to the RTS results, this indicates that the non-linearity is generated by the multilevel RTS in the original signal. In the residual noise, we find no indications of non-linear coupling. This indicates that the GR traps generating the RTS are coupled, and not independent instances as in the traditional RTS model.

6.1.6 Conclusion

It is generally accepted that the low-frequency noise of bipolar transistors are caused by number fluctuations [Chen et al., 1998]. These fluctuations can be caused by trapping/de-trapping or generation-recombination [Kirton and Uren, 1989] that randomly modifies the number of carriers contributing to the charge transport in the device. Each trap is characterized by a time constant and has a Lorentzian spectrum. If the traps are independent and have a certain distribution of time constants, a superposition of the traps yields a $1/f$ spectrum.

For small devices with a small number of traps the signature of single traps can often be observed as RTS signatures in the time series [Deen and Simoen, 2001]. The RTS signature is dominant for the small and medium size devices. The signal analysis is performed on the small device because it has the highest amplitude multilevel RTS signature. The multilevel RTS indicates that more than one trap is present. The estimation of the skewness function is an attempt to clarify if the traps are dependent. The skewness function quantifies the degree of nonlinear coupling between different frequency components in the signal, and hence potentially serves as a tool to reveal non-linear coupling between traps. The skewness function magnitude for the original noise signal has a maximum around 100-200 Hz. This indicates that traps with time constants in this range are dependent.

The different signal processing tools applied in this chapter are advanced and non-standard. Based on the result from the presented time series, and similar results from other HBTs, we have two recommendations of time series analysis for low-frequency noise research.

First, the traditional power spectral estimation method by HP3561A Dynamic Signal Analyzer produces results very similar to our advanced time series methods. The choice of method in this case is thus reduced to a practical question of analyzing equipment. Since the use of HP3561A and similar hardware based analyzing tools are well known in the electron devices communities, we do not recommend the use of advanced time series analysis for power spectrum estimation purposes alone.

Second, the time series analysis approach does allow for several other analysis methods. Using advanced signal processing techniques we have shown that the measured RTS noise is non-Gaussian and non-linear, and the these properties are tied to the RTS part of the noise. The indications of non-linearly coupled GR-traps in our results can be used to improve the existing models for such processes.

Chapter 7

Summary and Conclusions

In this thesis, we describe results from low-frequency electrical noise experiments on semiconductor devices. We focused on devices utilizing the silicon-germanium alloy. We studied noise in silicon-germanium thin film resistors, in silicon based MOSFETs with silicon-germanium gates, in AlGaInP quantum well lasers, and in silicon-germanium Heterojunction Bipolar Transistors. In the following we summarize the main conclusions drawn in this thesis, before we suggest relevant future work.

In chapter 2 we compared the low-frequency noise from poly-crystalline thin film resistors with different germanium content and film thickness. Germanium content and film thickness was shown to have little influence on the noise level. The noise level decreases with increasing doping level. The noise was found to stem from mobility fluctuations in the depletion region of the grains.

In chapter 3 we compared the low-frequency noise of silicon based field-effect transistors with poly-crystalline gates, made from silicon and silicon-germanium. The output noise level for N-MOSFETs was independent of the gate-material, whereas for P-MOSFETs the SiGe gate material resulted in lower noise. Analysis of fluctuating physical quantities, points towards mobility fluctuations for P-MOS, and number fluctuations for N-MOS.

In chapter 4 we presented results from measurement of the low-frequency electrical noise in AlGaInP Quantum Well Lasers. Experimental evidence of the association between LFN and device reliability was presented. LFN measurements can reveal the damage created by even a short burn-in process not found in $I_D - V$ and $P_O - I_D$ dependencies. Hence, the $1/f$ noise measurement can be used as a non-destructive diagnostic tool for assessing the reliability of laser diodes.

In chapter 5 we explored the low-frequency noise in state-of-the-art silicon-germanium

Heterojunction Bipolar Transistors. We found that downscaling induces a device-to-device noise variation. The variation is believed to be caused by a small, random set of GR traps, that is different for each device, distributed over the emitter area. The variation is strongly dependent on geometry, but little dependence on bias was found.

We intentionally induced additional traps by means of proton irradiation. This causes a reduction in the noise variation, especially for the smallest devices. These traps, distributed over the emitter perimeter, are found to contribute a noise with a different bias dependence than the pre-irradiation traps. Calculations show that such radiation-induced traps can decrease the noise variation, consistent with measurements. We use these calculations to quantify the number of dominant noise generating traps, before and after irradiation.

Aggressive down-scaling is known to result in higher and more variable LFN. However, we found that the latest generation of SiGe HBTs ($>$ 200 GHz) breaks this increasing LFN trend, and only a residual background noise remains, resulting in record values of noise corner frequency.

In chapter 6 we presented recent statistical tools to probe for nonlinear coupling between frequency components in a noise signal. These tools were applied to low-frequency noise time series with RTS noise, found in small geometry SiGe HBTs. We decomposed the signal into a pure multilevel RTS and remaining noise, and found that the non-linearity and non-Gaussianity in the original signal, is tied to the RTS noise component, which is indicative of non-linear coupling between the frequencies from the GR traps generating RTS noise.

Suggestions for Future Work

Further experiments should be carried out in order to reveal the intrinsic origin of the record low-noise level found in the latest generation of SiGe HBTs. Microscopic simulations of low-frequency noise is encouraged. It is a valuable tool in trying to understand what physical quantities can cause the observed low-frequency noise. Device simulator noise implementations that allow single noise sources to be localized at specific positions inside device models, would provide an excellent framework for understanding the noise and noise variation observed in highly scaled devices.

The use of advanced signal processing tools for analysis of low-frequency noise should be further explored. The skewness function approach from chapter 6, should be used to compare measured noise results, with those of existing models for noise. In particular, it could be used to analyze the noise from two devices with similar Lorentzian spectral signatures, where one device has a RTS signature, and the other does not.

Bibliography

D. C. Ahlgren, M. Gilbert, D. Greenberg, J. Jeng, J. Malinowski, D. Nguyen-Ngoc, K. Schonenberg, K. Stein, R. Groves, K. Walter, G. Hueckel, D. Colavito, G. Freeman, D. Sunderland, D. L. Harame and B. Meyerson. *Manufacturability demonstration of an integrated SiGe HBT technology for the analog and wireless marketplace*. In *IEEE International Electron Devices Meeting Technical Digest (IEDM)*, pp. 859–862. San Francisco, CA, USA, December 8–11, 1996.

P. A. Andrekson, P. Andersson, A. Alping and S. T. Eng. *In situ characterization of laser diodes from wide-band electrical noise measurement*. *IEEE Journal of Lightwave Technology*, **4**(7): 804–812, 1986.

ASTM Standard F1096. *Standard method for measuring MOSFET saturated threshold voltage*. In *1996 Annual Book of ASTM Standards*. American Society for Testing and Materials, Conshohocken, PA, USA, 1996.

A. Balandin, ed. *Noise and Fluctuations Control in Electronic Devices*. American Scientific Publishers, 2002.

J. Bardeen and W. H. Brattain. *The transistor, a semiconductor triode*. *Physical Review*, **74**: 230, 1948.

W. A. Barnett, A. R. Gallant, M. J. Hinich, J. A. Jungeilges, D. T. Kaplan and M. J. Jensen. *A single-blind controlled competition among tests for nonlinearity and chaos*. *Journal of Economics*, **82**: 57–192, 1997.

J. Bernamont. *Annalen der Physik*, **7**: 71, 1937.

Y. Birkelund. *Statistical signal processing with higher order spectra: Non-linear signal and system analysis*. Ph.D. thesis, University of Tromsø, Tromsø, Norway, 2003.

Y. Birkelund, A. Hanssen and E. Powers. *Multitaper estimators of polyspectra*. *Signal Processing*, **83**: 545–559, 2003a.

Y. Birkelund, J. A. Johansen, A. Hanssen, J. D. Cressler and A. D. van Rheenen. *Time series analysis of low-frequency noise in SiGe HBTs*. In *Proceedings of the Norwegian Signal Processing Symposium (NORSIG)*. Bergen, Norway, September 6-10, 2003b.

Y. Birkelund, J. A. Johansen and A. Hanssen. *High-precision surrogate based tests for Gaussianity and linearity*. *Accepted for the European Signal Processing Conference (EUSIPCO)*, Vienna, Austria, September 6-10, 2004.

F. Bonani, G. Ghione, M. R. Pinto and R. K. Smith. *An efficient approach to noise analysis through multidimensional physics-based models*. *IEEE Transactions on Electron Devices*, **45**: 261–269, 1998.

D. R. Brillinger. *An introduction to polyspectra*. *The Annals of Mathematical Statistics*, **36**: 1351–1374, 1965.

J. Brini. *Low frequency noise spectroscopy in MOS and bipolar devices*. *Microelectronics Engineering*, **40**: 167–179, 1998.

J. Chang, A. A. Abidi and C. R. Viswanathan. *Flicker noise in CMOS transistors from subthreshold to strong inversion at various temperatures*. *IEEE Transactions on Electron Devices*, **41**(11): 1965–1971, 1994.

X. Y. Chen. *Lattice scattering and $1/f$ noise in semiconductors*. Ph.D. thesis, Technische Universität Eindhoven, Eindhoven, The Netherlands, April 1997.

X. Y. Chen and L. C. deFolter. *Annealing of proton-damaged GaAs and $1/f$ noise*. *Semiconductor Science and Technology*, **12**(10): 1195–1201, 1997.

X. Y. Chen, M. J. Deen, Z. X. Yan and M. Schroter. *Effects of emitter dimensions on low-frequency noise in double-polysilicon BJTs*. *IEE Electronics Letters*, **34**: 219–220, 1998.

X. Y. Chen, C. Salm, F. N. Hooge and P. H. Woerlee. *$1/f$ noise in polycrystalline SiGe analyzed in terms of mobility fluctuations*. *Solid-State Electronics*, **43**(9): 1715–1724, 1999.

X. Y. Chen, M. J. Deen and C. X. Peng. *Low-frequency electrical noise of high-speed, high-performance 1.3 μm strained multiquantum well gain-coupled distributed feedback lasers*. *Journal of Applied Physics*, **88**(11): 746–6751, 2000a.

X. Y. Chen, J. A. Johansen, C. Salm and A. D. van Rheenen. *On low-frequency noise of polycrystalline Ge_xSi_{1-x} for sub-micron CMOS technologies*. In *Proceeding of the International Conference on Communications, Computers & Devices (ICCCD)*, edited by S. L. Maskara and T. S. Lamba, volume I, pp. 187–190. Kharagpur, India, December 14-16, 2000b.

X. Y. Chen, J. A. Johansen and C. L. Liu. *Temperature dependence of low frequency electrical noise and reliability of semiconductor lasers*. In *Proceedings of SPIE, Semiconductor Optoelectronic Device Manufacturing and Applications*, edited by D. Chen, R. T. Chen, G.-Y. Wang and C.-C. Zhu, volume 4602, pp. 128–133. Nanjing, China, November 7–9, 2001a.

X. Y. Chen, J. A. Johansen, C. Salm and A. D. van Rheenen. *On low-frequency noise of polycrystalline Ge_xSi_{1-x} for sub-micron CMOS technologies*. *Solid-State Electronics*, **45**(11): 1967–1971, 2001b.

K. D. Chik and T. F. Devenyi. *The effects of screening on the reliability of GaAlAs/GaAs semiconductor lasers*. *IEEE Transactions on Electron Devices*, **35**(7): 966–969, 1988.

J. D. Cressler and G. Niu. *Silicon-Germanium Heterojunction Bipolar Transistors*. Artech House, 2003.

J. D. Cressler, R. Krithivasan, G. Zhang, G. Niu, P. W. Marshall, H. S. Kim, R. A. Reed, M. J. Palmer and A. J. Joseph. *An investigation of the origins of the variable proton tolerance in multiple SiGe HBT BiCMOS technology generations*. *IEEE Transactions on Nuclear Science*, **49**: 3203–3207, 2002.

I. Daubechies. *Ten lectures on wavelets*. Society for Industrial and Applied Mathematics, Philadelphia, PA, 1982.

M. Deen and E. Simoen. *Low-frequency noise in polysilicon-emitter bipolar transistors*. *IEE Proceedings Circuits, Devices & Systems*, **149**(1): 40–50, 2001.

M. J. Deen, L. Ilowski and P. Yang. *Low-frequency noise in polysilicon emitter bipolar transistors*. *Journal of Applied Physics*, **77**(12): 6278–6288, 1995.

M. J. Deen, S. Rumysantesev, R. Bashir and R. Taylor. *Measurements and comparison of low frequency noise in npn and pnp polysilicon emitter bipolar transistors*. *Journal of Applied Physics*, **84**(1): 625–633, 1998.

M. J. Deen, O. Marinov and M. Sanden. *A new model for the low-frequency noise and the noise level variation in polysilicon emitter BJTs*. *IEEE Transactions on Electron Devices*, **49**(3): 514–520, 2002.

C. A. Dimitriadis, J. Brini and G. Kamarinos. *Low frequency noise in intrinsic low pressure chemical vapour deposited polysilicon resistors*. *The European Physical Journal - Applied Physics*, **3**: 283–285, 1998.

P. Dutta and P. M. Horn. *Low-frequency fluctuations in solids - $1/f$ noise*. *Reviews of Modern Physics*, **53**(3): 497–516, 1981.

N. V. D'yakonova, M. E. Levinshtein and S. L. Rumyantsev. *Temperature-dependence of the low-frequency noise in structurally perfect GaAs and after destructive compression*. *Soviet Physics Semiconductors*, **25**(2): 217–218, 1991.

L. Escotte, J. G. Tartarin, R. Plana and J. Graffeuil. *High-frequency noise in heterojunction bipolar transistors*. *Solid-State Electronics*, **42**(4): 661–663, 1998.

G. Freeman, D. Ahlgren, D. Greenberg, R. Groves, F. Huang, G. Hugo, B. Jagannathan, S. Jeng, J. Johnson, K. Schonenberg, K. Stein, R. Volant and S. Subbanna. *A 0.18 μm 90 GHz f_T SiGe HBT BiCMOS, ASIC-compatible, copper interconnect technology for RF and microwave applications*. In *IEEE International Electron Devices Meeting Technical Digest (IEDM)*, pp. 569–572. Washington, DC, USA, December 5–8, 1999.

G. Freeman, B. Jagannathan, S. J. Jeng, J. S. Rieh, A. D. Stricker, D. C. Ahlgren and S. Subbanna. *Transistor design and application considerations for $>$ 200-GHz SiGe HBTs*. *IEEE Transactions on Electron Devices*, **50**: 645–655, 2003.

M. Fukuda, T. Hirono, T. Kurosaki and F. Kano. *Correlation between $1/f$ noise and semiconductor laser degradation*. *Quality and Reliability Engineering International*, **10**(4): 351–353, 1994.

G. Ghibaudo, O. Roux, C. Nguyen-Duc, F. Balestra and J. Brini. *Improved analysis of low frequency noise in field-effect MOS transistors*. *Physica Status Solidi (a)*, **124**: 571–581, 1991.

H. C. de Graaff and M. T. M. Huybers. *$1/f$ noise in polycrystalline silicon resistors*. *Journal of Applied Physics*, **54**(5): 2504–2507, 1982.

D. R. Greenberg, B. Jagannathan, S. Sweeney, G. Freeman and D. Ahlgren. *Noise performance of a low base resistance 200 GHz SiGe technology*. In *IEEE International Electron Devices Meeting Technical Digest (IEDM)*, pp. 787–790. San Francisco, CA, USA, December 8-11, 2002.

K. Gurley and A. Kareem. *Applications of wavelet transform in earthquake, wind and ocean engineering*. *Engineering Structures*, **21**: 149–167, 1999.

A. Hanssen and L. L. Scharf. *A theory of polyspectra for nonstationary stochastic prosesses*. *IEEE Transactions on Signal Processing*, **51**(5): 1243–1252, 2003.

M. von Hartmann, M. Sanden, M. Östling and G. Bosman. *Random telegraph signal noise in SiGe heterojunction bipolar transistors*. *Journal of Applied Physics*, **92**(8): 4414–4421, 2002.

P.-E. Hellberg, S.-L. Jang and C. S. Peterson. *Work function of boron-doped polycrystalline* $SiGe_{1-x}$ *Films*. *IEEE Electron Device Letters*, **18**(9): 456–458, 1997.

M. J. Hinich. *Testing for Gaussianity and linearity of a stationary time series*. *Journal of Time Series Analysis*, **3**(3): 169–176, 1982.

F. N. Hooge. $1/f$ *noise is no surface effect*. *Physics Letters A*, **29**(3): 139–140, 1969.

F. N. Hooge. $1/f$ *noise*. *Physica B: Condensed Matter*, **83B**: 14–23, 1976.

F. N. Hooge. $1/f$ *noise sources*. *IEEE Transactions on Electron Devices*, **41**(11): 1926–1935, 1994.

F. N. Hooge. *On the additivity of generation-recombination spectra. Part 2:* $1/f$ *noise*. *Physica B: Condensed Matter*, **336**(3-4): 236–251, 2003.

F. N. Hooge and L. K. J. Vandamme. *Lattice scattering causes 1-f noise*. *Physics Letters A*, **66**: 315–316, 1978.

F. N. Hooge, T. G. M. Kleinpenning and L. K. J. Vandamme. *Experimental studies on* $1/f$ *noise*. *Reports on Progress in Physics*, **44**: 479–532, 1981.

HP. *Model 3561A Dynamic Signal Analyzer Operating Manual*. Hewlett-Packard Company, December 1985.

K. K. Hung, P. K. Ko, C. Hu and Y. C. Cheng. *A unified model for the flicker noise in metal-oxide-semiconductor field-effect transistors*. *IEEE Transactions on Electron Devices*, **37**(3): 654–665, 1990.

ISE. *DESSIS Reference Manual*. ISE Integrated Systems Engineering AG, 2003.

C. Jacobson. *CMOS low noise switched charge sensitive preamplifier for CdTe and CdZnTe X-ray detectors*. *IEEE Transactions on Nuclear Science*, **44**(1): 20–25, 1997.

S. L. Jang. *A model of* $1/f$ *noise in polysilicon resistors*. *Solid-State Electronics*, **33**(9): 1155–1162, 1990.

Z. Jin, G. Niu, J. D. Cressler, C. J. Marshall, P. W. Marshall, H. S. Kim, R. Reed and D. L. Harame. $1/f$ *noise in proton irradiated SiGe HBTs*. *IEEE Transactions on Nuclear Science*, **48**(6): 2244–2249, 2001.

Z. Jin, J. D. Cressler, G. Niu and A. J. Joseph. *Low-frequency noise variation in scaled SiGe HBTs*. In *Proceedings of IEEE Bipolar/BiCMOS Circuits and Technology Meeting (BCTM)*, pp. 224–227. Monterey, CA, USA, September 29-October 1, 2002.

Z. Jin, J. D. Cressler, G. F. Niu and A. J. Joseph. *Impact of geometrical scaling on low-frequency noise in SiGe HBTs*. *IEEE Transactions on Electron Devices*, **50**: 676–682, 2003a.

Z. Jin, J. A. Johansen, J. D. Cressler, R. A. Reed, P. W. Marshall and A. J. Joseph. *Using proton irradiation to probe the origin of low-frequency noise variations in SiGe HBTs*. In *Annual Nuclear and Space Radiation Effects Conference (NSREC)*. Monterey, CA, USA, July 21–25, 2003b.

Z. Jin, J. A. Johansen, J. D. Cressler, R. A. Reed, P. W. Marshall and A. J. Joseph. *Using proton irradiation to probe the origin of low-frequency noise variations in SiGe HBTs*. *IEEE Transactions on Nuclear Science*, **50**(6): 1816–1820, 2003c.

J. A. Johansen, H. Figenschau, X. Y. Chen, A. D. van Rheenen and C. Salm. *Low frequency noise in poly-Si- and poly-SiGe-gated MOSFETs*. In *Proceedings of the International Conference on Noise in Physical Systems and $1/f$ Fluctuations (ICNF)*, edited by G. Bosman, pp. 161–164. Gainesville, FL, USA, October 22-25, 2001.

J. A. Johansen, Z. Jin, J. D. Cressler, Y. Cui, G. Niu, Q. Liang, J.-S. Rieh, G. Freeman, D. Ahlgren and A. Joseph. *On the scaling limits of low-frequency noise in SiGe HBTs*. In *International Semiconductor Device Research Symposium Proceedings (ISDRS)*, pp. 12–13. Washington, DC, USA, December 10–12, 2003a.

J. A. Johansen, Z. Jin, J. D. Cressler and A. J. Joseph. *Geometry-dependent low-frequency noise variations in 120 GHz f_T SiGe HBTs*. In *Digest of Papers, Topical Meeting on Silicon Monolitic Integrated Circuits in RF Systems (SiRF)*, edited by G. E. Ponchak, pp. 57–59. Grainau, Germany, April 9–11, 2003b.

J. A. Johansen, Y. Birkelund, Z. Jin and J. D. Cressler. *A statistical tool for probing the coupling between noisy traps in semiconductor devices, with application to $1/f$ noise in SiGe HBTs*. *Accepted for the Topical Meeting on Silicon Monolitic Integrated Circuits in RF Systems (SiRF)*, Atlanta, Georgia, September 8-12, 2004a.

J. A. Johansen, Z. Jin, J. D. Cressler, Y. Cui, G. Niu, Q. Liang, J.-S. Rieh, G. Freeman, D. Ahlgren and A. Joseph. *On the scaling limits of low-frequency noise in SiGe HBTs*. *Accepted for publication in Solid-State Electronics*, 2004b.

E. R. Johnson and S. M. Christian. *Some properties of germanium-silicon alloys*. *Physical Review*, **95**: 560–561, 1954.

A. Joseph, D. Coolbaugh, M. Zierak, R. Wuthrich, P. Geiss, Z. He, X. Liu, B. Orner, J. Johnson, G. Freeman, D. Ahlgren, B. Jagannathan, L. Lanzerotti, V. Ramachandran, J. Malinowski, H. Chen, J. Chu, P. Gray, R. Johnson, J. Dunn, S. Subbanna, K. Schonenberg, D. Harame, R. Groves, K. Watson, D. Jadus, M. Meghelli and A. Rylyakov. *A*

0.18 μm BiCMOS technology featuring 120/100 GHz (f_T/f_{max}) HBT and ASIC-compatible CMOS using copper interconnect. In *Proceedings of IEEE Bipolar/BiCMOS Circuits and Technology Meeting (BCTM)*, pp. 143–146. Minneapolis, MN, USA, September 30–October 2, 2001.

K. Kandiah. *Random telegraph signal currents and low-frequency noise in JFETs*. *IEEE Transactions on Electron Devices*, **41**(11): 2006–2015, 1994.

J. Kilmer, A. van der Ziel and G. Bosman. *Presence of mobility-fluctuation $1/f$ noise identified in silicon p^+np transistors*. *Solid-State Electronics*, **26**(1): 71–74, 1983.

T. J. King, J. R. Pfiester, J. D. Shott, J. P. McVittie and K. C. Saraswat. *A polycrystalline $Si_{1-x}Ge_x$-gate CMOS technology*. In *IEEE International Electron Devices Meeting Technical Digest (IEDM)*, pp. 253–256. New York, NY, USA, 1990.

M. J. Kirton and M. J. Uren. *Noise in solid-state microstructures: A new perspective on individual defects, interface states and low-frequency ($1/f$) noise*. *Advances in Physics*, **38**(4): 367–468, 1989.

T. G. M. Kleinpenning. *$1/f$ noise in p-n diodes*. *Physica B+C*, **98**(4): 289–299, 1980.

W. S. Lau, E. F. Chor, C. S. Foo and W. C. Khoong. *Strong low-frequency noise in polysilicon emitter bipolar transistors with interfacial oxide due to fluctuations in tunneling probabilities*. *Japanese Journal of Applied Physics Part II*, **31**(8A): L1021–1023, 1992.

H. G. Lee, S. Y. Oh and G. Fuller. *A simple and accurate method to measure the threshold voltage of an enhancement-mode MOSFET*. *IEEE Transactions on Electron Devices*, **29**: 346–348, 1982.

W.-C. Lee, B. Watson, T.-J. King and C. Hu. *Enhancement of PMOS device performance with Poly-SiGe gate*. *IEEE Electron Device Letters*, **20**(5): 232–234, 1999.

A. Levitas. *Electrical properties of germanium-silicon alloys*. *Physical Review*, **99**(6): 1810–1814, 1955.

P. Llinares, D. Celi, O. Roux-dit-Buisson, G. Ghibaudo and J. A. Chroboczek. *Dimension scaling of $1/f$ noise in the base current of quasiself-aligned polysilicon emitter bipolar junction transistors*. *Journal of Applied Physics*, **82**(5): 2671–2675, 1997.

M. Y. Luo and G. Bosman. *An analytical model for $1/f$ noise in polycrystalline silicon thin films*. *IEEE Transactions on Electron Devices*, **37**(3): 768–774, 1990.

A. J. Madenach and J. H. Werner. *Noise spectroscopy of silicon grain boundaries*. *Physical Review B*, **38**(18): 13150–13160, 1988.

T. Manku, J. M. McGregor, A. Nathan, D. J. Roulston, J. P. Noel and D. C. Houghton. *Drift hole mobility in strained and unstrained doped $Si_{1-x}Ge_x$ alloys*. *IEEE Transactions on Electron Devices*, **40**(11): 1990–1996, 1993.

H. A. W. Markus and T. G. M. Kleinpenning. *Low-frequency noise in polysilicon emitter bipolar transistors*. *IEEE Transactions on Electron Devices*, **42**(4): 720–727, 1995.

P. W. Marshall, C. J. Dale, M. A. Carts and K. A. LaBel. *Particle induced bit errors in high performance fiber optic data links for satellite data management*. *IEEE Transactions on Nuclear Science*, **41**: 1958–1965, 1994.

A. L. McWhorter. *$1/f$ noise and related surface effects in germanium*. *Lincoln Laboratory Report*, **80**, May 1955a.

A. L. McWhorter. *Surface traps and 1-f noise in germanium*. *Physical Review*, **98**: 1191–1192, 1955b.

V. Mitin, L. Reggiani and L. Varani. *Generation-recombination noise in semiconductors*. In *Noise and Fluctuations Control in Electronic Devices*, edited by A. Balandin, chapter 2, pp. 11–29. American Scientific Publishers, 2003.

A. Mounib, F. Balestra, N. Mathieu, J. Brini, G. Ghibaudo, A. Chovet, A. Chantre and A. Nouailhat. *Low-frequency noise sources in polysilicon emitter BJTs: influence of hot-electron-induced degradation and poststress recovery*. *IEEE Transactions on Electron Devices*, **42**(9): 1647–1652, 1995.

A. Mounib, G. Ghibaudo, G. Balestra, D. Pogany, A. Chantre and J. A. Chroboczek. *Low frequency ($1/f$) noise model for the base current in polysilicon emitter bipolar junction transistors*. *Journal of Applied Physics*, **79**(6): 3303–3306, 1996.

K. M. Murray, W. J. Stapor and C. Castenada. *Proton beam facility for single event research*. *Nuclear Instruments and Methods in Physics Research Section B: Beam Interactions with Materials and Atoms*, **B56/57**: 616, 1991.

M. Ohtsu and S. Kotajima. *Derivation of the spectral width of a 0.8μm AlGaAs laser considering $1/f$ noise*. *Japanese Journal of Applied Physics Part I*, **23**(6): 760–764, 1984.

D. B. Percival and A. T. Walden. *Spectral Analysis for Physical Applications: Multitaper and Conventional Univariate Techniques*. Cambridge University Press, Cambridge, U.K., 1993.

D. B. Percival and A. T. Walden. *Wavelet Methods for Time Series Analysis*. Cambridge University Press, Cambridge, U.K., 2000.

R. Plana, L. Escotte, J. P. Roux, J. Graffeuil, A. Gruhle and H. Kibbel. *$1/f$ noise in self-aligned Si/SiGe heterojunction bipolar transistor*. *IEEE Electron Device Letters*, **16**: 58–60, 1995.

Y. V. Ponomarev, P. A. Stolk, C. Salm, J. Schmitz and P. H. Woerlee. *High-performance deep submicron CMOS technologies with polycrystalline-SiGe gates*. *IEEE Transactions on Electron Devices*, **47**(4): 848–855, 2000.

T. S. Rao and M. M. Gabr. *A test for linearity of stationary time series*. *Journal of Time Series Analysis*, **1**(1): 145–158, 1980.

S. N. Rashkeev, D. M. Fleetwood, R. D. Schrimpf and S. T. Pantelides. *Proton-induced defect generation at the Si-SiO_2 interface*. *IEEE Transactions on Nuclear Science*, **48**: 2086–2092, 2001.

M. Regis, M. Borgarino, L. Bary, O. Llopis, J. Graffeuil, L. Escotte, U. Koenig and R. Plana. *Noise behavior in SiGe devices*. *Solid-State Electronics*, **45**(11): 1891–1897, 2001.

A. D. van Rheenen, G. Bosman and C. M. van Vliet. *Decomposition of generation-recombination noise spectra in separate Lorentzians*. *Solid-State Electronics*, **28**(5): 457–463, 1985.

J.-S. Rieh, B. Jagannathan, H. Chen, K. T. Schonenberg, D. Angell, A. Chinthakindi, J. Florkey, F. Golan, D. Greenberg, S.-J. Jeng, M. Khater, F. Pagette, C. Schnabel, P. Smith, A. Stricker, K. Vaed, R. Volant, D. Ahlgren, G. Freeman, K. Stein and S. Subbanna. *SiGe HBTs with cut-off frequency of 350 GHz*. In *IEEE International Electron Devices Meeting Technical Digest (IEDM)*, pp. 771–774. San Francisco, CA, USA, December 8-11, 2002.

C. Salm. *Polycrystalline Germanium-Silicon for Advanced CMOS Technologies*. Ph.D. thesis, Universiteit Twente, Enschede, The Netherlands, September 1997.

C. Salm, J. H. Klootwijk, Y. Ponomarev, P. W. M. Boos, D. J. Gravesteijn and P. H. Woerlee. *Gate current and oxide reliability in p^+ poly MOS capacitors with poly-Si and poly-$Ge_{0.3}Si_{0.7}$ gate material*. *IEEE Electron Device Letters*, **19**(7): 213–215, 1998.

M. Sanden and M. J. Deen. *Low-frequency noise in advanced Si-based bipolar transistors and circuits*. In *Noise and Fluctuations Control in Electronic Devices*, edited by A. Balandin, chapter 11, pp. 235–247. American Scientific Publishers, 2002.

M. Sanden, O. Marinov, M. J. Deen and M. M. Östling. *A new model for the low-frequency noise and the noise level variation in polysilicon emitter BJTs*. *IEEE Transactions on Electron Devices*, **49**: 514–520, 2002.

W. Schottky. *Über spontane Stromschwankungen in verschiedenen Elektrizitätsleitern*. *Annalen der Physik*, **57**: 541–567, 1918.

D. K. Schroder. *Semiconductor Material and Device Characterization*. Wiley-Interscience. John Wiley & Sons, second edition, 1998.

W. Shockley. *The theory for p-n junctions in semiconductors and p-n junction transistors*. *Bell Systems Technical Journal*, **28**: 435, 1949.

E. Simoen and C. Claeys. *Low-frequency noise performance of scaled deep submicron metal-oxide-semiconductor devices*. In *Noise and Fluctuations Control in Electronic Devices*, edited by A. Balandin, chapter 8, pp. 163–186. American Scientific Publishers, 2002.

H. Stöhr and W. Klemm. *Über Zweistoffsyteme mit Germanium, Germanium/Aluminium, Germanium/Zinn und Germanium/Silicium*. *Zeitschrift für anorganische und allgemine Chemie*, **241**: 305–323, 1939.

M. Surdin. *Journal de Physique et le Radium*, **10**: 188, 1939.

S. M. Sze. *Physics of Semiconductor Devices*. Wiley-Interscience. John Wiley & Sons, second edition, 1981.

J. Theiler, S. Eubank, A. Longtin, B. Galdrikian and J. D. Farmer. *Testing for nonlinearity in times series: the method of surrogate data*. *Physica D*, **58**: 77–94, 1992.

D. J. Thomson. *Spectrum estimation and harmonic analysis*. *Proceedings of the IEEE*, **70**(9): 1055–1096, 1982.

M. J. Uren, D. J. Day and M. J. Kirton. *$1/f$ noise and random telegraph noise in silicon MOSFETs*. *Applied Physics Letters*, **47**(11): 1195–1197, 1985.

E. P. Vandamme and L. K. J. Vandamme. *Critical discussion on unified $1/f$ noise models for MOSFETs*. *IEEE Transactions on Electron Devices*, **47**(11): 2146–2152, 2000.

L. K. J. Vandamme and R. G. M. Penning de Vries. *Correlation between MOST $1/f$ noise and CCD transfer inefficiency*. *Solid-State Electronics*, **28**(10): 1049–1056, 1985.

L. K. J. Vandamme, R. Alabedra and M. Zommiti. *$1/f$ noise as a reliability estimation for solar cells*. *Solid-State Electronics*, **26**(7): 671–674, 1983.

L. K. J. Vandamme, X. Li and D. Rigaud. *$1/f$ noise in MOS devices, mobility or number fluctuations?*. *IEEE Transactions on Electron Devices*, **41**(11): 1936–1945, 1994.

L. K. J. Vandamme, E. P. Vandamme and J. J. Dobbelsteen. *Impact of silicon substrate, iron contamination and perimeter on saturation current and noise in n^+p diodes*. *Solid-State Electronics*, **41**(6): 901–908, 1997.

L. S. Vempati, J. D. Cressler, J. A. Babcock, R. C. Jaeger and D. L. Harame. *Low-frequency noise in UHV/CVD epitaxial Si and SiGe bipolar transistors*. *IEEE Journal of Solid-State Circuits*, **31**: 1458–1467, 1996.

M. B. Weissman. *Low-frequency noise as a tool to study disordered materials*. *Annual Review of Materials Science*, **26**: 395–429, 1996.

X. L. Wu, A. van der Ziel, A. N. Birbas and A. D. van Rheenen. *Burst-type noise mechanism in bipolar transistors*. *Solid-State Electronics*, **32**(11): 1039–1042, 1989.

A. van der Ziel. *Proof of basic semiconductor flicker noise formulae*. *Solid-State Electronics*, **17**: 110–111, 1974.